Search for New Resonances and Dark Matter Particles with BSM Higgs Boson Productions at the LHC

by

Wen Guo

A dissertation submitted in partial fulfillment
of the requirements for the degree of
Doctor of Philosophy
(Physics)
in The University of Michigan
2018

Doctoral Committee:

Professor Bing Zhou, Chair
Associate Professor Christine Aidala
Professor Aaron T. Pierce
Assistant Professor Thomas A. Schwarz
Assistant Professor Qiong Yang

Wen Guo

wenguo@umich.edu

ORCID iD: 0000-0001-7285-7490

To my parents who brought me into the scientific field,
and to my fiancee Melody, who inspired me during the hard time.

ACKNOWLEDGEMENTS

This dissertation cannot be achieved only by myself, numerous great people made indispensable contribution to make it happen. I owe my great gratitude to all of you, who not only assisted me moving forward, but also shaped the four years time into an unforgettable one in my life.

First of all, I would like to express my sinserest gratitude to my advisor Dr. Bing Zhou. Bing provided me with tremendous help during my Ph.D. study. Her knowledge, expertise, motivation and patience always supported me when I got stuck with obstacles in research. Not only limited to academic instructions, her support goes into every aspect, from shaping my critical thinking patterns to designing my future career path. Her thoughful ideas, broad vision and hard working ethics guide me, impact me and incent me all the time. It is my great fortune to meet Bing and have her as my advisor and mentor.

Beisdes my advisor, I would also like to express my sincere gratitude to other members of my committee: Dr. Christine Aidala, Dr. Aaron Pierce, Dr. Thomas Schwarz, and Dr. Qiong Yang for reviewing my dissertation, giving insightful comments and asking intuitive questions.

I'm very grateful for the opportunities to take the physics courses provided by Dr. Ratindranath Akhoury, Dr. Finn Larsen Dr. Aaron Pierce, Dr. Jianming Qian, Dr. Robert Savit, Dr. James Wells, Dr. Bing Zhou, Dr. Paul Zimmerman, which helped me consolidate the fundations for research work.

I also owe my gratitude to Dr. Dante Amidei, Dr. Homer Neal, Dr. Jianming Qian, Dr. Tom Schwarz, and Dr. Junjie Zhu for their insightful discussions on physics analyses and encouragements to me. It was my great pleasure to work with Dr. Tiesheng Dai, Dr. Philipp Fleischmann, who provided me technique support in maintaining MDT online configuration database. Here, special thanks to Tiesheng Dai for his role as a teacher and a mentor. I want to express my sincere gratitude to Dr. Shawn McKee, Bob Ball and Benjeman Meekhof for their expertise in maintaining our computing system and instant response to whatever problem the system pops up;

I also want to express my sincere gratitude to graduate coordinators, Christina

Zigulis and Nitesh Singh for handling all the physics graduate program issues as well as US-Europe transitions.

My sincere gratitude also goes to my colleagues in the $HZZllvv$ analysis group, to Dr. Giacomo Artoni, Dr. Sarah Heim, Dr. Eleni Mountricha, Dr. Hideki Okawa, Dr. Arthur Schaffer, Dr. Monica Trovatelli, Dr. Lailin Xu, and Dr. Yusheng Wu, for their dedication in organizing meetings and providing strong support for analyses; to Artem Basalaev Dr. Alison Elliot, Dr. Xiangyang Ju, Dr. Kota Kasahara, Kayla McLean, Dr. Johen Meyer, Mariyan Petrov, and Gabriele Sabato for their efficient collaboration and strong contributions to analyses; and special thanks to Dr. Cong Geng and Dr. Yusheng Wu, who worked with me closely and gave me various analyses suggestions. They guided me from the very beginning such as setting up framework to the very end when the paper being published. I'll never forget those long but intuitive discussions with them.

I also want to thank my friends from USTC, the Unievrsity of Michigan(UM) and CERN, to Jue Chen, Jing Chen, Dr. Hok-Chuen Cheng, Yicheng Guo, Rachel Hyneman, Dr. Bing Li, Hao Liu, Jing Li, Dr. Lulu Liu, Yanlin Liu, Dr. Haonan Lu, Dr. Nan Lu, Jingyu Luo, Ismet Siral, Rongkun Wang, Aaron White, Josh Xi, Dr. Dongliang Zhang, Liqing Zhang and Zhi Zheng for their being very friendly and bringing me joyful time at CERN.

Finally, I would like to thank all the staff from UM Physics Department for their various excellent supports and to thank the Department of Energy, the National Science Foundation and the University of Michigan, the research work could not be conducted without the financial aids from them. I express my gratitude to those institutions and agencies.

TABLE OF CONTENTS

DEDICATION ii

ACKNOWLEDGEMENTS iii

LIST OF FIGURES viii

LIST OF TABLES xv

ABSTRACT xxi

CHAPTER

I. Introduction 1

II. Theory 5

2.1 The Standard Model of Particle Physics 5
2.1.1 The SM Particles 5
2.1.2 The electroweak theory 6
2.1.3 The Higgs Mechanism 10
2.1.4 Natural Units 12
2.2 Beyond the Standard Model 12
2.2.1 Higgs portal in Search for dark matter particles . . 12
2.2.2 BSM Higgs Benchmark Models 13
2.2.3 Randall-Sundrum Graviton 16
2.3 Physics Phenomenology at the LHC 18
2.3.1 Hadronic Collisions 18
2.3.2 Monte Carlo event generator 20

III. The Large Hadron Collider and the ATLAS Experiment . . . 22

3.1 The Large Hadron Collider 22
3.1.1 The LHC Complex 22
3.1.2 LHC Design Parameters 24

3.2 The ATLAS Experiment . . . 29
3.2.1 Inner Detector . . . 30
3.2.2 Calorimeter . . . 32
3.2.3 Muon Spectrometer . . . 34
3.2.4 Trigger . . . 36
3.2.5 Detector Simulation . . . 38

IV. Object Reconstruction . . . 40

4.1 Track . . . 40
4.2 Primary Vertex . . . 42
4.3 Electron . . . 43
4.3.1 Electron Reconstruction . . . 43
4.3.2 Electron Identification . . . 45
4.3.3 Electron Isolation . . . 46
4.4 Muon . . . 47
4.4.1 Muon Reconstruction . . . 47
4.4.2 Muon Identification . . . 48
4.4.3 Muon Isolation . . . 51
4.5 Jet . . . 51
4.5.1 Jet reconstruction and calibration . . . 51
4.5.2 B-jet tagging . . . 53
4.6 Missing Transverse Momentum . . . 53
4.6.1 $E_{\mathrm{T}}^{\mathrm{miss}}$ reconstruction and calibration . . . 53

V. Search For Dark Matter Particles . . . 56

5.1 Introduction . . . 56
5.2 Data and MC Samples . . . 57
5.2.1 Data Sample . . . 57
5.2.2 Monte Carlo Samples . . . 57
5.3 Event Selection . . . 64
5.3.1 Object Selection . . . 64
5.3.2 Event Selection . . . 67
5.4 Background Estimation and Systematic Uncertainty . . . 78
5.4.1 ZZ Background . . . 79
5.4.2 WZ Background . . . 80
5.4.3 Top, WW, Wt and $Z \to \tau\tau$ Background . . . 87
5.4.4 Z+jets background . . . 89
5.4.5 W+jets background . . . 94
5.4.6 Other Backgrounds . . . 98
5.4.7 Systematic Uncertainty . . . 98
5.5 Results . . . 100
5.5.1 Data Comparison with Predicted Background and Signal . . . 100

5.5.2 Likelihood definition . . . 101
5.5.3 Limits . . . 104
5.5.4 Short Summary . . . 107
5.5.5 Discussion on DM Searches . . . 107

VI. Search For New Resonances in High Mass Scale . . . 111

6.1 Introduction . . . 111
6.2 Data and MC Samples . . . 112
6.2.1 Data Sample . . . 112
6.2.2 Monte Carlo Samples . . . 112
6.3 Event Selection . . . 114
6.3.1 Final Event Selection . . . 114
6.3.2 Kinematic Distributions . . . 114
6.3.3 Signal Acceptance and Systematic Uncertainties . . . 115
6.4 Background Estimation and Systematic Uncertainty . . . 120
6.4.1 ZZ Background . . . 122
6.4.2 WZ Background . . . 123
6.4.3 Top, WW, Wt and $Z \to \tau\tau$ Background . . . 123
6.4.4 Z+jets background . . . 124
6.4.5 W+jets background . . . 126
6.4.6 Other Background . . . 127
6.5 Results . . . 127
6.5.1 Data Comparison with Predicted Background and Signal . . . 127
6.5.2 Limits . . . 127
6.5.3 Short Summary . . . 132

VII. Summary . . . 135

BIBLIOGRAPHY . . . 137

LIST OF FIGURES

Figure

2.1 Elementary particles in the Standard Model of particle physics [20]. 7
2.2 The Higgs potential ($V(\phi)$) for $\mu^2 > 0$ (dash line) and $\mu^2 < 0$ (solid line) [21]. . . . 10
2.3 Feynman diagrams for the decay of the Higgs boson into dark matter particles (a) and the Higgs boson produced in association with a Z boson (b). . . . 13
2.4 Schematic representation of the RS warped model of hierarchy and flavor [33]. . . . 17
2.5 Schematic view of a hadron-hadron collision [37]. . . . 18
2.6 NNPDF3.0 NNLO PDF set for $Q^2 = 10$ GeV^2 and $Q^2 = 10^4$ GeV^2 [38]. . . . 19
2.7 The basic structure of a showering and hadronization generator event is shown schematically [39]. . . . 21
3.1 Distribution of the LHC complex [47]. . . . 23
3.2 The cumulative luminosity versus time delivered by the LHC (green) and recorded by the ATLAS (yellow) during stable proton-proton beam periods at the center-of-mass energy of $\sqrt{s} = 13$ TeV in 2015 (left) and 2016 (right) [51]. . . . 27
3.3 Luminosity-weighted distribution of the mean number of interactions per crossing in the 2015 and 2016 pp collision data [51]. . . . 28
3.4 The longitudinal cut-away view of the ATLAS detector [52]. . . . 29
3.5 The cut-away view of the ATLAS Inner Detector [52]. . . . 31
3.6 The cut-away view of the ATLAS Calorimeter [52]. . . . 33
3.7 The cut-away view of the ATLAS Muon Spectrometer [52]. . . . 35
3.8 Block diagram of the ATLAS trigger and data acquisition systems. [63] 37
3.9 The flow of the ATLAS simulation software, from event generators (top left) through reconstruction (top right). [64] . . . 39
4.1 A wedge of the transverse plane of the ATLAS detector. Hadrons, leptons and photons have different signatures left in the detector. With algorithms dealing with such different characteristics, physics objects are reconstructed for following analysis [65]. . . . 41
4.2 The electron identification efficiency for *loose*, *medium*, and *tight* categories as a function of transverse energy E_T [67]. . . . 45

4.3 Muon reconstruction efficiency as a function of η measured in $Z \rightarrow \mu\mu$ events for muons with $p_T > 10$ GeV shown for *Medium* (left), *Tight* (right) muon selections. In addition, the left plot also shows the efficiency of the *Loose* selection in the region $|\eta|$ <0.1 where the *Loose* and *Medium* selections differ significantly. The error bars on the efficiencies indicate the statistical uncertainty. Panels at the bottom show the ratio of the measured to predicted efficiencies, with statistical and systematic uncertainties [68]. 50
4.4 The scheme of $E_{\mathrm{T}}^{\mathrm{miss}}$ generation according to detectable particles. . . 54
4.5 Comparison of the performance of $E_{\mathrm{T}}^{\mathrm{miss}}$ built from TST and CST, and the Track $E_{\mathrm{T}}^{\mathrm{miss}}$, under different pile-up conditions. The resolution (RMS of $E_{\mathrm{x}}^{\mathrm{miss}}$, $E_{\mathrm{y}}^{\mathrm{miss}}$) is shown shown as a function of N_{PV}. [75] 55
5.1 Feynman diagrams for leading order ZH production through (a) qq annihilation and (b) gg fusion. In this analysis, we search for an invisible Higgs (h) decay by assuaming this Higgs boson (h) is produced with the SM Higgs Boson (H) cross section. 56
5.2 The invariant mass of leptons that pass the object selections in the (a) electron channel and (b) muon channel. Only events with two same flavor and opposite sign leptons and no additional leptons are accepted, whose invariant mass is 76 < M_{ll} <106 GeV. MC samples are normalized to their cross section values as given in Section 5.2.2 and re-scaled to the data integrated luminosity reported in figure. The error band in the ratio plot shows the systematic uncertainty on the MC. 71
5.3 Kinematic distributions that are used for event selections in the $\ell\ell$+ $E_{\mathrm{T}}^{\mathrm{miss}}$ analyses for the signal, backgrounds and data in the electron channel after applying Z mass window cut : (a) $E_{\mathrm{T}}^{\mathrm{miss}}$, (b) the distance between leptons, ΔR_{ll}, (c) the fractional p_{T} difference, (d) the opening angle between $E_{\mathrm{T}}^{\mathrm{miss}}$ and di-lepton pair, (e) number of central jets that have $p_{\mathrm{T}} > 20$ GeV and $|\eta| < 2.5$, and (f) number of b-tagged jets. The bottom plot shows the ratio between data and all the background MC expectation. MC samples are normalized to their cross section values as given in Section 5.2.2 and re-scaled to the data integrated luminosity reported in figure. The error band in the ratio plot shows the systematic uncertainty on the MC expectation. 72

5.4 Kinematic distributions that are used for event selections in the $\ell\ell+ E_{\mathrm{T}}^{\mathrm{miss}}$ analyses for the signal, backgrounds and data in the muon channel after applying Z mass window cut : (a) $E_{\mathrm{T}}^{\mathrm{miss}}$, (b) the distance between leptons, ΔR_{ll}, (c) the fractional p_{T} difference, (d) the opening angle between $E_{\mathrm{T}}^{\mathrm{miss}}$ and di-lepton pair, (e) number of central jets that have $p_{\mathrm{T}} > 20$ GeV and $|\eta| < 2.5$, and (f) number of b-tagged jetse. The bottom plot shows the ratio between data and all the background MC expectation. MC samples are normalized to their cross section values as given in Section 5.2.2 and re-scaled to the data integrated luminosity reported in figure. The error band in the ratio plot shows the systematic uncertainty on the MC expectation. 73

5.5 $E_{\mathrm{T}}^{\mathrm{miss}}$ distributions for the $Zh \rightarrow \ell\ell +$ invisible process with EW correction systematic uncertainty applied in the (a) ee and (b) $\mu\mu$ channels. 75

5.6 The derived NNLO QCD k-factors in binned m(4l) for the $q\bar{q} \rightarrow ZZ$ process. Also shown for comparison with the k-factors used in the previous study note which are calculated from the charged four-lepton channel [100]. The error bar in the plot represents the statistical uncertainty on the k-factor. 80

5.7 The p_{T} (top two), η (middle two) and ϕ (bottom two) distributions of the additional muon in events with two electrons (left three) or two muons (right three) with an invariant mass consistent with Z boson mass. MC samples are normalized to their cross section values as given in Section 6.2.2.2 and re-scaled to the data integrated luminosity reported in the figure. The scale factor of $1.29 \pm 0.03 \pm 0.07$ is applied to the WZ MC, and NNLO and NLO corrections are applied for ZZ. The error band in the ratio plot includes only the statistical uncertainty on MC. 82

5.8 The p_{T} (top two), η (middle two) and ϕ (bottom two) distributions of the additional electron in events with two electrons (left three) or two muons (right three) with an invariant mass consistent with Z boson mass. MC samples are normalized to their cross section values as given in Section 6.2.2.2 and re-scaled to the data integrated luminosity reported in the figure. The scale factor of $1.29 \pm 0.03 \pm 0.07$ is applied to the WZ MC, and NNLO and NLO corrections are applied for ZZ. The error band in the ratio plot only includes the statistical uncertainty on MC. 83

5.9 Transverse mass of the W boson for both data and Monte Carlo in (a) the ee + e channel, (b) ee + μ channel, (c) $\mu\mu$ + e channel and (d) $\mu\mu$ + μ channel in events with one additional electron or muon with respect to the lepton pair whose invariant mass is consistent with the Z boson mass. MC samples are normalized to their cross section values as given in Section 6.2.2.2 and re-scaled to the data integrated luminosity reported in the figure. The scale factor of $1.29 \pm 0.03 \pm 0.07$ is applied to the WZ MC, and NNLO and NLO corrections are applied for ZZ. The bottom plots show the ratio of the data and Monte Carlo. The red arrow in the ratio plot indicates the ratio is up/down beyond y-axis range. 84

5.10 $E_{\mathrm{T}}^{\mathrm{miss}}$ distributions after M_T cut for data and Monte Carlo in (a) the ee + e channel, (b) ee + μ channel, (c) $\mu\mu$ + e channel and (d) $\mu\mu$ + μ channel in events with one additional electron or muon with respect to the lepton pair whose invariant mass is consistent with the Z boson mass. MC samples are normalized to their cross section values as given in Section 6.2.2.2 and re-scaled to the data integrated luminosity reported in the figure. For WZ background, the scale factor of $1.29 \pm 0.03 \pm 0.07$ from data-driven estimate is applied, NNLO and NLO corrections are applied for ZZ. The bottom plots show the ratio of the data and Monte Carlo. The red arrow in the ratio plot indicates that the ratio is up/down beyond y-axis range. . 85

5.11 Scheme of the boolean "ABCD" method. Signal region A is defined by both variables equal true, representing all selections passed. . . . 91

5.12 Scheme of the one side-band method. A selection is reversed to construct the side-band region. 93

5.13 (a) Fake factor as measured in data, W+jets, and Z+jets MC samples with regarding to lepton p_{T}(a), η (b) in ee channel 97

5.14 (a) Fake factor as measured in data, W+jets and Z+jets MC samples with regarding to lepton p_{T}(a), η (b) in $\mu\mu$ channel. 97

5.15 Theoretical systematic uncertainties on ZZ background due to QCD scale and PDF variation, as a function of the transverse mass of the ZZ resonance. 100

5.16 QCD and PDF scale included shape uncertainties as a function of the mass of the WZ resonance. 100

5.17 The $E_{\mathrm{T}}^{\mathrm{miss}}$ distribution after final selections in the (a) ee channel, (b) $\mu\mu$ channel, and (c) $ee + \mu\mu$ combined channel. The yields of WZ, $Top/WW/Z \to \tau\tau$ (Non-resonant-ll) and $Z \to ee/Z \to \mu\mu$ backgrounds are estimated using data-driven method and the $E_{\mathrm{T}}^{\mathrm{miss}}$ shapes for these backgrounds are derived from MC samples. The ZZ backgrounds are fully estimated from theoretical predictions and higher order corrections are applied. Both statistical and systematic uncertainties are included in the uncertainties bands, and they are summed quadratically. 102

5.18 The CL scan as function of BR($h \to$ inv.) for $Zh \to \ell\ell +$ invisible with $m_{\mathrm{h}} = 125\,\mathrm{GeV}$. Plots (a) and (b) are the ee and $\mu\mu$ channel results, and plot (c) is the $ee + \mu\mu$ combined channel results. The observed and expected curves are shown with solid and dashed lines. Signal is scaled to the SM cross section value times the best-fit μ value 0.3. The $\pm1\sigma$ and $\pm2\sigma$ bands are shown as yellow and green bands respectively. The crossing point between 95% CL line solid (dashed) line gives the observed (expected) upper limit on BR($h \to$ inv.). . . 105
5.19 The 95% CL upper limits on $\sigma(pp \to Zh \to \ell\ell + inv.)$ as a function of m_H, as obtained from the combined ee+$\mu\mu$ channels. Observed and expected limits are given, as well as $\pm1\sigma$ and $\pm2\sigma$ error bands on the expected limit. No significant excess is seen in all channels, and the observed and expected limits are compatible within the error bands. Full statistical and systematic uncertainties are included in the fit. . 108
5.20 Spin-independent WIMP-nucleon cross section limits vs WIMP mass as of summer 2013 [115]. 109
5.21 Bounds on the spin-independent direct detection cross section $\sigma^{\mathrm{SI}}_{\chi p}$ in Higgs portal models derived for $m_h = 125$ GeV and the invisible branching fraction of 20% (colord lines). For comparison, the current and future direct bounds from the XENON experiments are plotted (black lines) [116]. 110
6.1 Feynman diagram for new heavy resonance produced in gluon-gluon fusion and decay to dilepton + $E_{\mathrm{T}}^{\mathrm{miss}}$ final state. X represents an additional heavy Higgs boson (H) or a bulk RS graviton (G^*). . . . 111
6.2 The $E_{\mathrm{T}}^{\mathrm{miss}}$ distribution of the expected backgrounds after applying all analysis cuts up through the di-lepton invariant mass window. The plot on the left shows the result for the di-electron channel whereas the right plot shows the result for the di-muon channel. The structure in the data/MC ratio is due to mismodeling of the $E_{\mathrm{T}}^{\mathrm{miss}}$, and is covered by the relevant jet and $E_{\mathrm{T}}^{\mathrm{miss}}$ systematics. The red arrows in the ratio plot indicate that the point is off the scale. The uncertainty band in the ratio includes systematic uncertainties, while the statistical uncertainty is propagated to the data/MC points. 115
6.3 The ΔR distribution of the expected backgrounds after applying all analysis cuts up through the E_T^{miss} cut. The plot on the left shows the result for the di-electron channel whereas the right plot shows the result for the di-muon channel. The red arrows in the ratio plot indicate that the point is off the scale. The uncertainty band in the ratio includes systematic uncertainties, while the statistical uncertainty is propagated to the data/MC points. 116

6.4 The $\Delta\phi(Z, E_{\mathrm{T}}^{\mathrm{miss}})$ distribution of the expected backgrounds after applying all analysis cuts up through the ΔR cut. The plot on the left shows the result for the di-electron channel whereas the right plot shows the result for the di-muon channel. The red arrows in the ratio plot indicate that the point is off the scale. The uncertainty band in the ratio includes systematic uncertainties, while the statistical uncertainty is propagated to the data/MC points. 116
6.5 The fractional p_{T} difference distribution of the expected backgrounds after applying all analysis cuts up through the $\Delta\phi(Z, E_{\mathrm{T}}^{\mathrm{miss}})$ cut. The plot on the left shows the result for the di-electron channel whereas the right plot shows the result for the di-muon channel. The red arrows in the ratio plot indicate that the point is off the scale. The uncertainty band in the ratio includes systematic uncertainties, while the statistical uncertainty is propagated to the data/MC points. . . 117
6.6 The $min(\Delta\phi(j, E_{\mathrm{T}}^{\mathrm{miss}}))$ distribution of the expected backgrounds after applying all analysis cuts up through the fractional p_{T}difference cut. The plot on the left shows the result for the di-electron channel whereas the right plot shows the result for the di-muon channel. The red arrows in the ratio plot indicate that the point is off the scale. The uncertainty band in the ratio includes systematic uncertainties, while the statistical uncertainty is propagated to the data/MC points. 117
6.7 The $E_{\mathrm{T}}^{\mathrm{miss}}/H_T$ distribution of the expected backgrounds after applying all analysis cuts up through the $min(\Delta\phi(j, E_{\mathrm{T}}^{\mathrm{miss}}))$ cut. The plot on the left shows the result for the di-electron channel whereas the right plot shows the result for the di-muon channel. The red arrows in the ratio plot indicate that the point is off the scale. The uncertainty band in the ratio includes systematic uncertainties, while the statistical uncertainty is propagated to the data/MC points. 118
6.8 The n_{b-jets} distribution of the expected backgrounds after applying all analysis cuts up through the $E_{\mathrm{T}}^{\mathrm{miss}}/H_T$ cut. The plot on the left shows the result for the di-electron channel whereas the right plot shows the result for the di-muon channel. The red arrows in the ratio plot indicate that the point is off the scale. The uncertainty band in the ratio includes systematic uncertainties, while the statistical uncertainty is propagated to the data/MC points. 118
6.9 The signal acceptance versus resonance mass for heavy Higgs and Graviton. Only the statistical uncertainty is shown. 119

6.10 The m_T^{ZZ} distribution after final selections in the (a) ee channel, (b) $\mu\mu$ channel, and (c) $ee + \mu\mu$ combined channel. The yield of WZ, $Top/WW/Z \to \tau\tau$ and $Z \to ee/Z \to \mu\mu$ backgrounds are estimated using data-driven method and the m_T^{ZZ} shapes for these backgrounds are derived from MC samples. Signals are scaled to the SM cross section values time branching fraction of $H \to ZZ^*$ and $ZZ \to \ell\ell\nu\nu$. The ZZ backgrounds are fully estimated from theoretical predictions and higher order corrections are applied. Both statistical and systematic uncertainties are included in the uncertainties bands, and they are summed quadratically. 129

6.11 95% C.L. limits on $\sigma \times \mathrm{BR}(H \to ZZ^*)$ for a narrow width heavy Higgs boson produced a function of its pole mass. The limits are derived using events in ee (top left), $\mu\mu$ (top right) and combined channels (bottom). The observed and expected limits are derived with considering the full uncertainties discussed in previous sections. The limits are derived for mass points between 300 GeV and 1 TeV with a 100 GeV interval. Two additional mass points are added, 1.2 TeV and 1.4 TeV. And limit lines between each mass points are interpolated using an exponential function. Both the statistical and systematic uncertainties are considered in the limit setting. 130

6.12 95% C.L. limits on $\sigma \times \mathrm{BR}(G^* \to ZZ)$ for a Randall-Sundrum Graviton as a function of its pole mass. The limits are derived using events in ee (top left), $\mu\mu$ (top right) and combined channels (bottom). The observed and expected limits are derived with considering the full uncertainties discussed in previous sections. The limits are derived for mass points between 600 GeV and 2 TeV. Limit lines between each mass points are interpolated using an exponential function. . 133

LIST OF TABLES

Table

3.1 The LHC parameters. 26
3.2 The LHC operational conditions in Run I (2010-2012) and in Run II (2015-2016). 28
5.1 Cross section for the $Zh \to \ell\ell$ + invisible signal with $m_h = 125$ GeV, where $\ell = e, \mu, \tau$. 58
5.2 Cross sections at the NLO in perturbation theory, k-factors and filter efficiencies for ZZ POWHEG+Pythia8 samples at $\sqrt{s} = 13$ TeV. Processes listed refer to both quark-quark and gluon-gluon production modes. 59
5.3 Cross sections at the NLO in perturbation theory, k-factors and filter efficiencies for WZ and WW POWHEG+Pythia8 samples at $\sqrt{s} =$ 13 TeV. 60
5.4 Cross sections at the NNLO in perturbation theory, k-factors and filter efficiencies for Z+jets SHERPA $Z \to ee$ samples at $\sqrt{s} = 13$ TeV. 60
5.5 Cross sections at the NNLO in perturbation theory, k-factors and filter efficiencies for Z+jets SHERPA $Z \to \mu\mu$ samples at $\sqrt{s} = 13$ TeV. 61
5.6 Cross sections at the NNLO in perturbation theory, k-factors and filter efficiencies for Z+jets SHERPA $Z \to \tau\tau$ samples at $\sqrt{s} = 13$ TeV. 61
5.7 Cross sections at the NLO in perturbation theory, k-factors and filter efficiencies for triboson samples at $\sqrt{s} = 13$ TeV. 62
5.8 Cross sections at the NLO in perturbation theory, k-factors and filter efficiencies for W+jets POWHEG+Pythia8 samples at $\sqrt{s} = 13$ TeV. 62
5.9 Cross sections at the NLO in perturbation theory, k-factors and filter efficiencies for top-pair, single top and Wt POWHEG+Pythia6 samples at $\sqrt{s} = 13$ TeV. 63
5.10 Cross sections at NLO in perturbation theory, k-factors and filter efficiency for ttV/ttVV MADGRAPH+Pythia8 samples at $\sqrt{s} = 13$ TeV. 63
5.11 Summary of muon selection. 65
5.12 Summary of electron selection. 66

5.13 Overlap removal criteria adopted in the analyses. Pile-up jets check means JVT > 0.59 if jet $p_{\mathrm{T}} < 60$ GeV and $|\eta| < 2.4$. 68
5.14 Trigger requirement in $\ell^+\ell^-$+$E_{\mathrm{T}}^{\mathrm{miss}}$ analyses in 2015 and 2016 data periods. 68
5.15 List of the event selections. 70
5.16 Expected $Zh \to \ell\ell$ + invisible cutflow yields scaled to 36.1 fb^{-1}. Statistical errors are included. 74
5.17 Uncertainties from PDF, QCD scale, and PS variations on the $Zh \to \ell\ell$ + invisible ($m_h = 125$ GeV) signal acceptance. 75
5.18 Experimental systematic uncertainties on the $Zh \to \ell\ell$ + invisible ($m_h = 125$ GeV) signal acceptance. Up/down means the impact on fianl yields by varying the systematic uncertainties of one standard deviation upwards and downwards 78
5.19 $qqZZ$ and $ggZZ$ yields in signal region for both ee and $\mu\mu$ channel. In each box, first number is central value of yields, second number is statistical uncertainty and third one is systematic uncertainty. . . . 80
5.20 Experimental systematic uncertainties on the $q\bar{q} \to ZZ$ background process. 80
5.21 List of selections applied at the event selection level for the 3lCR. . 81
5.22 The expected number of background and observed number of events in the 3lCRs in $M_T > 60$ GeV and b-jet veto region. The final column shows the scale factor. It is obtained by subtracting other backgrounds (in MC) from the observed events in data, and taking the ratio between this and the expected number of events from the WZ MC. Number of observed events is for an integrated luminosity of 36.1 fb^{-1}. Error is statistical only. 86
5.23 WZ yields in signal region for both ee and $\mu\mu$ channel. First column shows estimates based on MC only, numbers in second column are applied with scale factor $1.29 \pm 0.03 \pm 0.07$. 86
5.24 Event selection applied to define the $e\mu$ Control Region. The control region reflects the SR definition except the opposite flavor requirement of the two selected leptons. 88
5.25 Efficiency factor values in bin of p_{T} and η from Data. Errors contain statistical uncertainty only. 90
5.26 $e\mu$ background yields in signal region for both ee and $\mu\mu$ channel. The first column shows estimates based on MC only, numbers in second column are estimated using data-driven method. Both statistical and systematic uncertainties are included. 90
5.27 Ratios N_A/N_C, N_B/N_D for the ee- and $\mu\mu$-channel. Only the statistical errors shown. Statistical errors due to the MC subtraction are also considered for N_B/N_D (Data). WZ background yields for subtraction from data are rescaled using a scale factor of 1.29. For ZZ background, NNLO QCD & NLO EW corrections are applied. Sherpa 2.2.1 samples are used for the Z+jets background. 92

5.28 Summary of the Z+jets background estimation using the "ABCD" method with statistical and systematic uncertainties. Systematic uncertainties come from the level of correlation in MC, estimated by difference between N_A/N_C (MC) and N_B/N_D (MC), experimental uncertainties on this difference and subtraction of non-Z+jets backgrounds. 92
5.29 Systematic uncertainties sources combine methodology uncertainty and uncertainty on subtraction of non-Z+jets backgrounds from MC. Methodology uncertainty consists of correlation-induced bias $1 - \frac{N_C * N_B}{N_D * N_A}$ including experimental uncertainties (dominated by JetGroupedNP_1&3 5.3.2.4) and uncertainty associated with selection of optimal additional $E_{\mathrm{T}}^{\mathrm{miss}}$and $E_{\mathrm{T}}^{\mathrm{miss}}/H_T$ cuts, estimated by varying the cuts by 40% from their nominal values; both of these sources having roughly equal contribution. 93
5.30 Estimated Z+jets background yields with the one side-band method. Numbers in brackets are from the MC expectation for comparison. Errors are shown for both statistical uncertainty and systematic uncertainty. 94
5.31 Summary of requirements for "Good" and "Bad" leptons 96
5.32 Summary of the requirements used to select a control sample from W+jets MC for fake factor measurement. 97
5.33 Summary of the requirements used to select a control sample from Z+jets MC for fake factor measurement. 97
5.34 W+jets estimation in the electron and muon channel as obtained from the "fake factor" data-driven technique. The systematic uncertainties are calculated as the differences between the W+jets and Z+jets MC-based fake-factors, as well as uncertainty associated with subtraction of non-W+jets backgrounds from MC. 98
5.35 Impact of various uncertainty sources on the physics processes involved in this analysis. For processes labeled with "Yield," the number of events in the signal region is affected (.e.g by uncertainties on the luminosity). For processes labeled with "Acceptance," (e.g. the signal), the cross section is unknown and so the uncertainties will affect the acceptance but not the yield. 99
5.36 The observed data and expected yields in ee and $\mu\mu$ SRs after full event selections for 36.1 fb^{-1}. Estimates include statistical and systematic errors given where available in both MC and data-driven estimations. The data-driven estimation on WZ has a significant impact on total background yields. The statistical and systematic errors on the total background prediction are summed quadratically from each individual process. The "Others" category is composed of ttV and VVV backgrounds. 101

5.37 The 95% CL upper limits on BR($h \to$ inv.) for ee, $\mu\mu$, and ee+$\mu\mu$ channel fits. Both observed and expected limits are presented as well as the $\pm 1\sigma$ and $\pm 2\sigma$ error bands on the expected limit. Only statistical uncertainties are included in the fit. 104
5.38 The 95% CL upper limits on BR($h \to$ inv.) for ee, $\mu\mu$, and ee+$\mu\mu$ channel fits. Both observed and expected limits are presented as well as the $\pm 1\sigma$ and $\pm 2\sigma$ error bands on the expected limit. No significant excess is seen in all channels, and the observed and expected limits are compatible within the error bands. *Both statistical and systematic uncertainties are included in the fit.* 106
5.39 The systematic uncertainty impact on the expected and observed limits for BR($h \to$ inv.) (relative errors). The systematic uncertainties are grouped into different categories. For each repetition of the limit setting, one group is added on top of the stat-only configuration. The difference w.r.t. to the stat-only limit is then taken as the systematic uncertainty impact. 106
5.40 The 95% CL upper limits on $\sigma(pp \to Zh \to \ell\ell + inv.)$ for various values of m_H as obtained from the combined ee+$\mu\mu$ channels. Both observed and expected limits are given, as well as $\pm 1\sigma$ and $\pm 2\sigma$ error bands on the expected limits. No significant excess is seen in all channels, and the observed and expected limits are compatible within the error bands. Full statistical and systematic uncertainties are included in the fit. 107
6.1 Summary of the heavy Higgs signal samples. The cross sections are for Standard Model Higgs Boson of corresponding masses 113
6.2 Summary of the RS graviton samples used in this analysis. 113
6.3 Summary of the event selection for the high mass resonance search. 114
6.4 Cutflow table presenting absolute event counts as well as relative and absolute efficiencies for the $H \to ZZ^* \to \ell^+\ell^-\nu\bar{\nu}$ sample (m_H = 600 GeV). 119
6.5 Theory uncertainties of PDF, QCD and shower variation on acceptance of heavy higgs signals with mass point from 300 GeV to 1400 GeV. 120
6.6 Experimental systematic uncertainties on the $H \to ZZ^* \to \ell^+\ell^-\nu\bar{\nu}$ (with m_H = 600 GeV) signal acceptance. 121
6.7 Overall experimental systematic uncertainties on the acceptance of $H \to ZZ^* \to \ell^+\ell^-\nu\bar{\nu}$ signal with different masses. 121
6.8 Overall experimental systematic uncertainties on the acceptance of RS Graviton signal with different masses. 122
6.9 $qqZZ$ and $ggZZ$ yields in signal region for both ee and $\mu\mu$ channel. In each box, the first number is central value of yields, the second number is statistical uncertainty and the third one is systematic uncertainty. 122
6.10 Experimental systematic uncertainties on the $q\bar{q} \to ZZ$ background process. 123

6.11 WZ yields in signal region for both ee and $\mu\mu$ channel. First column shows estimates based on MC only, numbers in second column are applied with scale factor $1.29 \pm 0.03 \pm 0.07$. 123
6.12 Event selection applied to define the $e\mu$ Control Region. The control region reflects the SR definition except that the opposite flavor requirement of the two selected leptons. 124
6.13 $e\mu$ background yields in signal region for both ee and $\mu\mu$ channel. First column shows estimates based on MC only, numbers in second column are estimated using data-driven method. Both statistical and systematic uncertainties are included. 125
6.14 Ratios N_A/N_C, N_B/N_D for the ee- and $\mu\mu$-channel. Only the statistical errors are shown. Statistical errors due to the MC subtraction are also considered for N_B/N_D (Data). WZ background yields for subtraction from data were rescaled using a scale factor of 1.29 obtained using data-driven estimate. For ZZ background, NNLO QCD & NLO EW corrections were applied. Sherpa 2.2.1 samples are used for the Z+jets background. 125
6.15 Summary of the Z+jets background estimation using the boolean "ABCD" method with statistical and systematic uncertainties. Systematic uncertainties come from the level of correlation in MC, estimated by difference between N_A/N_C [MC] and N_B/N_D [MC], experimental uncertainties on this difference and subtraction of Non-Z+jets backgrounds. 126
6.16 Systematic uncertainties sources combine methodology uncertainty and uncertainty on subtraction of Non-Z+jets backgrounds from MC. Methodology uncertainty consists of correlation-induced bias $1 - \frac{N_C * N_B}{N_D * N_A}$ including experimental uncertainties (dominated by JetGroupedNP_1&3 5.3.2.4) and uncertainty associated with selection of optimal additional $E_{\mathrm{T}}^{\mathrm{miss}}$ and $E_{\mathrm{T}}^{\mathrm{miss}}/H_T$ cuts, estimated by varying them by 40% from their nominal values; both of these sources having roughly equal contribution. 126
6.17 W+jets estimation in the electron and muon channel as obtained from the "fake factor" data-driven technique. The systematic uncertainties are calculated as the differences in the W+jets and Z+jets MC-based fake-factors, as well as uncertainty associated with subtraction of non-W+jets backgrounds from MC. 127
6.18 The observed data and expected yields (scaled to 36.1 fb^{-1}) in ee and $\mu\mu$ signal regions after full event selections. Estimates include statistical and systematic errors given where available in both MC and data-driven estimations. The total background prediction is given in the last row. The statistical and systematic errors on the total background prediction are summed quadratically from each individual process. The "Others" category is composed of ttV and VVV backgrounds. 128

6.19 The observed and expected 95% CL upper limits on production cross-section of additional narrow-width heavy Higgs bosons times the branching fraction of Higgs to ZZ decay $\sigma\times\mathrm{BR}(H \to ZZ^*)$, Limits are derived using ee, $\mu\mu$ and combined ($ee + \mu\mu$) channels, as indicated in the table. Both the statistical and systematic uncertainties are considered in the limit setting. 131
6.20 The observed and expected 95% CL upper limits on the production cross-section of a Randall-Sundrum Graviton times the branching fraction of Graviton to ZZ decay $\sigma\times\mathrm{BR}(G^* \to ZZ)$, shown for mass points between 600GeV and 2TeV. Limits are derived using ee, $\mu\mu$ and combined ($ee+\mu\mu$) channels, as indicated in the table. Both the statistical and systematic uncertainties are considered in the limit setting. 134

ABSTRACT

This dissertation presents searches for dark matter particles and new resonances at the LHC with the ATLAS experiment. The data used in these analyses are produced in proton-proton collisions at a center-of-mass energy of 13 TeV and are collected by the ATLAS experiment, with a total integrated luminosity of 36.1 fb^{-1}.

The experimental signature of new physics in this work involves large missing transverse energy ($E_{\text{T}}^{\text{miss}}$) plus a di-lepton pair from a Z boson decay. In the dark matter search program, it is hypothesized that the Higgs boson may couple to invisible particles who serve as dark matter candidates. The Higgs boson is produced in association with a Z boson, which is used as a 'tag' particle through its charged lepton (ee or $\mu\mu$) decays. The dark matter signature is large $E_{\text{T}}^{\text{miss}}$ since the dark matter particles, just like the neutrinos, escape from the detector (invisible). The challenge of searching for dark matter is to understand sources of $E_{\text{T}}^{\text{miss}}$ produced in proton-proton collisions and design an efficient event selection criterion to separate the signal from the backgrounds. Selected data is compared with the expected background and the dark matter signal, assuming the Standard Model (SM) ZH production cross section. Data is found to be consistent with the background expectation. An upper limit on the branching fraction of the Higgs boson decaying to invisible particles of 67% is set at 95% confidence level (CL). The corresponding limits on the production cross-section (σ) of beyond the SM Zh process with the invisible Higgs boson decays are also presented in a mass range of 110 to 400 GeV.

The two-Higgs-doublet model and the electroweak singlet model are motivated theoretical models, which predict additional Higgs bosons near the TeV scale that may decay to pairs of Z bosons. The search for these non-SM Higgs bosons are also conducted with di-lepton plus $E_{\text{T}}^{\text{miss}}$ final states, but by considering the decay mode $ZZ \to \ell^+\ell^-\nu\bar{\nu}$ ($\ell = e$, or μ). The transverse mass spectrum of the $\ell^+\ell^- + E_{\text{T}}^{\text{miss}}$ system is used as the discriminant to search for bumps created by new resonances. Comparing data with the expected signal and background, no evidence is found for new resonance production in the mass range between 300 GeV to 1500 GeV. Therefore, the limits on new resonance production cross-section times a branching ratio are set. This result is also interpreted as a search for a spin-2 Kaluza-Klein graviton excitation, G_{KK}^*, in the context of the bulk Randall-Sundrum model via $G_{KK}^* \to ZZ^* \to \ell^+\ell^-\nu\bar{\nu}$ process. An upper limit on $\sigma \times \text{BR}(G_{KK}^* \to ZZ^*)$ is set as a function of the KK graviton mass between 600 GeV and 2 TeV.

CHAPTER I

Introduction

This dissertation presents searches for dark matter particles and new resonances at the Large Hadron Collider (LHC) [1] with the ATLAS experiment [2] at CERN, the European Nuclear Research Center.

The research in high energy physics is to address the most fundamental questions: what are the fundamental constituents of matter and how do they interact with each other? Modern physics experiments are conducted at the energy frontier with high energy accelerators. These particle colliders allow us to study the structure of matter at the distance of 10^{-18} m. We use particle accelerators to pump sufficient energy into a point in space to re-create the short-lived particles and uncover the forces and symmetries that existed in the earliest universe. The current most powerful particle collider in the world is the LHC. Researches at the LHC are exploring forces that governed the universe when it was about one trillionth of a second (one picosecond) old.

Our physical world is governed by four fundamental forces: gravitation, the electromagnetic (EM) force, the weak force and the strong force. High energy physics is concerned with the last three of these forces; gravitation is so much weaker than the other three that it has negligible influence on subatomic processes and it is not included in the Standard Model (SM) [4, 5, 6]. The SM consists of three distinct quantum theories: Quantum Electrodynamics (QED), the theory of weak interactions, and Quantum Chromodynamics (QCD) as the theory of strong interactions at high energy. QED and the weak force are unified as the electroweak theory. Before the LHC, predictions made by the SM, in terms of the elementary particles and their interactions, had been verified by experiments, except one scalar particle, the Higgs boson. The electroweak interaction is introduced in the SM by requiring gauge symmetry ($SU(2)_L \times U(1)_Y$). However, invariance under this gauge symmetry requires massless gauge bosons, which conflicts with the observed massive weak interaction

bosons, Z and $W^{\pm}$. During 1964 - 1968 Peter Higgs and Francois Englert introduced a scalar field to the SM [7, 8]. Based on the theory, the electroweak symmetry is spontaneously broken with the choice of a special potential. This potential is the minimum value under the spontaneous symmetry breaking, known as vacuum expectation value. The weak gauge bosons (Z and $W^{\pm}$) acquire their masses through electroweak symmetry breaking process (called Higgs mechanism) by their interactions with the scalar field. The quantum of this field is the Higgs boson. The search for the SM Higgs boson was of high priority in high energy physics experiments over past 50 years till its discovery in 2012 [9, 10] at the ATLAS and the CMS experiments at the LHC.

Even though the last predicted particle in the SM, the Higgs boson, was discovered, some big questions in particle physics remain and cannot be answered in the SM. For example, what is the nature of dark matter in the universe? What is the origin of neutrino masses? Can the fundamental interactions be unified? How can gravity be incorporated? There are also many questions related to the newly discovered Higgs boson, such as: Is it an elementary or composite particle? Will it decay to other final states not predicted by the SM? Does it have other neutral or charged siblings? To address these questions, US Particle Physics Project Prioritization Panel (P5) [11] defined "Science Driver" for the field:

1) Use the Higgs boson as a new tool for discovery;

2) Pursue the physics associated with neutrino mass;

3) Identify the new physics of dark matter;

4) Understand cosmic acceleration: dark energy and inflation;

5) Explore the unknown: new particles, interactions, and physical principles.

The above science driver items 1), 3) and 5) are related to the physics researches in this dissertation: search for dark matter using Higgs boson and new heavy resonances of beyond the SM Higgs boson productions.

Data used in these physics searches are created in proton-proton collisions at the highest center-of-mass energy, 13 TeV, at the LHC and collected by the ATLAS experiment during 2015 and 2016, corresponding to a total integrated luminosity of 36.1 fb^{-1}. The experimental signature of new physics involves large missing transverse energy $E_{\text{T}}^{\text{miss}}$ plus a di-lepton pair (ee, or $\mu\mu$) from a Z boson decay. This thesis will present two analyses:

- A search for dark matter particles in the process of $pp \to Zh \to \ell^+\ell^- + \chi\chi$, where ℓ and χ denote leptons from the Z boson decay and invisible dark matter particles from the Higgs boson decay, respectively;

- Search for additional Higgs bosons in high mass region (300 GeV - 1.5 TeV) in the process $pp \to H^{'}/G^* \to ZZ \to \ell^+\ell^- + \nu\bar{\nu}$, where H' denotes a new Higgs boson, G^* denotes a Randall-Sandrum graviton and ν denotes neutrinos from the Z boson decay.

In the dark matter search program the Higgs boson is used as a new portal that couples to invisible particles as dark matter candidates. The Higgs boson is produced in association with a Z boson, which is used as a "tag" particle through its decays to charged leptons (ee or $\mu\mu$), while the Higgs boson decays to probe dark matter particles. The dark matter gives large missing transverse energy ($E_{\mathrm{T}}^{\mathrm{miss}}$) since the dark matter particle is just like neutrino escaping from the detector (invisible). The previous search with the LHC Run I data collected by the ATLAS experiment set an upper limit on the branching fraction (BR) of the Higgs boson decaying to invisible particles BR($h \to$ inv.) = 75% at 95% confidence level (CL) [12]. With the increased luminosity and energy of the LHC Run II program, this search is expected to increase the sensitivity significantly. The challenge of searching for dark matter at high luminosity is to understand various sources of $E_{\mathrm{T}}^{\mathrm{miss}}$ produced in proton-proton collisions and design an efficient event selection criterion to separate the dark matter signal from backgrounds. The $E_{\mathrm{T}}^{\mathrm{miss}}$ spectrum is used as the discriminant for dark matter searches. A statistical analysis program is performed in the search to quantitatively interpret the final physics results.

There are highly motivated theoretical models, such as the two-Higgs-doublet model (2HDM) [14] and the electroweak singlet model [15, 16], that predict the existence of additional Higgs bosons at higher mass scale. These additional Higgs bosons can decay to pairs of Z bosons. Previous searches with the ATLAS data collected in the LHC Run I presented a negative result [18]. We extend these searches at higher mass range (from 300 GeV to 1.5 TeV) with the LHC Run II data collected at $\sqrt{s} =$ 13 TeV. The search for these additional Higgs bosons are performed with $\ell^+\ell^- + E_{\mathrm{T}}^{\mathrm{miss}}$ final state, considering the decay mode of $H \to ZZ^* \to \ell^+\ell^-\nu\bar{\nu}$ ($\ell = e,\ \mu$). The transverse mass spectrum of the $\ell^+\ell^- + E_{\mathrm{T}}^{\mathrm{miss}}$ system is used as the discriminant to search for a high mass resonance. The major irreducible background comes from the SM ZZ production, which is calculated using Monte Carlo simulations. The reducible background from Z+jets process is estimated from data. This analysis result is also

interpreted in a search for a spin-2 Kaluza-Klein graviton excitation, G^*_{KK}, in the context of the bulk Randall-Sundrum model in $G^* \to ZZ^* \to \ell^+\ell^-\nu\bar{\nu}$ process.

This dissertation is organized as follows: Chapter II gives an overview of the SM of particle physics, including the *Higgs Mechanism*. Theories beyond the SM related to this thesis work and the physics phenomenology at the LHC are also described in this chapter; An overview of the LHC and the ATLAS experiment is presented in Chapter III; Reconstruction of physics objects in the ATLAS experiment, including electrons, muons, jets, $E_{\mathrm{T}}^{\mathrm{miss}}$, and b-tagging, are described in Chapter IV; Chapter V presents the dark matter search analysis and results; Chapter VI presents the searches for new resonances at high mass region; Finally, a summary of the searches is given in Chapter VII.

CHAPTER II

Theory

This chapter describes the particle physics theory, the Standard Model (SM) with emphases on Electroweak theory and Higgs mechanism, followed by descriptions of theoretical models beyond the SM (BSM) related to this thesis work, predictions of non-SM Higgs boson productions at the LHC, and dark matter models.

2.1 The Standard Model of Particle Physics

The SM of particle physics describes the elementary particles and their interactions at the most fundamental level. The theory has been widely tested and can successfully explain a large amount of experimental results with high precision. The recently discovered particle, Higgs boson, has further increased the action of the SM. The elementary particles of matter (fermions in three generations) and the force carriers (vector bosons) as well as the Higgs scalar of the SM are shown in Figure 2.1.

2.1.1 The SM Particles

The building blocks of the SM can be divided into three classes of elementary particles: fermions, gauge bosons and the Higgs boson.

- **Fermions** are spin-$\frac{1}{2}$ particles following the Fermi-Dirac statistics. There are two types of fermions: *leptons* and *quarks*, which are basic components of matter. There are three generations of leptons: electron (e), muon (μ) and tau (τ), each of them has the electric charge of -e,and their corresponding neutrino: electron neutrino (ν_e), muon neutrino (ν_μ) and tau neutrino (ν_τ), which do not carry electric charges. There are also three generations of quarks: up and down quarks as the first generation, charm and strange quarks as the second generation, top and bottom quarks as the third generation. Up, charm and top quarks

have electric charge of $\frac{2}{3}e$, while other three types of quark have electric charge of -$\frac{1}{3}e$. Quarks carry both electric and color charge and thus they can interact with other particles via both the strong interaction and the electromagnetic interaction. Leptons do not carry color charge, they cannot get involved in strong interactions. For neutrinos, they only participate in weak actions, since they do not carry electric charge, therefore cannot have electromagnetic interaction. All the fermions have corresponding antiparticles, which have the same mass, spin, and the same amount but opposite sign of charge as the original particles.

- **Gauge Bosons** are spin-1 particles known as force carriers. There are three types of gauge bosons: photons(γ) that mediate the electromagnetic force between electrically charged particles, $W^{\pm}$ and Z gauge bosons that mediate weak interactions among fermions, and gluons (g) that mediate strong interactions among quarks (colored particles). The photons and the eight gluons are massless. Photons can be described by quantum electrodynamics (QED) while gluons can be described by quantum chromodynamics (QCD). The $W^{\pm}$ gauge bosons carry electric charge and couple to electromagnetic interaction while Z boson is electrically neutral. $W^{\pm}$ and Z bosons along with photons are unified by the electroweak theory in the SM. The electroweak symmetry is broken in the SM so that the Z and $W^{\pm}$ boson can acquire masses in symmetry breaking process, called Higgs mechanism.

- **Higgs Bosons** is a spin-0 massive scalar boson. It is introduced to break the electroweak symmetry to explain how elementary particle acquire masses through their interactions with the Higgs field.

2.1.2 The electroweak theory

The Electroweak theory unifies the electromagnetic and weak interactions mediated by the γ, $W^{\pm}$ and Z bosons. It is based on the $SU(2)_L \times U(1)_Y$ gauge symmetry group, where L refers to the left-handed fields and Y refers to the weak hypercharge. The framework of the theory is built with the Lagrangian, which is presented as the following equation 2.1:

$$\mathcal{L}_{SU(2)_L \times U(1)_Y} = \mathcal{L}_{gauge} + \mathcal{L}_{fermion} + \mathcal{L}_{\phi} + \mathcal{L}_{Yukawa} \tag{2.1}$$

The Lagrangian includes four terms: the gauge fields, the fermion interaction with gauge fields, the scalar fields, and the interaction between fermions and scalar fields.

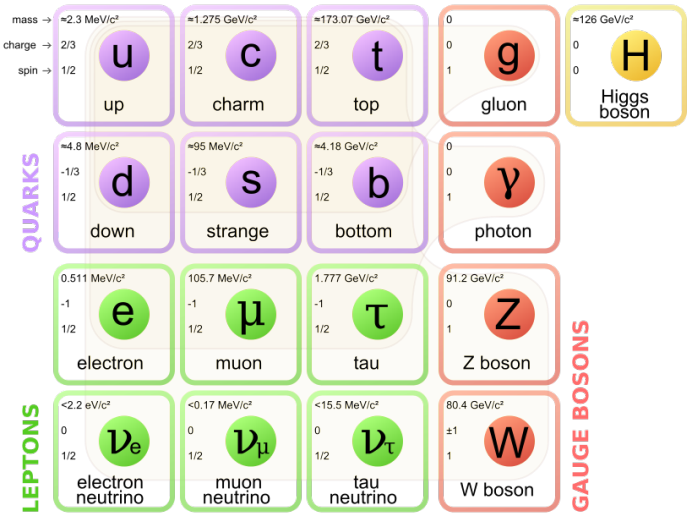

Figure 2.1: Elementary particles in the Standard Model of particle physics [20].

The $\mathcal{L}_{gauge}$ term describes the gauge bosons(γ, $W^{\pm}$, Z) kinetic terms:

$$\mathcal{L}_{gauge} = -\frac{1}{4}W^{i}_{\mu\nu}W^{\mu\nu i} - \frac{1}{4}B_{\mu\nu}B^{\mu\nu}, \tag{2.2}$$

where W^{i}_{μ} (i = 1, 2, 3) and B_{μ} are the $SU(2)_L$ and $U(1)_Y$ gauge fields respectively, with the field strength tensors:

$$\begin{aligned} B_{\mu\nu} &= \partial_{\mu}B_{\nu} - \partial_{\nu}B_{\mu} \\ W^{i}_{\mu\nu} &= \partial_{\mu}W^{i}_{\nu} - \partial_{\nu}W^{i}_{\mu} - g_2\epsilon_{ijk}W^{j}_{\mu}W^{k}_{\nu}, \end{aligned} \tag{2.3}$$

where g_2 is the $SU(2)_L$ gauge coupling and ϵ_{ijk} is the totally anti-symmetric Levi-Civita symbol. The $\mathcal{L}_{fermion}$ term describes the fermion kinetic terms and interactions:

$$\mathcal{L}_{fermion} = \sum_{\psi=L_L,L_R,Q_L,u_R,d_R} \bar{\psi}i\gamma^{\mu}D_{\mu}\psi, \tag{2.4}$$

where γ^{μ} are the 4×4 Dirac matrices, D_{μ} is covariant derivative operator (see equation 2.8), and $\bar{\psi} \equiv \psi^{\dagger}\gamma^{0}$.

In the SM, the fermions form the left-handed weak-isospin doublet and right-handed weak-isospin singlet. The first generation of leptons describe the theory and can be generalized to the second and the third generations by involving the CKM

matrix [22, 23]:

$$L_e = \begin{pmatrix} \nu_L \\ e_L \end{pmatrix}, \qquad \text{and} \qquad R_e = (e_R). \tag{2.5}$$

The left and right handed states are defined by:

$$e_L = \frac{1-\gamma^5}{2}e, \qquad \nu_L = \frac{1-\gamma^5}{2}\nu \qquad e_R = \frac{1+\gamma^5}{2}e, \tag{2.6}$$

where γ^5 is a 4×4 matrix $\begin{pmatrix} 0 & I_{2\times2} \\ I_{2\times2} & 0 \end{pmatrix}$ and $I_{2\times2}$ represents the two-dimensional unit matrix. Similarly, the first generation of quarks can be written as:

$$Q_e = \begin{pmatrix} u_L \\ d_L \end{pmatrix}, \qquad u_R, \qquad d_R. \tag{2.7}$$

In order to keep the gauge invariance under $SU(2)_L \times U(1)_Y$, one must introduce a gauge field B_μ, which transforms as a four-vector and replace the derivatives by gauge-covariant derivatives and a three vector fields W^i_μ. The covariant derivative is introduced as:

$$D^\mu = \partial^\mu - ig_1\frac{Y}{2}B_\mu - ig_2\frac{\tau^i}{2}W^i_\mu, \tag{2.8}$$

where g_1 and g_2 are gauge couplings, Y and τ^i are the generators for the $U(1)_Y$ and $SU(2)_L$ gauge symmetry groups (τ^i does not act on ψ_R), B_μ and W^i_μ are the gauge boson fields. If we re-define the gauge fields as

$$W^+ = \frac{-W^1 + iW^2}{\sqrt{2}}, \quad W^- = \frac{-W^1 - iW^2}{\sqrt{2}}, \quad W^0 = W^3 \tag{2.9}$$

and

$$A_\mu = \frac{g_2B_\mu + g_1W^0_\mu}{\sqrt{g_1^2+g_2^2}}, \quad Z_\mu = \frac{-g_2B_\mu + g_1W^0_\mu}{\sqrt{g_1^2+g_2^2}} \tag{2.10}$$

the electric charge e and weak mixing angle θ_W can be related to the coupling constants g_1 and g_2:

$$e = \frac{g_1g_2}{\sqrt{g_1^2+g_2^2}}, \quad \sin\theta_W = \frac{g_1}{g_1^2+g_2^2}, \quad \cos\theta_W = \frac{g_2}{g_1^2+g_2^2}. \tag{2.11}$$

The Electroweak (EW) Lagrangian for the first generation fermions is:

$$\begin{aligned}\mathcal{L}_{fermion} = & \sum_{f=e,\nu_e,u,d} eQ_f\left(\overline{f}\gamma^\mu f\right)A_\mu \\ & + \frac{g_1}{cos\theta_W}\sum_f \left[\overline{f}_L\gamma^\mu f_L\left(T_f^3 - Q_f sin^2\theta_W\right) + \overline{f}_R\gamma^\mu f_R\left(Q_f sin^2\theta_W\right)\right]Z_\mu \\ & + \frac{g_2}{\sqrt{2}}\left[\left(\overline{u}_L\gamma^\mu d_L + \overline{\nu}_{eL}\gamma^\mu e_L\right)W_\mu^+ + herm.conjugate\right]\end{aligned} \tag{2.12}$$

where Q_f and T_f^3 refers to EM charge and the third component of isospin for each fermion f. The fields A_μ, Z_μ, W_μ^+ and W_μ^- are then identified as photon (γ), the Z, and the $W^\pm$ fields, respectively. All fermions which have electric charge can interact with EM field A_μ, with a strength proportional to their electric charges. The neutrino which has $Q_\nu = 0$ interacts only with Z and $W^\pm$ fields. Also, only left-handed fermions interact with the $W^\pm$ fields. This is due to the fact that right-handed fermions are $SU(2)$ singlets with $T_f^3 = 0$.

The scalar term of the Lagrangian is

$$\mathcal{L}_\phi = (D^\mu\phi)^\dagger D_\mu\phi - V(\phi), \tag{2.13}$$

where $\phi = \begin{pmatrix} \phi^+ \\ \phi^0 \end{pmatrix}$ is a complex Higgs scalar, which is a doublet under $SU(2)_L$. The square of the covariant derivative leads to three and four-point interactions between the gauge and scalar fields. The $V(\phi)$ is the scalar (the Higgs boson) potential. The combination of $SU(2)_L \times U(1)_Y$ invariance and renormalizability restricts $V(\phi)$ to the form

$$V(\phi) = \mu^2\phi^\dagger\phi + \lambda(\phi^\dagger\phi)^2. \tag{2.14}$$

For $\mu^2 < 0$ there will be spontaneous symmetry breaking, the potential will have non-zero ϕ in the ground state. As will be described in the Higgs mechanism section, the weak gauge bosons will acquire masses through the symmetry breaking process, and the λ term describes triple and quartic self-interaction between the scalar fields when expanding around the vacuum expectation value (vev). Vacuum stability requires $\lambda > 0$.

The last term is $\mathcal{L}_{Yukawa}$, which explains how fermions interact with the Higgs field and acquire masses and will be introduced in detail in Section 2.1.3.

The Lagrangian constructed based on $SU(2)_L \times U(1)_Y$ symmetry can completely

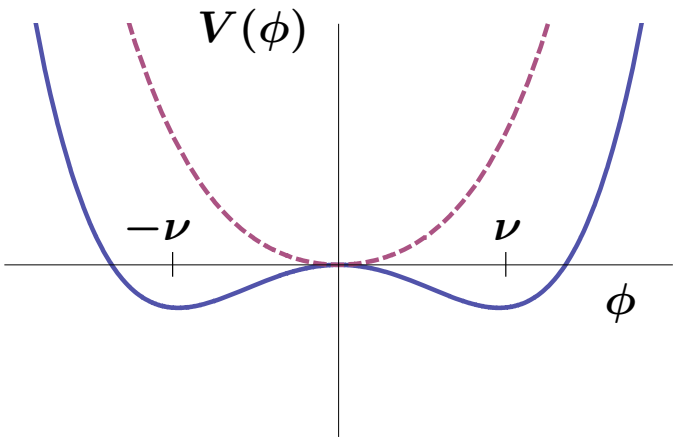

Figure 2.2: The Higgs potential ($V(\phi)$) for $\mu^2 > 0$ (dash line) and $\mu^2 < 0$ (solid line) [21].

describe the EW interactions. However, the fermions and gauge bosons must be massless within this framework, and this conflicts with experimental measurements. Thus, the Higgs mechanism is introduced to explain mass generation through electroweak symmetry broken spontaneously.

2.1.3 The Higgs Mechanism

In this section, the Higgs mechanism is briefly described to explain how fermions and gauge bosons acquire masses.

In the SM, the Higgs scalar field ϕ is a single complex doublet. and the Higgs terms of Lagrangian can be written as:

$$\mathcal{L}_\phi = (D^\mu \phi)^\dagger D_\mu \phi - \mu^2 \phi^\dagger \phi - \lambda(\phi^\dagger \phi)^2. \tag{2.15}$$

When minimizing the potential, the sign of μ^2 has to be considered, as shown in Figure 2.2. For $\mu^2 > 0$, the minimum occurs at $\nu = 0$, which means the vacuum is empty space, and $SU(2)_L \times U(1)_Y$ is unbroken at this point. For $\mu^2 < 0$, the minimum occurs at a nonzero value of vev, $\nu = (-\mu^2/\lambda)^{1/2}$. At this minimum point, the $SU(2)_L \times U(1)_Y$ symmetry is broken spontaneously. We can study the spectrum by expanding ϕ field around the vacuum:

$$\phi(x) = \frac{1}{\sqrt{2}} \begin{pmatrix} 0 \\ \nu + H(x) \end{pmatrix}, \tag{2.16}$$

where the minimum, vacuum ϕ_0 is:

$$\phi_0 = \frac{1}{\sqrt{2}} \begin{pmatrix} 0 \\ \nu \end{pmatrix}. \tag{2.17}$$

The Higgs potential $V(\phi)$ can be rewritten as:

$$V(\phi) = -\frac{\mu^4}{4\lambda} - \mu^2 H^2 + \lambda\nu H^3 + \frac{\lambda}{4} H^4.$$

The second term in $V(\phi)$ represents the mass (at the tree-level) of the physical Higgs boson:

$$M_H = \sqrt{-2\mu^2} = \sqrt{2\lambda}\ \nu,$$

where λ is a parameter of the SM which is not specified in the model. The third and the 4th terms are the Higgs boson self-interaction terms.
The $(D^\mu\phi)^\dagger D_\mu\phi$ term in $\mathcal{L}_\phi$ can be rewritten as:

$$\begin{aligned}(D^\mu\phi)^\dagger D_\mu\phi &= \frac{1}{2}\left(\partial_\mu H\right)^2 + M_W^2 W^{\mu+} W_\mu^- \left(1+\frac{H}{\nu}\right)^2 + \frac{1}{2} M_Z^2 Z^\mu Z_\mu \left(1+\frac{H}{\nu}\right)^2 \\ &= \frac{1}{2}\left(\partial_\mu H\right)^2 + {M_W}^2 W^{\mu+} W_\mu^- + \frac{2{M_W}^2}{\nu} W^{\mu+} W_\mu^- H + \frac{{M_W}^2}{\nu^2} W^{\mu+} W_\mu^- H^2 \\ &\quad + \frac{1}{2}{M_Z}^2 Z^\mu Z_\mu + \frac{{M_Z}^2}{\nu} Z^\mu Z_\mu H + \frac{{M_Z}^2}{2\nu^2} Z^\mu Z_\mu H^2\end{aligned} \tag{2.18}$$

where $M_W = \frac{1}{2}\nu g_2$ and $M_Z = \frac{1}{2}\nu\sqrt{g_1^2 + g_2^2}$. This form of equation explicitly describes the Higgs boson kinetic terms, the mass of $W^\pm$ and Z bosons, the triple (an interaction involves three bosons such as $W^{\mu+}W_\mu^- H$ term) and quartic (an interaction involves four bosons such as $W^{\mu+}W_\mu^- H^2$ term) boson interactions of the $W^\pm$/Z boson with the Higgs boson with coupling constants proportional to the mass of the gauge boson squared.

The fermions also acquire masses by interacting with the Higgs filed and the Lagrangian term is given by:

$$\mathcal{L}^f_{Yukawa} = g_f(\overline{L_f}\phi R_f + \overline{R_f}\phi^\dagger L_f) \tag{2.19}$$

Here, f refers to fermions, which all have similar terms and the coupling g_f is called Yukawa coupling. By inserting the expression of ϕ defined in equation 2.16 into

equation 2.19, one can acquire the fermion mass as:

$$m_f = \frac{\nu g_f}{\sqrt{2}} \tag{2.20}$$

2.1.4 Natural Units

It is common in the realm of the elementary particle physics to redefine units so that speed of light in vacuum (c) and Plank's constant become equal to one: $c = 1$ and ($\hbar$) = 1. In this case, energy, momentum and mass can share the same unit, for example MeV, GeV, TeV.

Conversions between SI units and Natural units are based on:

$$\hbar = 6.58 \times 10^{-25}\ \text{GeV} \cdot \text{s}, \tag{2.21}$$

$$c = 3.00 \times 10^{8}\ \text{m/s}. \tag{2.22}$$

The expressions can provide three useful factor as shown below:

$$1\ \text{GeV}^{-1} = 6.58 \times 10^{-25}\ \text{sec}, \tag{2.23}$$

$$1\ \text{GeV}^{-1} = 0.198\ \text{fm}, \tag{2.24}$$

$$1\ \text{GeV}^{-2} = 3.89 \times 10^{-32}\ \text{m}^2 = 3.89 \times 10^{-4}\ \text{b}. \tag{2.25}$$

2.2 Beyond the Standard Model

2.2.1 Higgs portal in Search for dark matter particles

A large branching fraction of invisible Higgs decay (BR($h \to$ inv.)) can exist in many extensions of the SM. A Higgs boson can decay to dark matter (DM) particles through Higgs portal models [26, 27] as shown in figure 2.3.

Higgs Portal models [28, 29, 30] make a simple, ad-hoc extension to the SM by introducing a new particle χ that couples to only the Higgs boson, with a coupling strength, $\lambda_{h\chi\chi}$. By using the Feynman rules, the Higgs partial width can be deter-

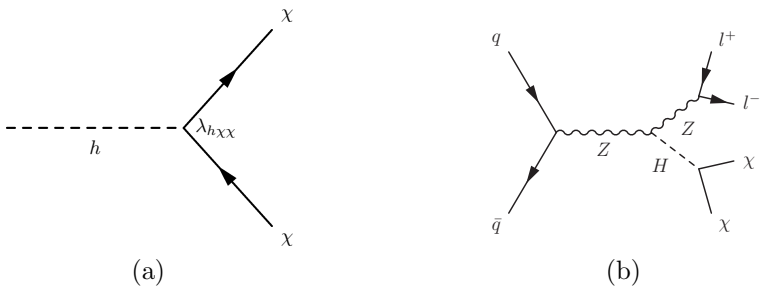

Figure 2.3: Feynman diagrams for the decay of the Higgs boson into dark matter particles (a) and the Higgs boson produced in association with a Z boson (b).

mined in terms of $\lambda_{h\chi\chi}$ and its decay to dark matter particles for the scalar, vector, and fermion cases.

In the SM, the invisible decay of the Higgs boson ($H \to ZZ^* \to \nu\nu\nu\nu$) has a very low branching ratio $\mathrm{BR}_{H\to\mathrm{inv.}}$ of 1.06×10^{-3} for $m_H = 125$ GeV, In this situation, searching for new physics in beyond the SM Higgs invisible decay looks more promising.

2.2.2 BSM Higgs Benchmark Models

Since the Higgs boson was discovered, its properties have been broadly tested using both Run I and Run II datasets at the LHC. The experimental results are so far found consistent with the SM predictions in the measurements of production cross section, couplings to fermions and bosons and spin and CP states of the Higgs boson. Some extensions to the SM that have an extended scalar sector can predict additional heavy Higgs bosons. Physicists want to determine whether this SM Higgs boson is fully responsible for the electroweak symmetry breaking, in other words, that it fully unitarizes the high-energy scattering amplitudes for $V_LV_L \to V_LV_L$, ($V = W$ ($m_W = 80.4$ GeV) or Z ($m_Z = 91.2$ GeV) and $V_LV_L \to f\bar{f}$. If this SM Higgs boson at 125 GeV is not fully responsible for unitarizing the scattering amplitudes, then additional new physics must exist to play the role. Two popular models that predict an additional Higgs boson are the two-Higgs-doublet model [14] and the electroweak-singlet model [15, 16].

2.2.2.1 Electroweak singlet

The electroweak singlet (EWS) model is the simplest extension of the SM Higgs sector. In this model, a heavy singlet is introduced in addition to the SM scalar field

of the original Higgs mechanism. Through the spontaneous symmetry breaking, the EWS can generate two CP-even (charge conjugation parity symmetry-even) Higgs bosons. The lightest of these bosons (h) is considered to be the m_h=125 GeV resonance whose features are assumed to be same as in the SM and can be scaled by a constant κ. The new heavy boson (H) is allowed to have non-SM decays which can be parameterized by the corresponding branching ratio $BR_{H,new}$.

The Lagrangian of this model can be expressed as below:

$$\mathcal{L}^s = (D^\mu \Phi)^\dagger D_\mu \Phi + \partial^\mu S \partial_\mu S - V(\Phi, S), \tag{2.26}$$

where S is an aditional real scalar singlet and $V(\Phi, S)$ is:

$$V(\Phi, S) = -m^2 \Phi^\dagger \Phi - \mu^2 S^2 + \lambda_1 (\Phi^\dagger \Phi)^2 + \lambda_2 S^4 + \lambda_3 \Phi^\dagger \Phi S^2. \tag{2.27}$$

λ_i are the coupling parameters related to the masses (m_h, m_H) and the effective mixing angles (α). The additional parameters m and μ can be constrained by:

$$m^2 = \lambda_1 v^2 + \frac{\lambda_3}{2} x^2, \tag{2.28}$$

$$\mu^2 = \lambda_2 x^2 + \frac{\lambda_3}{2} v^2, \tag{2.29}$$

where v and x are the non-zero vevs of both Higgs field Φ and S. κ and κ' are two scaling constants applied to the SM quantities to get the EWS ones. In order to preserve the coupling to the SM particles, κ and κ' must satisfy the relation

$$\kappa^2 + \kappa'^{\,2} = 1.$$

The features of the EWS are summarized below:

- Cross section of h: $\sigma_h = \kappa^2 \times \sigma_{h,\mathrm{SM}}$
- Width of h: $\Gamma_h = \kappa^2 \times \Gamma_{h,\mathrm{SM}}$
- Branching fraction of h: $\mathrm{BR}_{h,i} = \mathrm{BR}_{h,\mathrm{SM},i}$
- H allowed to have non-SM decays parametrized by $\mathrm{BR}_{H,\mathrm{new}}$
- Cross section of H: $\sigma_H = \kappa'^{\,2} \times \sigma_{H,\mathrm{SM}}$
- Width of H: $\Gamma_H = \frac{\kappa'^{\,2}}{1-\mathrm{BR}_{H,\mathrm{new}}} \times \Gamma_{H,\mathrm{SM}}$
- Branching fraction of H: $\mathrm{BR}_{H,i} = (1 - \mathrm{BR}_{H,\mathrm{new}}) \times \mathrm{BR}_{H,\mathrm{SM},i}$

2.2.2.2 Two Higgs Doublet Model

The two-Higgs doublet model (2HDM) adds an additional doublet to the SM Higgs sector. The lagrangian of 2HDM is built on two doublets Φ_1 and Φ_2 as following:

$$\mathcal{L}_{2HDM} = (D^\mu \Phi_1)^\dagger D_\mu \Phi_1 + (D^\mu \Phi_2)^\dagger D_\mu \Phi_2 + \mathcal{L}_Y - V(\Phi_1, \Phi_2). \tag{2.30}$$

The most general form for scalar potential of two doublets Φ_1 and Φ_2 is [14]:

$$\begin{aligned} V = {} & m_{11}^2 \Phi_1^\dagger \Phi_1 + m_{22}^2 \Phi_2^\dagger \Phi_2 - m_{12}^2 (\Phi_1^\dagger \Phi_2 + \Phi_2^\dagger \Phi_1) + \frac{\lambda_1}{2} (\Phi_1^\dagger \Phi_1)^2 + \frac{\lambda_2}{2} (\Phi_2^\dagger \Phi_2)^2 \\ & + \lambda_3 \Phi_1^\dagger \Phi_1 \Phi_2^\dagger \Phi_2 + \lambda_4 \Phi_1^\dagger \Phi_2 \Phi_2^\dagger \Phi_1 + \frac{\lambda_5}{2} \left[(\Phi_1^\dagger \Phi_2)^2 + (\Phi_2^\dagger \Phi_1)^2 \right]^2, \end{aligned} \tag{2.31}$$

where all the constants are real.

Through the spontaneous symmetry breaking, it generates five physical Higgs bosons:

- Two CP-even particles (h and H)
- A neutral CP-odd particle (A)
- Two charged particles ($H^\pm$)

The Higgs sector of the 2HDM can be described by six parameters:

- the masses of the Higgs bosons: m_h, m_H, m_A, and $m_{H^\pm}$
- $\tan\beta = v_1/v_2$ (v_1 and v_2 are vacuum expectation values of the two doublets)
- α: the mixing angle between the two CP-even bosons

The renormalizable couplings of a single physical Higgs boson to two gauge bosons can be fixed by gauge invariance in terms of the mixing angles in any CP-conserving 2HDM as [14]:

$$g_{hVV} = \sin(\beta-\alpha) g_V \quad g_{HVV} = \cos(\beta-\alpha) g_V \quad g_{AVV} = 0 \quad g_{H^\pm W^\mp Z} = 0 \tag{2.32}$$

where for $V = W, Z$ the Standard Model Higgs couplings are $g_W = g$ and $g_Z = g/\cos\theta_W$, where g is the $SU(2)_L$ gauge coupling and θ_W the weak mixing angle. The

renormalizable couplings of two physical Higgs bosons to a single gauge boson are likewise fixed in any CP-conserving 2HDM as [14]:

$$\begin{aligned} &g_{hZA} = \frac{1}{2} g_Z \cos(\beta - \alpha), \quad g_{HZA} = -\frac{1}{2} g_Z \sin(\beta - \alpha) \\ &g_{hW^\mp H^\pm} = \mp \frac{i}{2} g_Z \cos(\beta - \alpha) \quad g_{HW^\mp H^\pm} = \pm \frac{i}{2} g_Z \sin(\beta - \alpha) \quad g_{AW^\mp H^\pm} = \frac{1}{2} g \end{aligned} \tag{2.33}$$

None of these couplings involve additional assumptions about the form of the full non-renormalizable scalar potential, beyond CP conservation.

Since the Lagrangian of the 2HDM has a very general form, one degree of freedom comes from the choice of the symmetry of its Yukawa sector (which models the interaction of the two fields with the fermions). Φ_1 and Φ_2 are the two fields that are introduced in the Lagrangian to describe the model, and "fermions" means all SM fermions excluding neutrinos. Several types of 2HDM models have been developed depending on this choice and summarized as below:

- Type-I: all vector bosons couple only to Φ_1 and all fermions couple only to Φ_2;
- Type-II: This is an "MSSM-like" model, in which up-type right-handed fermions couple to Φ_2 while down-type right-handed fermions couple to Φ_1,
- Type-III: This is a "lepton-specific" model, where the Higgs bosons have the same couplings to quarks as in the Type I model and to leptons as in Type II.
- Type-IV: This is a "flipped" model, where the Higgs bosons have the same couplings to quarks as in the Type II model and to leptons as in Type I.

2.2.3 Randall-Sundrum Graviton

Gravity is the weakest force of the four fundamental forces of physics, approximately 10^{42} times weaker than the strong force at the scale of quarks, 10^{36} times weaker than the electromagnetic force and 10^{29} times weaker than the weak force at the scale of protons/neutrons. In order to solve such hierarcy problem, in 1999, Lisa Randall and Raman Sundrum proposed a new higher-dimensional mechanism [32], which relies on the existence of only a single additional dimension. This model assumes our world is a 5-dimensional one described by warped geometry. Based on the Randall-Sundrum (RS) framework with a warped a extra dimension, the most distinctive novel feature of this scenario is the existence of spin-2 Kaluza-Klein (KK) gravitons [33] whose masses and couplings to the SM are set by the TeV scale.

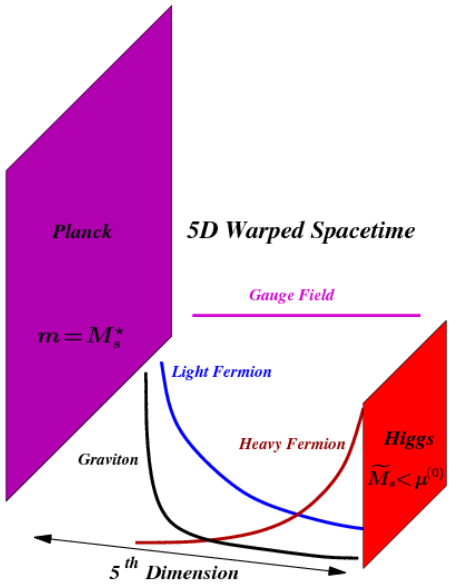

Figure 2.4: Schematic representation of the RS warped model of hierarchy and flavor [33].

A general formula for the couplings of a bulk filed to the KK gravitons is:

$$\mathcal{L}_G = C\frac{1}{\bar{M}_P}\eta^{\mu\alpha}\eta^{\nu\beta}h_{\alpha\beta}(x)T_{\mu\nu}(x) \tag{2.34}$$

where $h_{\alpha\beta}(x)$ corresponds to the KK graviton, $T_{\mu\nu}(x)$ denotes the $4D$ energy-momentum tensor of the modes of the bulk field and $\eta^{\mu\alpha}$ is the metric tensor, $\bar{M}_P \approx 2.4 \times 10^{18}$ GeV is the reduced $4D$ Planck scale and C is the overlap integral of the wave functions of the graviton and the bulk fields.

In this scenario, the production of graviton via $q\bar{q}$ annihilation and decays to the conventional photon and lepton channels are highly suppressed. However, the graviton production via gluon fusion followed by decay to longitudinal Z/W can be significant. In particular, the "golden" ZZ decay mode offers a distinctive 4-lepton signal that could lead to the observation at the LHC. This is because in the RS model, the entire SM are assumed to be localized on the TeV brane. The key feature of this model is that KK gravitons have a mass TeV and are localized near the TeV brane so that KK graviton coupling to the entire SM is only TeV suppressed. A schematic representation of this setup is shown in Figure 2.4. Hence, KK graviton production via $q\bar{q}$ or gg fusion at the LHC followed by decays to dileptons or diphotons gives striking signals.

2.3 Physics Phenomenology at the LHC

2.3.1 Hadronic Collisions

LHC is a machine built for proton-proton (pp) collision. A proton consists of partons: quarks and gluons. For the pp collisions at the LHC, the parton interactions can be divided into hard and soft scattering processes depending on the momentum transferred between partons. A pp collision event at the LHC can be illustrated in Figure 2.5.

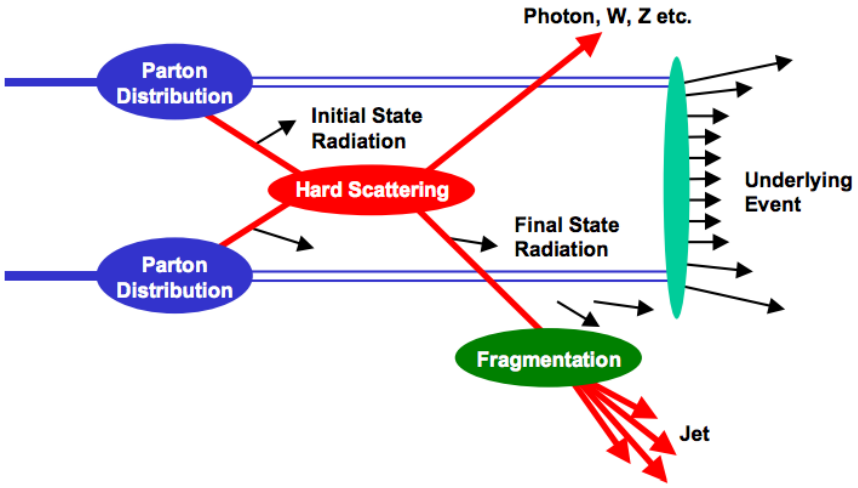

Figure 2.5: Schematic view of a hadron-hadron collision [37].

The theoretical model for an event from hadron-hadron collisions is described below:

- **Parton Distribution Function (PDF)** quantifies the probability of finding a certain type of quark or gluon with momentum fraction x at an energy scale Q. Figure 2.6 shows the measured PDFs of gluons and quarks in NNPDF3.0 which is accurate in perturbative QCD at next-to-next-to leading order (NNLO) [35].

- **Hard Scattering** shows the event produced by parton interactions. A hard scattering process transfers large momentum among partons, which could be either a violent scatter or creation of of a large mass system. For example, the Higgs boson production from the gluon-gluon fusion and the final state of Higgs boson decay for underlying physics process such as vector bosons or quark pairs.

- **Jet Fragmentation** produces the hadronic jets in the final state from the partons (quarks and gluons) which are produced in the hard scattering.

- **Initial and Final State Radiation** represents the QCD, in form of gluons, or QED, in form of photons, radiation from incoming and outgoing particles.
- **Underlying Event** contains the particles produced by proton remnants.

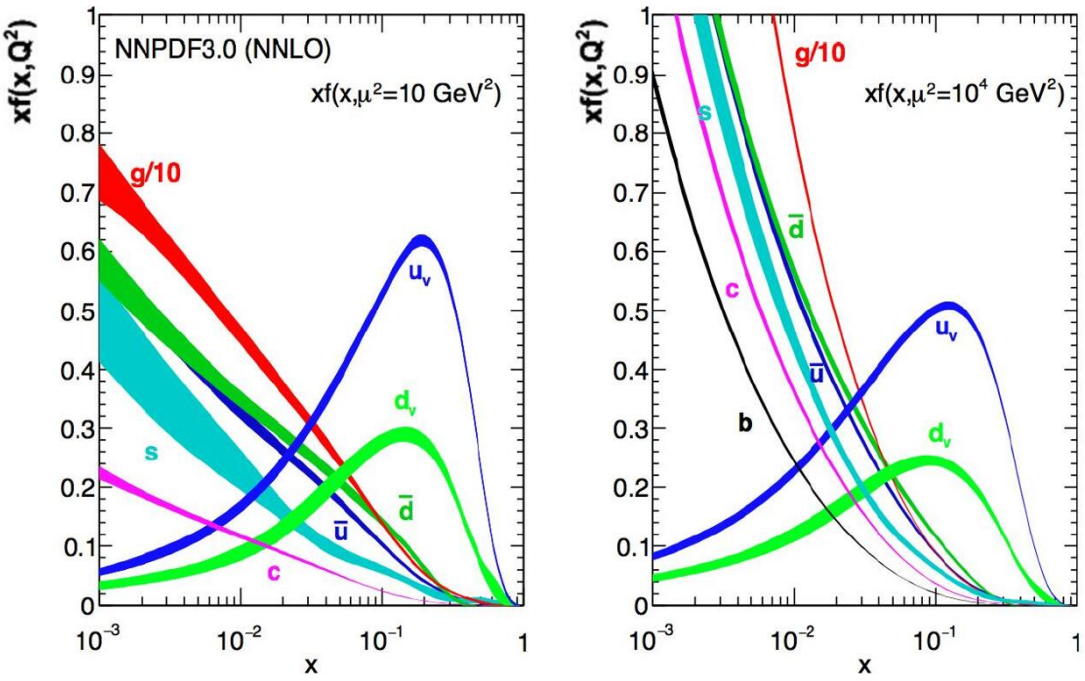

Figure 2.6: NNPDF3.0 NNLO PDF set for $Q^2 = 10$ GeV^2 and $Q^2 = 10^4$ GeV^2 [38].

One of the physical quantities to connect the theory and experimental measurement is the cross section (σ) for a certain physics process. According to the QCD *factorization theorem* [36] the cross sections for hard scattering can be factorized into a parton level hard scattering convoluted with the parton distribution functions. For example, for the scattering of two hadrons A and B producing a final state X, a general form to calculate the hadronic cross section can be written as:

$$\sigma_{AB} = \int dx_a dx_b \; f_{a/A}(x_a, \mu_F^2) f_{b/B}(x_b, \mu_F^2) \; \hat{\sigma}_{ab\to X}(\alpha_S, \mu_R, \mu_F) \; . \tag{2.35}$$

where μ_F is the *factorization* scale, which can be understood as the scale that separates the short- and long-distance physics and μ_R is the renormalization scale for the QCD running coupling. $f_{a/A}(x_a, \mu_F^2)$ and $f_{b/B}(x_b, \mu_F^2)$ represent the PDF for the incoming particles. $\hat{\sigma}_{ab\to X}(\alpha_S, \mu_R, \mu_F)$ is the parton level cross section, which can be

calculated perturbative in QCD, in form of fixed-order expansion in α_S

$$\hat{\sigma}_{ab\to X}(\alpha_S, \mu_R, \mu_F) = (\alpha_S)^n[\hat{\sigma}^{(0)} + (\alpha_S/2\pi)\hat{\sigma}^{(1)}(\mu_F, \mu_R) + (\alpha_S/2\pi)^2\hat{\sigma}^{(2)}(\mu_F, \mu_R) + ...], \tag{2.36}$$

where $\hat{\sigma}^{(0)}$ denotes the leading-order (LO) partonic cross section, and $\hat{\sigma}^{(1)}$ is the next-to-leading-order (NLO), $\hat{\sigma}^{(2)}$ for NNLO.

The choices of μ_F and μ_R are arbitrary. To avoid unnaturally large logarithms reappearing in the perturbation series it is sensible to choose μ_F and μ_R values in the order of the typical momentum scales of the hard scattering process. And $\mu_F = \mu_R$ is often assumed. Taking the Higgs production through gluon-gluon fusion and decay to $ZZ^\star$ as an example, the standard choice is $\mu_F = \mu_R = \frac{m_{ZZ^\star}}{2}$

2.3.2 Monte Carlo event generator

Monte Carlo (MC) event generators are software that simulate particle physics events using Monte Carlo methods. The MC event generators play a crucial role throughout the whole process of an experiment, including the design of the experiment, detector simulation and calibration, data analysis and comparison of the experimental results and theoretical predictions. The structure of a proton-proton collision at the LHC as built up by event generators can be described by a few main steps, as illustrated in 2.7.

Here lists some typical MC generators used for the new physics searches in this thesis:

- `Pythia6` [**40**]: Multi-purpose LO generator mostly used for QCD final states.
- `Pythia8` [**41**]: The successor to Pythia6.
- `MadGraph` [**42**]: Automation of the computations of tree-level and NLO cross sections and matching to parton shower simulations.
- `Sherpa` [**43**]: Multi-parton Matrix Element (ME) + Parton Shower (PS) generator, including hadronization.
- `PowhegBox` [**44**]: It creates events at NLO in QCD, and can be used standalone to produce `LHE` files which can be passed to `Pythia8`, `Herwig++`, or `HERWIG+Jimmy` for parton showering.
- `gg2VV` [**45, 46**]: Parton-level integrator and event generator for $gg(\to H) \to VV$ processes.

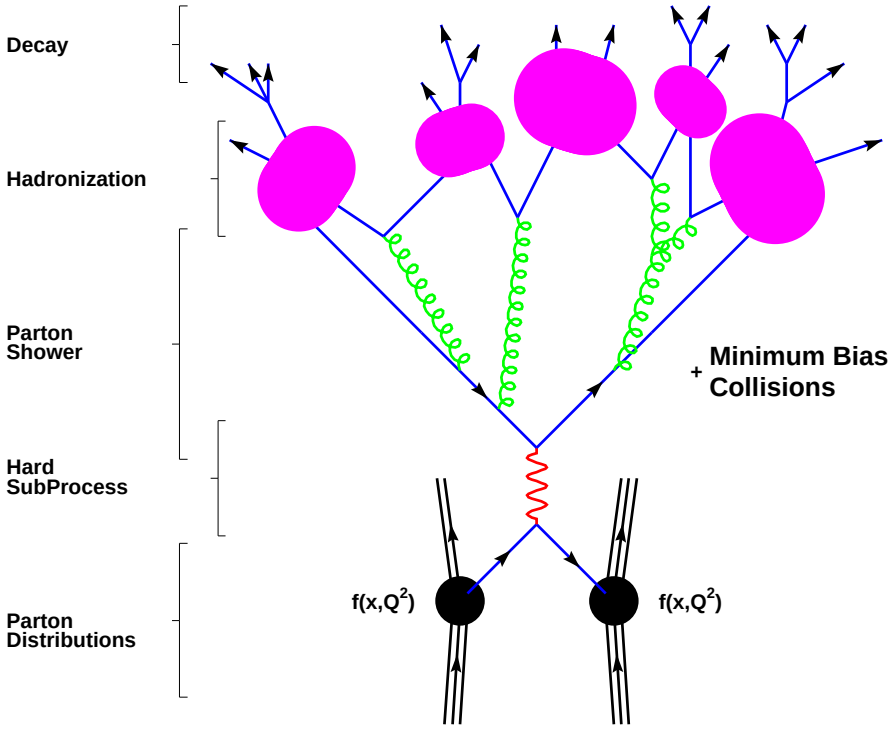

Figure 2.7: The basic structure of a showering and hadronization generator event is shown schematically [39].

CHAPTER III

The Large Hadron Collider and the ATLAS Experiment

The Large Hadron Collider (LHC) [1] is the largest and the most powerful particle collider, the most complex experimental facility ever built, and the largest single machine in the world. It was built by the European Organization for Nuclear Research (CERN) between 1998 and 2008 in collaboration with over 10,000 scientists and engineers from over 100 countries. It lies in a tunnel 27 kilometers (17 mi) in circumference, as deep as 175 meters (574 ft) beneath the France-Switzerland border near Geneva. On the circle of the LHC, there lies four major experiments, ALICE [48], ATLAS [2], CMS [3] and LHCb [49]. The ATLAS experiment, utilzied in this thesis, is a multi-purpose detector, designed to take advantage of the unprecedented energy available at the LHC and observe phenomena that involve highly massive particles which were not observable using earlier lower-energy accelerators. Along with CMS, ATLAS was one of the two LHC experiments involved in the discovery of the Higgs boson in July 2012. It was also designed to search for evidence of particle physics beyond the Standard Model (BSM). In this chapter, a brief description of LHC is given in section 3.1 and followed by an introduction to major part of the ATLAS detector in section 3.2

3.1 The Large Hadron Collider

3.1.1 The LHC Complex

The accelerator complex at CERN, shown in Figure 3.1 [47] is a succession of machines that accelerate particles to increasingly higher energies. Each machine boosts the energy of a beam of particles before injecting the beam into the next machine in the sequence. In the LHC, the last element in this chain, particle beams

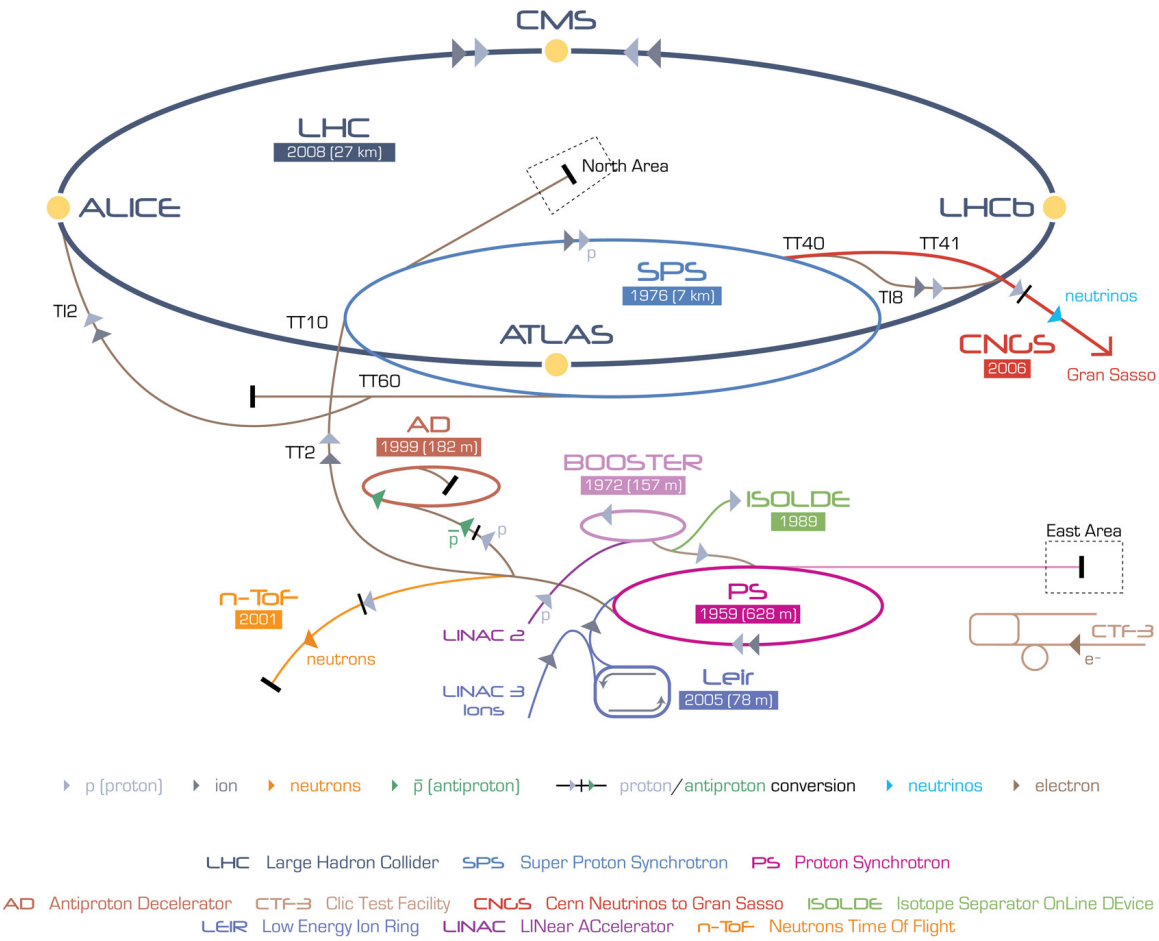

Figure 3.1: Distribution of the LHC complex [47].

are accelerated up to the record energy of 6.5 TeV per beam. Most of the other accelerators in the chain have their own experimental halls where beams are used for experiments at lower energies.

Inside the accelerator, two high-energy particle beams travel at close to the speed of light before they are made to collide. The beams travel in opposite directions in separate beam pipes - two tubes kept at ultrahigh vacuum state. They are guided around the accelerator ring by a strong magnetic field maintained by superconducting electromagnets. The electromagnets are built from coils of special electric cable that operates in a superconducting state, efficiently conducting electricity without resistance or loss of energy. This requires chilling the magnets to -271.3°C - a temperature colder than outer space. For this reason, majority of the accelerator is connected to a distribution system of liquid helium, which cools the magnets, as well as to other supply services.

The proton source is a simple bottle of hydrogen gas. An electric field is used to strip hydrogen atoms of their electrons to yield protons. Linac 2, the first accelerator in the chain, accelerates the protons to the energy of 50 MeV. The beam is then injected into the Proton Synchrotron Booster (PSB), which accelerates the protons to 1.4 GeV, followed by the Proton Synchrotron (PS), which pushes the beam to 25 GeV. Protons are then sent to the Super Proton Synchrotron (SPS) where they are accelerated to 450 GeV. These protons are finally transferred to the two beam pipes of the LHC. The beam in one pipe circulates clockwise while the beam in the other pipe circulates anticlockwise. It takes $20 \sim 30$ minutes for the protons to reach their maximum energy of 6.5 TeV and both two beams circulate for many hours inside the LHC beam pipes under normal operating conditions. The two beams are then brought into collision inside four detectors: ALICE, ATLAS, CMS and LHCb, where the total energy at the collision point is equal to 13 TeV. The four detectors where collisions occur are summarized below:

- **ALICE** (**A** **L**arge **I**on **C**ollider **E**xperiment): A heavy ion experiment designed to study the nature of quark-gluon plasma.
- **ATLAS** (**A** **T**oroidal **L**HC **A**pparatu**S**): One of two general-purpose detectors to study a wide range of physics from testing the SM Higgs boson to looking for new physics such as dark matter and etc..
- **CMS** (**C**ompact **M**uon **S**olenoid): The other general-purpose detector, like ATLAS, to study the SM including the Higgs boson and look for clues of new physics.
- **LHCb** (**L**arge **H**adron **C**ollider **b**eauty): A specialized b-physics experiment designed to slight differences between matter and antimatter by studying b-hadrons.

3.1.2 LHC Design Parameters

The collider is designed to create proton-proton collisions with a peak luminosity of 10^{-34} cm^{-2}s^{-1} and a center-of-mass energy of $\sqrt{s} = 14$ TeV. The momentum of a proton in a circular accelerator is determined by:

$$p[\text{GeV}] = 0.3B[\text{T}]\rho[\text{m}], \tag{3.1}$$

where B is the magnetic field strength and ρ is the radius of the circle. In order to reach the center-of-mass energy at the LHC, the magnetic field strength has to reach 8.3 T. 1232 dipole magnets are used to keep the beams on circular path and 392 quadrupole magnets are used to focus the beams. In total, over 1600 superconducting magnets are installed.

The events are produced by beam-beam collisions at a rate of:

$$\frac{dN}{dt} = L \times \sigma, \tag{3.2}$$

where L is the instantaneous luminosity and σ is the cross section. Luminosity is an important parameter to describe the performance of the LHC. It has the dimension of number of particles or events per time per area and thus has the unit of $\mathrm{cm}^{-2}\mathrm{s}^{-1}$. In practice, L is dependent on the particle beam parameters [50] , such as beam width and particle flow rate, as well as the target properties, such as target size and density. Assuming a Gaussian beam distribution, the luminosity can be expressed as:

$$L = \frac{N_b^2 n_b f_r e v \gamma_r}{4\pi\epsilon_n \beta^*} F, \tag{3.3}$$

where N_b is the number of particles per bunch, n_b is the number of bunches per beam, f_r the revolution frequency, γ the relativistic γ factor, ϵ_n the normalized transverse beam emittance, β^* the β function (to describe beam width) at the collision point and F the geometrical luminosity reduction factor. The geometric luminosity reduction factor is added in the luminosity calculation due to the crossing angle at the interaction point (IP, the point where two bunch of protons collide with each other), which can be expressed as:

$$F = \frac{1}{\sqrt{1 + (\frac{\theta_c \sigma_z}{2\sigma^*})^2}}, \tag{3.4}$$

where θ_c is the full crossing angle at the IP, σ_z the root mean square (RMS) of the bunch length and σ^* the transverse RMS of the beam size at the IP.

The integrated luminosity is the integral of luminosity over a period of time, and can be written as:

$$L_{int} = \int L dt, \tag{3.5}$$

which has the dimension of cm^{-2}. In this thesis, it is expressed in the unit of inverse femtobarn (fb^{-1}, $\mathrm{fb}^{-1} = 10^{39}\ \mathrm{cm}^{-2}$) and measures the number of events produced per fb cross section. The integrated luminosity of pp collisions delivered by the LHC and

recorded by the ATLAS detector in 2015 and 2016 are shown in Figure 3.2.

Table 3.1 [54] shows the main parameters required to reach a peak luminosity of 10^{34} cm^{-2}s^{-1} for proton-proton collisions at $\sqrt{s} = 14$ TeV.

Circumference	26.7 km
Beam energy at collision	7 TeV
Beam energy at injection	0.45 TeV
Dipole field at 7 TeV	8.33 T
Luminosity	10^{34}cm^{-2}s^{-1}
Beam current	0.56 A
Protons per bunch	1.1×10^{11}
Number of bunches	2808
Nominal bunch spacing	24.95 ns
Normalized emittance	3.75μm
Total crossing angle	300μrad
Energy loss per turn	6.7 keV
Critical synchrotron energy	44.1 eV
Radiated power per beam	3.8 kW
Stored energy per beam	350 MJ
Stored energy in magnets	11 GJ
Operating temperature	1.9 K

Table 3.1: The LHC parameters.

At the LHC, the average number of pp interactions per bunch crossing is often referred as pile-up parameter (μ). The collision events from pileup are uncorrelated with the hard-scattering process and often poses an contamination to the soft energy deposits, leading to an adverse effects on the objects reconstruction. The pileup parameter can be calculated from the integrated luminosity over a bunch crossing time as:

$$\mu = \int_0^{t^{\text{crossing}}} Ldt \times \sigma_{\text{inelastic}}, \tag{3.6}$$

where $\sigma_{\text{inelastic}}$ is inelastic interaction cross section, which takes value of 78 mb at the center-of-mass energy of $\sqrt{s} = 13$ TeV.

Figure 3.3 shows the integrated luminosity versus the mean number of interactions per crossing averaged over all bunch crossings (denoted as $< \mu >$) for the 2015, 2016 pp runs.

Table 3.2 presents some highlighted LHC beam parameter values under operational conditions of the pp collision during Run 1 (2010-2012) and Run 2(2015-2016).

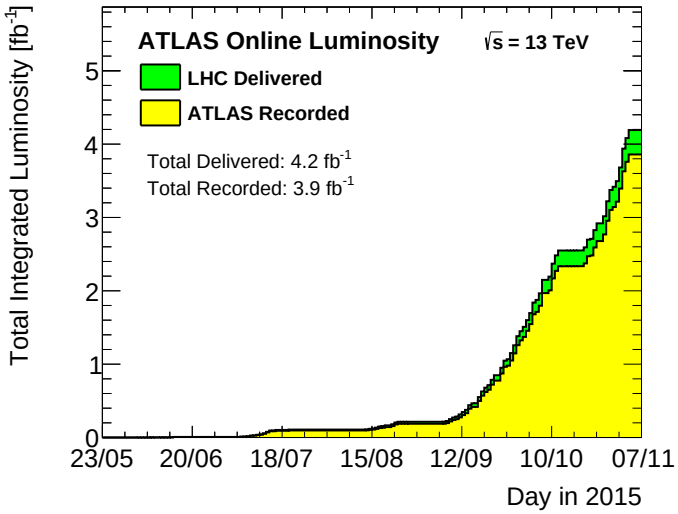

(a)

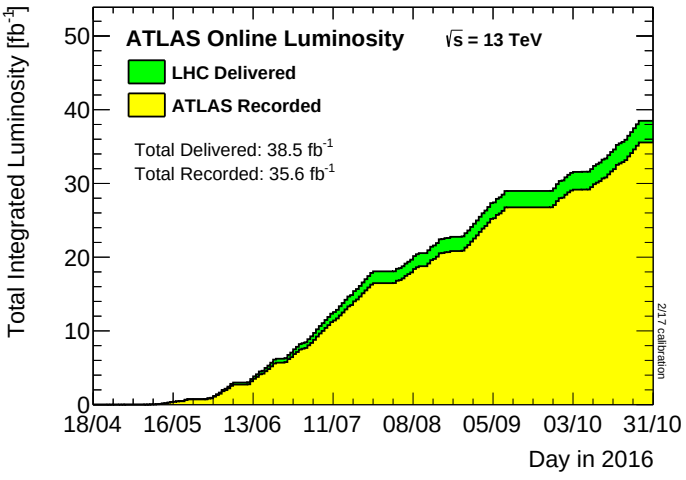

(b)

Figure 3.2: The cumulative luminosity versus time delivered by the LHC (green) and recorded by the ATLAS (yellow) during stable proton-proton beam periods at the center-of-mass energy of $\sqrt{s} = 13$ TeV in 2015 (left) and 2016 (right) [51].

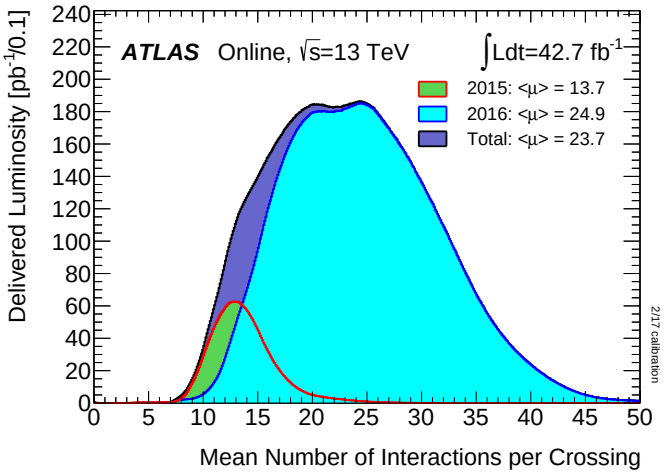

Figure 3.3: Luminosity-weighted distribution of the mean number of interactions per crossing in the 2015 and 2016 pp collision data [51].

Parameter	Design	2010	2011	2012	2015	2016
Beam energy [TeV]	7.0	3.5	3.5	4	6.5	6.5
Bunches/beam n_b	2808	348	1331	1380	2244	2220
Bunch crossing time t_{crossing} [ns]	25	150	50	50	25	25
Protons/bunch N_b [10^{11} protons]	1.15	0.9	1.2	1.7	1.1	1.1
ϵ_n [μ m]	3.75	2.6	2.4	2.4	3.5	3.4
β function at IP β^* [m]	0.55	2.0-3.5	1.0-1.5	0.6	0.8	0.4
Peak luminosity [10^{34} cm^{-2}s^{-1}]	1.0	0.02	0.36	0.77	0.51	1.4
$< \mu >$	25	2	9	21	14	25
$N = \int Ldt$ LHC delivered [fb^{-1}]		0.047	5.5	22.8	4.2	38.5

Table 3.2: The LHC operational conditions in Run I (2010-2012) and in Run II (2015-2016).

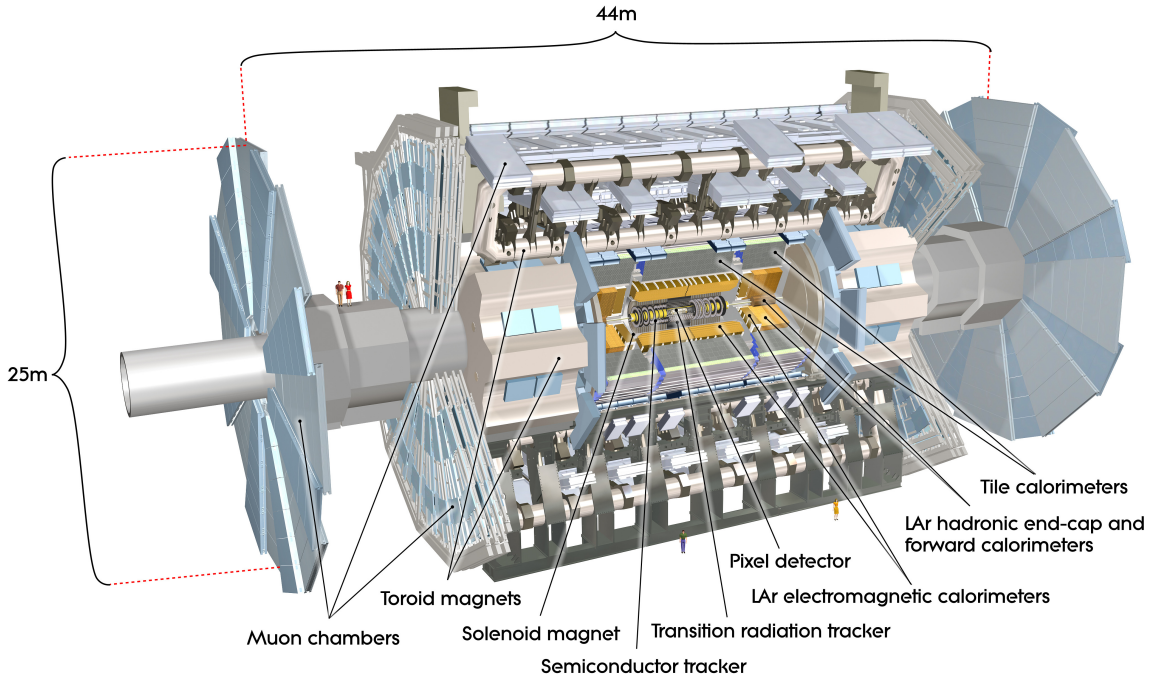

Figure 3.4: The longitudinal cut-away view of the ATLAS detector [52].

3.2 The ATLAS Experiment

The ATLAS detector is a multi-purpose machine to probe different particles. It is composed of four major parts: the inner detector (ID), the electromagnetic (EM) and hadronic calorimeter, the muon spectrometer (MS) and the magnet systems. The layout of the ATLAS detector is shown in Figure 3.4

The coordinate system used in the ATLAS detector is the right-handed Cartesian coordinate system with its origin at the interaction point (IP), the center of the detector. The $z-$axis points to the beam direxion, the $x-$axis points from the IP to the center of LHC ring and the $y-$axis points upward. The side-A and side-C of the detector are defined with positive z and negative z respectively. The polar angle θ measures the angle from the beam axis and the azimuthal angle ϕ is measured around the beam pipe. $\phi = 0$ corresponds to the positive x-axis and increases clockwise when looking into the positive z-axis direction. The pseudorapidity is defined as η = -ln tan(θ/2), in case of massive objects such as jets, the rapidity is used $y = \frac{1}{2}\ln(\frac{E+p_Z}{E-p_Z})$. The distance ΔR is the pseudorapidity-azimuthal angle space defined as $\Delta R = \sqrt{\Delta\eta^2 + \Delta\phi^2}$. The momentum projected to x-y plane is defined as transverse momentum p_T, as well as missing transverse energy $E_{\mathrm{T}}^{\mathrm{miss}}$. As a multi-purpose detec-

tor, the ATLAS should be capable of recognizing various particles in the final states, including electron (e), muon (μ), tau (τ), photon (γ), jets (j) and etc.. To achieve this goal, the ATLAS detector should meet the design criteria summarized as below:

- Excellent EM calorimeter for e and γ ID and energy measurements and hadronic calorimeter for accurate jet and $E_{\mathrm{T}}^{\mathrm{miss}}$ measurements.
- Efficient tracking at high luminosity for high-p_T leptons, e and γ ID, τ and heavy flavor ID and full event reconstruction at low luminosity.
- High-precision muon spectrometer for accurate measurements of μ momentum at the high luminosity.
- Large acceptance in pseudorapidity with almost full azimuthal angle coverage.
- Efficient triggering system to record the particles of interest at low-p_T thresholds, as well as the efficiency at high pile-up.

3.2.1 Inner Detector

The ATLAS Inner Detector (ID), also known as inner tracking system, combines high-resolution detectors at the inner radii with continuous tracking elements at the outer radii, all contained in the Central Solenoid, which provides a nominal magnetic field of 2 T. The highest granularity is achieved around the vertex region using semiconductor pixel detectors followed by a silicon micro-strip detector. Typically for each track the pixel detector contributes three and the strips four space points. At larger radii, 36 tracking points are provided by the straw tube tracker. The relative precision of the measurement is well matched, so that no single measurement dominates the momentum resolution. The layout of the ID is shown in Figure 3.5, three major parts of ID, the Pixel Detectors, the Semiconductor Tracker (SCT) and the Transition Radiation Tracker (TRT) are introduced below.

3.2.1.1 Pixel Detector

The Pixel detector [55], the innermost part of the ID, provides a very high granularity, high precision set of measurements as close to the interaction point as possible. Its active part consists of three barrel layers at radii of 4.3 cm, 10.1 cm and 13.2 cm from the center. The basic unit of the pixel detector is the module. A module is a rectangular active device approximately 6cm by 2 cm with 46080 pixels, each 50 μm in azimuth by 400 μm along the beam. All modules are arranged in 3 concentric

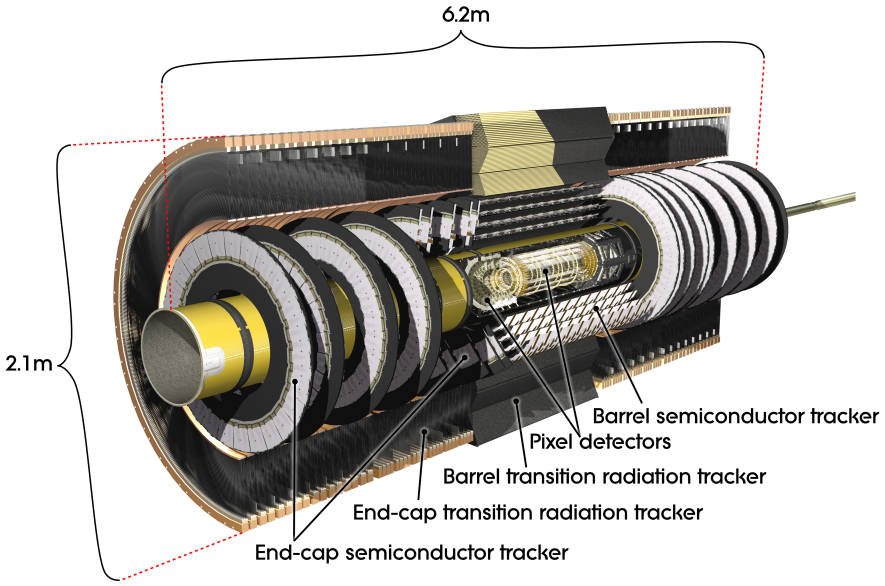

Figure 3.5: The cut-away view of the ATLAS Inner Detector [52].

cylinders with the axis along the beam (the barrel) at radii of 5 cm, 9 cm and 12 cm from the center, known as B-layer, layer 1, layer 2, plus 3 disks concentric with the beam at each end of barrel. There are 1456 barrel modules and 288 disk modules covering pseudorapidity $\eta < |2.5|$.

During the LHC first long shutdown from 2013-2014, the detector was extracted from the experiment to repair the modules and install an Insert-able B-Layer (IBL). The IBL is a fourth layer of the pixel detectors, and has been installed between the existing Pixel Detector and a new smaller radius beam-pipe at a radius of 3.3 cm to improve the vertex resolution and b-tagging efficiency.

3.2.1.2 Semiconductor Tracker

The Semiconductor Tracker (SCT) [56] is the middle component of the ID. It is designed to provide eight precision measurements per track in the intermediate radial range, contributing to the measurement of momentum, impact parameter and vertex position. In the barrel region of SCT, eight layers of the silicon micro-strip detectors provide four space points in the r-ϕ and z coordinates crossed by each track. The barrel modules are mounted on carbon-fibre cylinders at radii of 30.0, 37.3, 44.7, and 52.0 cm. In the end-cap region, the detectors have a set of strips running radially and a set of stereo strips at an angle of 40 mrad, with mean pitch of approximately 80 mm.

3.2.1.3 Transition Radiation Tracker

The Transition radiation Tracker (TRT) [57] is based on the use of straw detectors, which can operate at the expected high rates due to their small diameter and the isolation of the sense wires within individual gas volumes. The maximum straw length is is 144 cm in the barrel, which contains about 50,000 straws, each divided in two at the center and with the readout at both ends, to reduce the occupancy. The end-caps contain 320,000 radial straws, with the readout at the outer radius. Each channel provides a drift time measurement, giving a spatial resolution of 170 μm per straw, and two independent thresholds. These allow the detector to discriminate between tracking hits, which pass the lower threshold, and transition radiation hits, which pass the higher one.

3.2.2 Calorimeter

The ATLAS Calorimeter, as shown in Figure 3.6, is built on three subsystems: an EM calorimeter (ECal) covering the pseudorapidity range of $|\eta| < 1.475$ in the barrel region and $1.375 < |\eta| < 3.2$ in the end-cap regions, a hadronic calorimeter (HCal) covering $|\eta| < 1.7$ for the barrel and $1.5 < |\eta| < 3.2$ for the end-caps and a forward calorimeter (FCal) covering $3.1 < |\eta| < 4.9$.

3.2.2.1 Electromagnetic Calorimeter

The ATLAS EM calorimeter [58] is a lead-liquid argon (LAr) sampling detector with accordion-shaped electrodes and lead absorber plates over its full coverage. It consists of a barrel part and two end-cap parts. The barrel part consists of two identical half-barrels, separated by a small gap (4 mm) at $z = 0$. Each end-cap part is divided into two coaxial wheels: an inner wheel covering $1.375 < |\eta| < 2.5$ and an outer wheel covering $2.5 < |\eta| < 3.2$. With the accordion geometry, the EM calorimeter can provide complete ϕ symmetry without azimuthal cracks. The lead thickness in the absorber plates is optimized as a function of η in terms of EM calorimeter performance in energy resolution, with a typical 2 mm thickness over a large area. The LAr gap thickness is 2.1 mm in the barrel region, while changing with radius with range of 0.9 - 3.1 mm in the end-cap region. Within the full range, the EM calorimeter is divided into three sections in the barrel part and two sections in each end-cap part in depth respectively, with finely segmented η and ϕ. In the region of $|\eta| < 1.8$, a presampler detector is installed to correct for the energy lost by electrons and photons upstream of the calorimeter. The presampler consists of an

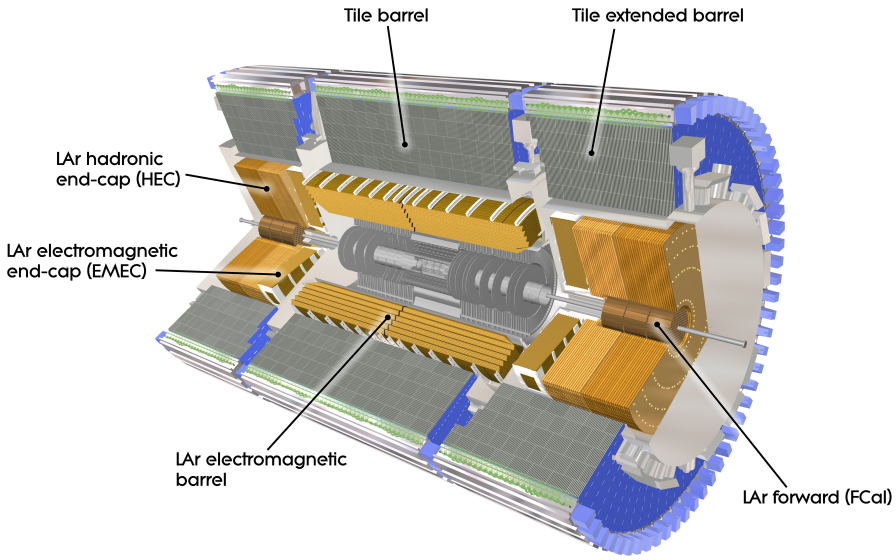

Figure 3.6: The cut-away view of the ATLAS Calorimeter [52].

active LAr layer of thickness 1.1 cm (0.5 cm) in the barrel (end-cap) region.

3.2.2.2 Hadronic Calorimeter

The ATLAS hadronic calorimeter consists of three parts: the tile calorimeter [59], the liquid-argon hadronic end-cap calorimeter (HEC) [60] and the liquid-argon forward calorimeter (FCal) [61].

- **Tile Calorimeter:** The tile calorimeter is a sampling calorimeter using steel as the absorber and scintillating tiles as the active material, located outside the EM calorimeter envelope with a central barrel and two extended barrels, in the region of $|\eta| < 1.7$. It is segmented in depth in three layers, approximately 1.5, 4.1, and 1.8 interaction lengths (λ) thick for the central barrel and 1.5, 2.6, and 3.3 λ for the extended barrel. The total detector thickness at the outer edge of the tile-instrumented region is 9.7 λ at $\eta = 0$. Two sides of the scintillating tiles are read out by wavelength shifting fibers into two separate photomultiplier tubes.

- **LAr hadronic end-cap calorimeter:** The HEC consists of two independent wheels per end-cap, located directly behind the end-cap EM calorimeter and sharing the same LAr cryostats. To reduce the drop in material density at the transition between the end-cap and the forward calorimeter (around

$|\eta| = 3.1$), the HEC extends out to $|\eta| = 3.2$, thereby overlapping with the forward calorimeter. Each wheel is built from 32 identical wedge-shaped modules, divided into two segments in depth, for a total of four layers per end-cap. The wheels closest to the IP are built from 25 mm parallel copper plates, while those further away use 50 mm copper plates. The copper plates are interleaved with 8.5 mm LAr gaps, providing the active medium for this sampling calorimeter.

- **LAr forward calorimeter:** The FCal is integrated into the same cryostats as the end-cap calorimeter covering the range of $3.1 < |\eta| < 4.9$. It consists of three modules in each end-cap: the first, made of copper, is optimized for electromagnetic measurements, while the other two, made of tungsten, measure the energy of hadronic interactions. Each module consists of a metal matrix, with regularly spaced longitudinal channels filled with the electrode structure consisting of concentric rods and tubes parallel to the beam axis.

3.2.3 Muon Spectrometer

The Muon Spectrometer (MS) is the largest subsystem of the ATLAS detector, designed to measure the muon momentum based on the magnetic deflection of muon tracks in the large superconducting air-core toroid magnets, and cover the muon measurement up to $|\eta| = 2.7$. The machine is instrumented with separate trigger and high-precision tracking chambers. Over the range $|\eta| < 1.4$, magnetic bending is provided by the large barrel toroid. For $1.6 < |\eta| < 2.7$, muon tracks are bent by two smaller end-cap magnets. Over $1.4 < |\eta| < 1.6$, usually referred to as the transition region, deflection is provided by a combination of barrel and end-cap fields. This magnet configuration provides a field which is mostly orthogonal to the muon trajectories, while minimizing the degradation of resolution due to multiple scattering. In the barrel region, tracks are measured in chambers arranged in three cylindrical layers around the beam axis; in the transition and end-cap regions, the chambers are installed in planes perpendicular to the beam, also in three layers. The layout of MS is shown in Figure 3.7. There are four types of muon chamber installed in the MS.

- **Cathode Strip Chambers (CSC).** The CSCs are multi-wire proportional chambers segmented in ϕ on two wheels of eight chambers each. The (anode) wires are oriented in the radial direction and have (cathode) strips oriented perpendicular to them. A crossing muon will cause charges on several strips and interpolation between the charges can provide the position. Each crossing muon will leave four independent points in η and ϕ coordinate with a resolution

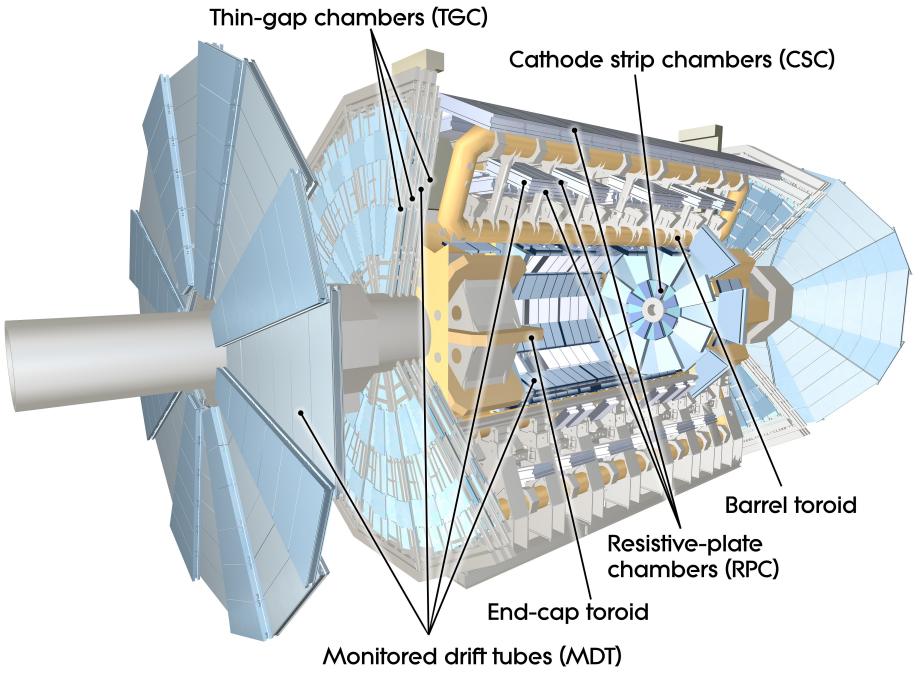

Figure 3.7: The cut-away view of the ATLAS Muon Spectrometer [52].

of 60 μm in η and 5 mm in ϕ. This design makes the chambers effective in high particle density environments. The sensitivity for neutrons is low, and the drift times are small, resulting in a time resolution of 7 ns. Furthermore, due to the ability to combine measurements in the η and ϕ coordinats it is possible to resolve ambiguities when more than one particle is present.

- **Monitored Drift Tubes (MDT).** MDT provides the precision measurement of the track coordinates in the principal bending direction of the magnetic field. In the barrel region ($|\eta| < 1.3$), the MDTs are positioned in three concentric layers around the beam axis, at an approximate radius of 5, 8 and 10 m. There is a 16-fold segmentation in ϕ, which are called *sectors*. To avoid holes in the acceptance, the chambers are partly overlapping. In the end-cap region ($1.0 < |\eta| < 2.7$), MDT chambers are assembled onto three wheels, inner, middle and outer layers positioned at $z = 7.5$, 14 and 22.5 m respectively. These chambers are trapezoidal shapes, small and large sectors also have overlaps to prevent any cracks in the detector coverage.

- **Resistive Plate Chambers (RPC).** RPCs constitute the muon trigger in the barrel ($|\eta| < 1.05$). Like the MDT chambers, the RPCs are positioned

in three concentric layers around the beam axis. The two inner chambers are assembled together with the middle MDT chambers, and the outer layer is assembled on the outer MDT chambers. Due to the large lever arm between inner and outer RPCs, the trigger is able to select high momentum muons with thresholds ranging from 9 to 35 GeV. The inner RPCs deliver the low momentum trigger with thresholds from 6 to 9 GeV. Each RPC has independent layers for η and ϕ measurements. Therefore, a muon trajectory usually provides six RPC measurements.

- **Thin Gap Chambers (TGC).** TGCs provide two functions in the end-cap MS ($1.05 < |\eta| < 2.7$, with trigger coverage $|\eta| < 2.7$): the muon trigger capability (with good time resolution and high rate) and the determination of the second, azimuthal coordinate to complement the measurement of the MDT's in the bending (radial) direction. TGCs are multi-wire proportional chambers. There are two types of TGC modules: a doublet module has two wire layers, a triplet module three and both structures have two strip layers. Position measurements are obtained from both the wires (η) and the strips (ϕ).

3.2.4 Trigger

The Trigger consists of three level of event selection: Level-1 (L1), Level-2 (L2), and event filter (EF). The L2 and event filter together form the High-Level Trigger (HLT). Each trigger level refines the decisions made at the previous level and applies additional selection criteria if necessary. The block diagram of the ATLAS trigger and data acquisition systems is shown in Figure 3.8.

The L1 trigger performs the initial event selection based on the information from the calorimeters and muon detectors. It reduces the event rate from 40 MHz to 75 kHz (Run I) or 100 kHz (Run II), a rate that most detectors can fit. The L1 Calorimeter Trigger (L1Calo) aims to identify high$-E_T$ objects such as electrons and photons, jets, and τ leptons decaying into hadrons, as well as events with large missing transverse momentum ($E_{\mathrm{T}}^{\mathrm{miss}}$) and large total transverse energy. For the electron/photon and τ triggers, isolation is also required. Isolation implies that the energetic particle must have a minimum angular separation from any significant energy deposit in the same trigger.

The L1 muon trigger is based on signals in the muon trigger chambers: RPC's in the barrel and TGC's in the end-caps. It searches for patterns of hits consistent with high$-p_T$ muons originating from the interaction region. The logic provides

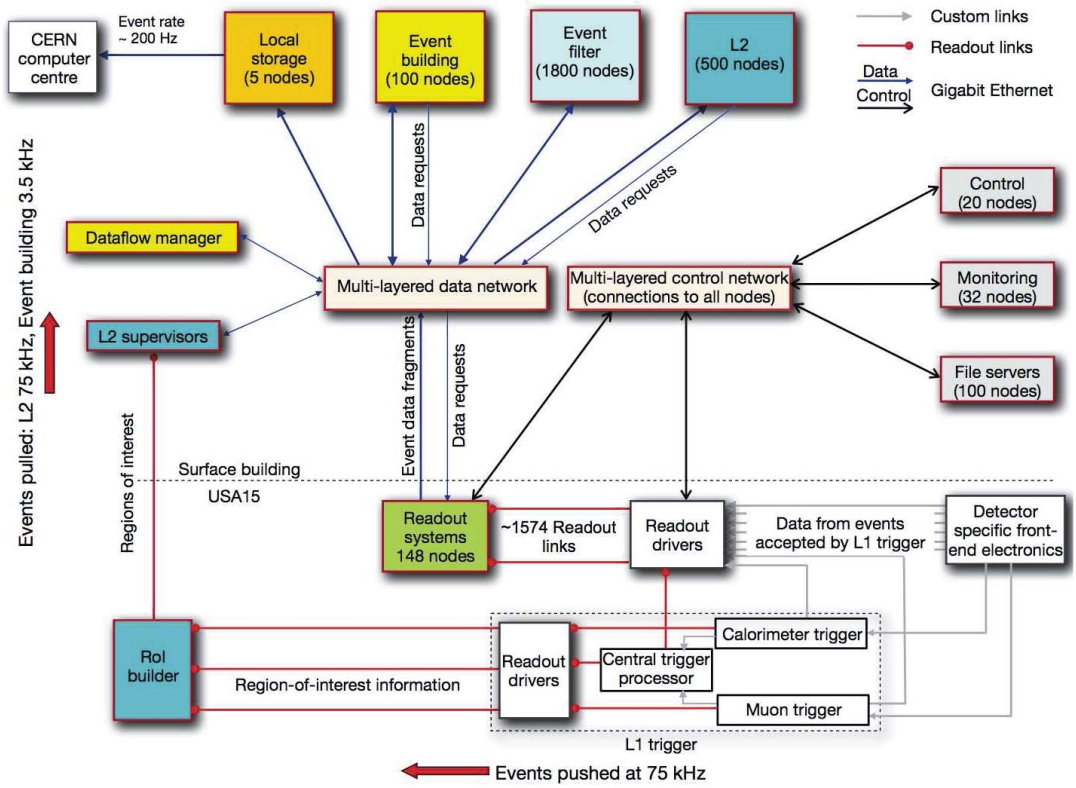

Figure 3.8: Block diagram of the ATLAS trigger and data acquisition systems. [63]

six independently-programmable p_T thresholds and the information for each bunch-crossing used in the L1 trigger decision is the multiplicity of muons for each of the p_T thresholds.

The overall L1 acceptance decision is made by the Central Trigger Processor (CTP), which combines all the energetic object information in the current event. When the L1 trigger decision is made based on the trigger objects, the information about the location of those objects is still retained in the muon and calorimeter trigger processors. Once the event being accepted by the L1 trigger, this information is sent as region of interest (RoI) to the L2 trigger, where it is used to seed the selection performed by the HLT.

The LV2 trigger reduces the event rate from 100 kHz to 3.5 kHz with an average event processing time of approximately 40 ms by running more complex object identification algorithms with commercial software. It uses all the information within RoIs specified by LV1, from the ID, the MS and full granular information of calorimeters, which accounts for about 2% of the total event.

The final selection step - the level 3 - is made by the event filter, which further reduces the event rate to 400 Hz for Run I and 1 kHz for Run 2 [62]. EF consists of many processing node, each handles tasks of receiving and processing events. Since the average time of processing an event is 4 s, unlike the L2 trigger, these tasks can be completed based on standard ATLAS event reconstruction and analysis applications. For those events passing the selection criteria, a subset of the data generated during the event analysis is sent to the event data structure, prepared for the subsequent offline analysis. Otherwise, the information will be removed from the readout devices.

3.2.5 Detector Simulation

The ATLAS detector simulation is performed by using the Geant4 simulation toolkit [78, 79]. The simulation software chain is generally divided into three steps, as shown in Figure 3.9: generation of the events and immediate decays, simulation of the detector and physics interactions, and digitization of the energy deposited in the sensitive regions of the detector into voltages and currents for comparison to the readout of the ATLAS detector. The output of the simulation chain can be presented in either an object-based format or in a format identical to the output of the ATLAS data acquisition system (DAQ), which can then be run through the ATLAS trigger and reconstruction packages in the same way as the real data.

The ATLAS detector geometry used for simulation, digitization, and reconstruction is built from databases containing the information describing the physical construction and conditions data. The latter contains all the information needed to emulate a single data-taking run of the real detector, such as the detector misalignment or temperatures. With the same geometry and simulation infrastructure, it is able to reproduce the installation configurations of the ATLAS detector.

The event generators are already discussed in Section 2.3.2. These events can be filtered during the generation process so that only events with a certain property (e.g. leptonic decay or within a specific kinematics phase space) are kept. The generated events are then read into the simulation. A record of all particles produced by the generator is retained in the simulation output file, but cuts can be applied to select only certain particles to process in the simulation. Each particle is propagated through the full ATLAS detector by Geant4. Geant4 provides models for physics and infrastructure for particle transportation through a geometry in the Geant4 format. In both event generation and detector simulation, information called "truth" is recorded for each event, which is a history of the interactions from the generator, including incoming and outgoing particles. A record is kept for every particle, whether the

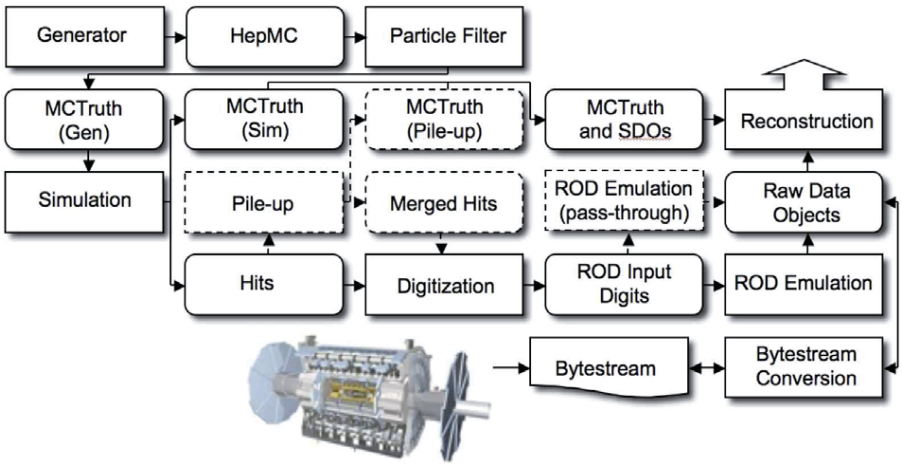

Figure 3.9: The flow of the ATLAS simulation software, from event generators (top left) through reconstruction (top right). [64]

particle is to be passed through the detector simulation or not.

CHAPTER IV

Object Reconstruction

Events recorded by the ATLAS detector or from MC simulation of pp collisions are reconstructed offline for physics analysis. Physics objects, such as electrons, muons, taus, photons, jets etc., are reconstructed by sub-detector components. Figure 4.1 shows a wedge of the transverse plane of the ATLAS detector, indicating different particles leave information in different sub-systems. All charged particles such as electron, muon will leave tracks in inner detector, protons and neutrons can deposit energies in calorimeters and muon will also leave tracks in MS. This chapter will introduce how the object are reconstructed.

4.1 Track

A track is a trajectory that a charged particle leaves when flying from IP outward to the ID. The ATLAS track system consists of two separate tracking sub-system: the Inner Detector and the Muon Spectrometer. The ID, closest to the IP, deals with highest density tracks, while the MS mainly focuses on reconstructing tracks from muon.

The ID track reconstruction software involves a modular and flexible software design to meet the requirements of both ID and MS reconstruction. These features form a common event data model, which allows for standardized interfaces to all reconstruction tools, such as track extrapolation, track fitting and vertex fitting. Track reconstruction in the ID is logically sub-divided into three stages:

1. A pre-processing stage, in which the raw data from the pixel and SCT detectors are converted into clusters, and the TRT raw timing information is translated into calibrated drift circles. The SCT clusters are transformed into space-points,

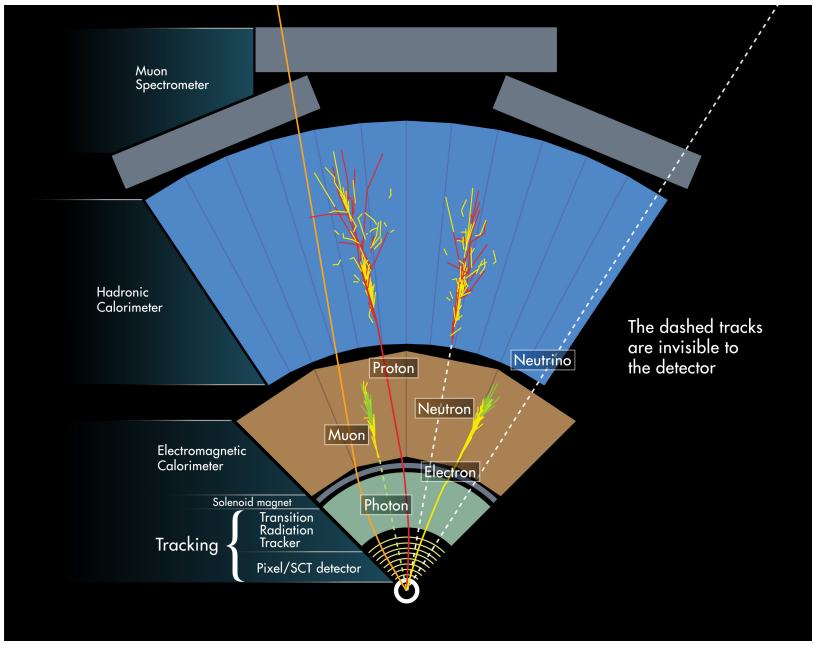

Figure 4.1: A wedge of the transverse plane of the ATLAS detector. Hadrons, leptons and photons have different signatures left in the detector. With algorithms dealing with such different characteristics, physics objects are reconstructed for following analysis [65].

using a combination of the cluster information from opposite sides of a SCT module.

2. A track-finding stage, in which different tracking strategies are implemented to cover different applications. The default tracking, called *inside-out* with minimum transverse momentum requirement $p_T > 400$ MeV, exploits the high granularity of the pixel and SCT detectors to find prompt tracks originating from the interaction region. First, track seeds are formed from a combination of space-points in the three pixel layers and the first SCT layer. These seeds are then extended throughout the SCT to form track candidates. Next, these candidates are fitted, "outlier" clusters are removed, ambiguities in the cluster-to-track association are resolved, and fake tracks are rejected. This is achieved by applying quality cuts. The selected tracks are then extended into the TRT to associate drift-circle information in a road around the extrapolation and to resolve the left-right ambiguities. Finally, the extended tracks are refitted with the full information of all three detectors (Pixel, SCT, and TRT). The quality of the refitted tracks is compared to the silicon-only track candidates and hits on track extensions resulting in bad fits are labeled as outliers.

A complementary track-finding strategy, called *outside-in*, searches for unused track segments in the TRT. Such segments are extended into the SCT and pixel detectors to improve the tracking efficiency for secondary tracks from conversions or decays of long-lived particles.

3. A post-processing stage, in which a dedicated vertex finder is used to reconstruct primary vertices.

The track reconstruction in the MS begins with searching for hits within each muon chamber and nearby trigger chambers. Segments are reconstructed by performing a straight-line fit to the hits in each MDT layer. The hits in RPC and TGC can provide the coordinate orthogonal to the bending plane. And in CSC planes, a combinatorial search for hits forms the segments with a loose compatibility requirement with the luminous region. Following the hits searching, muon track candidates are built by fitting the hits from segments in different layer together. The segments are selected with the criteria on hit multiplicity, fit quality and consistency among them. A track requires at least two matched segments, except that a single high-quality segment in the barrel-endcap transition region can also build a track. The same segment can be used to build several different track candidates. Later on, an overlap removal algorithm will select the best choice for a single track or allow a segment used in different tracks. The hits associated with each track candidate and the accepted track candidate are fitted using a χ^2 fit. The accepted one will be fitted again if the hits making large contribution are removed or additional hits are recovered.

4.2 Primary Vertex

A primary vertex (PV) is a spatial point where the pp collision happens and out-going particles originate. The reconstruction of primary vertices is organized in two steps: firstly, finding the primary vertex to associate reconstructed trucks to the vertex candidates and secondly, fitting the vertex to reconstruct the vertex position and its covariance matrix. The PV reconstruction algorithm works as the following steps:

- Pre-select reconstructed tracks satisfying track selection criteria and compatible with originating from the interaction point.
- Find the vertex seed position by clustering the tracks based on their z coordinates at their point of closest approach to the center of the beam spot.

- Fit and estimate the vertex position using the adaptive vertex fitting algorithm which takes seed and nearby tracks as input.
- Determine a new overtax using tracks incompatible with the vertex ($> 7\sigma$).
- Repeat the procedure until all tracks are associated to the event and no additional vertex can be found.

Given an input set of reconstructed tracks, the PV reconstruction efficiency is evaluated based on how often a vertex is reconstructed successfully and its position found consistent with the true value. Vertices are matched to interactions by calculating the sum of the weights of the tracks in a vertex matched to each interaction. If the sum of the weights of the tracks from the interaction is greater than 50%, the interaction is regarded as reconstructed. This requirement ensures that the vertex composition and hence the position is dominated by tracks of particles coming from the given interaction.

4.3 Electron

In the ATLAS detector, electrons are triggered and reconstructed from the energy deposits in the ECAL that are matched to a track in the inner detector. Electrons are distinguished from other particles using identification criteria with different levels of background rejection and signal efficiency. This section will introduce the electron construction, identification and isolation.

4.3.1 Electron Reconstruction

In the ECAL, the $\eta - \phi$ space is divided into a grid of $N_\eta \times N_\phi = 200 \times 256$ towers of size $\Delta\eta^{tower} \times \Delta\phi^{tower} = 0.025 \times 0.025$, corresponding to the granularity of the ECAL middle layer. The electron reconstruction in the central region ($|\eta| < 2.47$) contains 3 main steps:

1. Seed-cluster reconstruction:

   To reconstruct the EM cluster, seed clusters of towers with total cluster transverse of energy above 2.5 GeV are searched by a sliding-window algorithm with size of 3×5 towers in $\eta - \phi$ space. A duplicate-removal algorithm is applied to nearby seed clusters. For each seed EM cluster passing loose shower shape requirement, a ROI with a cone-size of $\Delta R = 0.3$ around the seed cluster

barycenter is defined. The collection of these EM cluster ROIs is retained for use in the track reconstruction.

2. Track candidate reconstruction:
   Electron track reconstruction contains two steps, pattern recognition and track fit. The standard pattern recognition uses the *pion hypothesis* for energy loss in the material. If a track seed with $p_T > 1$ GeV fails extended to a full track and falls within one EM cluster ROI, it is retried with a new pattern recognition using the *electron hypothesis*, which allows up to 30% energy loss accounting for bremsstrahlung. In this way, pattern recognition performance is improved while the interference with the main track reconstruction is minimized. The parameters of the track candidates found by pattern recognition are then fitted with the same hypothesis used in pattern recognition, using the *ATLAS Global* χ^2 *Track Fitter*. If a track candidate fails the *pion hypothesis* track fit, it is refitted with the *electron hypothesis*.

3. Electron candidate reconstruction:
   An electron is reconstructed if at least one track is matched to the seed cluster. If multiple tracks are assigned to a cluster, the best-matched one is chosen as the primary track with following criteria: the track with at least 1 Pixel hit; or the track with the smallest ΔR if more than one track has at least 1 Pixel hit. All seed clusters together with their matching tracks are treated as electron candidates. Each of these electron clusters is then rebuilt in all four layers sequentially, starting from the middle layer, using $3\times7(5\times5)$ cells in $\eta\times\phi$ space in the barrel (end-caps) region. The cluster position is adjusted in each layer to take into account the distribution of the deposited energy. Then, the energy calibration is applied as the next step [66].The four-momentum of the electron candidate is computed using both the final cluster and its primary track. The energy is given by cluster energy and (η, ϕ) is extracted from corresponding track parameters, except for TRT-only tracks, cluster η and ϕ are used.

In the forward region ($2.5 < |\eta| < 4.9$), where ID loses its coverage, the electron reconstruction uses only the information from the EMEC and forward calorimeters and therefore no distinction is possible between electrons and photons. Due to the reduced detector information in this region, the use of forward electrons in physics analyses is restricted to the range $E_T > 20$ GeV. In contrast to the fixed size sliding-window clustering used in the central region, the forward region uses a topological

clustering algorithm [66]. The direction of the forward-electron candidates is defined by the barycenter of the cells belonging to the cluster.

4.3.2 Electron Identification

The identification criteria for central electron candidates are implemented based on sequential cuts on calorimeter, on tracking, and on combined track-cluster variables.

Signal electrons are identified by different sets of likelihood-based identification criteria which are chosen to be 95%, 90% and 80% efficient for electrons with $E_T \approx$ 40 GeV, and referred to as *loose*, *medium* and *tight* operating points respectively. Figure 4.2 shows the electron ID efficiencies in $Z \rightarrow ee$ and $J/\Psi \rightarrow ee$ (in low transverse energy E_T region) events as a function of transverse energy (E_T).

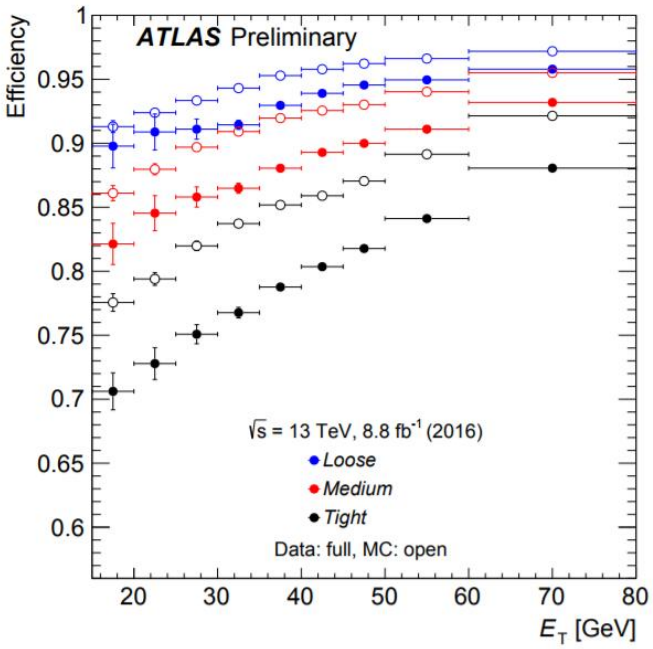

Figure 4.2: The electron identification efficiency for *loose*, *medium*, and *tight* categories as a function of transverse energy E_T [67].

The increased background-rejection power is obtained both by adding discriminating variables at each step and by tightening the requirements on the original variables. Detailed selections can be found in [67]. The identification of the forward electron is also based on sequential cuts on discriminating variables; however, these variables are mostly based on topological cluster moments. Three reference sets of selection criteria, same as the central region, are defined. To compensate for the absence of tracking information in the forward region, variables describing both the lateral and

longitudinal shower development are employed. In addition, due to the significantly harsher pile-up conditions in the forward region, the identification criteria for forward electrons were optimized directly with data in nine cluster-η bins and four number of PV bins.

The identification efficiency of electron as *loose*, *medium*, or *tight* is calculated w.r.t a reconstructed electron candidate, labeled as ϵ_{loose}, ϵ_{medium}, and ϵ_{tight}. The efficiency ranges from 60% to 90% according different types of electron in different η regions.

4.3.3 Electron Isolation

Electron isolation is used to reject the backgrounds such as photon conversion, mis-identified jets and so on. Most analyses require electrons to pass some isolation criteria in addition to the identification requirements. Two isolation variables are defines:

- Calorimeter-based isolation:
  The calorimetric isolation variable $E_T^{cone\Delta R}$ is defined as the sum of transverse energy E_T deposited in the calorimeter cells in a cone size of ΔR around the electron, excluding the contribution of electron itself, which is the energy deposited within $\Delta\eta \times \Delta\phi = 0.125 \times 0.175$ around the particle.

- Track-based isolation:
  The track isolation variable $p_T^{cone\Delta R}$ is the scalar sum of the transverse momentum of the tracks with $p_T > 0.4$ GeV in a cone of ΔR around the electron, excluding the track of electron itself. The tracks in the sum must share the same primary vertex associated with the electron track and pass the good quality requirement: at least nine silicon hits, one of which must be in the innermost pixel layer. This variable is quite robust to pile-up.

In addition to isolation cuts, final requirement on transverse and longitudinal impact parameters, which are denoted as d_0 and z_0 respectively, are also applied to ensure the electron candidates come from PVs. $\sigma(d_0)$ and $\sigma(z_0)$ denote the corresponding uncertainties estimated by the track fit. Generally, d_0 and z_0 are small if the track come from the center of the beam spot, indicating they are tracks from PV.

4.4 Muon

Muons are a crucial ingredient for some of the most important physics results published by the ATLAS at the LHC. These include the discovery of the Higgs boson and the measurements of its properties, precise measurements of the SM processes, and searches for the BSM physics. How to efficiently and accurately identify muons and measure their four momenta is a major task of the ATLAS detector. This chapter will introduce how to reconstruct and identify muons.

4.4.1 Muon Reconstruction

Muon reconstruction is performed independently in the ID and MS. The information from individual subdetectors is then combined to form the muon tracks prepared for physics analyses. In the ID, muons are reconstructed like any other charged particles described in [68]. In the MS, muons are reconstructed following the steps described in section 4.1.

The combined ID-MS muon reconstruction is performed using different algorithms according to the information provided by the ID, MS and calorimeters. There are four types of muon depending on which reconstruction method and subdectors are used.

- Combined (CB) muon: track reconstruction is performed independently in the ID and MS, and a combined track is formed with a global refit that uses the hits from both the ID and MS subdetectors. To improve the fit quality, MS hits may be added to or removed from the track. Most muons are reconstructed following an outside-in pattern recognition: muons are first reconstructed in the MS and then extrapolated inward to match to an ID track. Another reconstruction method called inside-out, in which ID tracks are extrapolated outward and matched to MS tracks, is used as a complementary approach. CB muon is the main type of four and has the highest muon purity, but with coverage limited to $|\eta| < 2.5$.

- Segment-tagged (ST) muon: a track in the ID is classified as ST muon if it's extrapolated to the MS and matches to at least one local track which is not yet associated with any CB track. ST muon are used to increase acceptance when the muons cross only one layer of the MS, either due to their low p_T or because they fall in regions with reduced MS acceptance.

- Calorimeter-tagged (CT) muon: a track in the ID is identified as a muon if it matches to a minimum-ionizing particle (energy deposit in the caolrimeter meeting certain criteria). Two calorimeter-seed algorithms are used to search for muons: the $LArMuID$ finds muon from ECAL and the $TIleMuID$ trigger the HCAL information for muon. Then, a track-seed algorithm, $CaloMuonTag$, extrapolates ID tracks through the calorimeters to match and identify those energy deposits and thus form the pattern of a muon. This type has the lowest purity of all the muon types but it recovers acceptance in the region where the MS in only partially instrumented to allow for cabling and services to the calorimeters and inner detector.

- Extrapolated (ME) muon: a muon trajectory is reconstructed based on the MS track and a loose requirement on compatibility with originating from the IP. The muon is required to pass through at least two layers of MS chambers to provide a track measurement, three layers in the forward region. This type of muon is used to extend the acceptance of muon reconstruction into the region $2.5 < |\eta| < 2.7$, which is not covered by the ID ($|\eta| < 2.5$).

For the overlap among four muon types, there are certain preferences applied. When two muon types share the same ID track, preference is given to CB muons, then to ST and finally to the CT muons. To resolve the overlap with ME muons in the system, one can analyze the track hit content and select the track with better fit quality and larger number of hits.

The muon reconstruction in LHC Run II uses algorithms named $Chain3$ in [69]. These algorithms implement the performance in several aspects: 1) Using Hough transform to identify the hit patterns to make the reconstruction faster and more robust against misidentification of hadrons. 2) Improvement in the early stage of pattern recognition process to reduce the background contamination. 3) Involving the analytic parameterization to improve the precision of the energy loss calculation in the calorimeter (a precision on the mean energy loss of about 30 MeV for 50 GeV muons).

4.4.2 Muon Identification

Muon identification is performed by applying quality requirements that suppress background, while keeping high efficiency and robust momentum measurement. Several variables provide good discrimination between prompt muons (signal) and backgrounds (diboson, $t\bar{t}$, etc.):

- q/p significance, defined as:

$$\sigma_{q/p} = \frac{|q/p_{\mathrm{T,ID}} - q/p_{\mathrm{T,MS}}|}{\sqrt{\sigma^2_{p_{\mathrm{T,ID}}} + \sigma^2_{p_{\mathrm{T,MS}}}}}, \tag{4.1}$$

  the absolute value of the difference between the ratio of the charge q and transverse momentum of the muons p_T measured in the ID and MS divided by the corresponding uncertainties sum in quadrature;

- $\rho^{'}$, defined as:

$$\rho^{'} = \frac{p_{\mathrm{T,ID}} - p_{\mathrm{T,MS}}}{p_{\mathrm{T,CB}}} \tag{4.2}$$

  the absolute value of the difference between the transverse momentum measurements in the ID and MS divided by the p T of the combined track;

- normalized χ^2 of the combined track fit.

To guarantee a robust momentum measurement, some requirements on the number of hits in the ID and MS are applied. For the hits in ID, the cuts require at least one Pixel hit and five SCT hits, less than three Pixel or SCT holes. At least 10% of TRT hits assigned to the track should be included in the final fit. There are four sets of identification selection ($Medium$, $Loose$, $Tight$, $High - p_T$) used to address the specific needs of different physics analyses.

- $Medium$ muon: the medium identification criteria, designed to minimize the systematic uncertainties associated with muon reconstruction and calibration, is used as default selection for muons in the ATLAS. Only CB and ME tracks are used, with additional requirement on the number of hits in muon chambers and a loose selection on the compatibility between p_T measurements in the ID and MS. Specifically, CB tracks require at least three hits in at least two MDT layers, ME tracks require at least three MDT/CSC layers within the coverage $2.5 < |\eta| < 2.7$. The requirement q/p significance < 7 is also applied.

- $Loose$ muon: the loose identification criteria are designed to maximize the reconstruction efficiency while providing good-quality muon tracks. All four muon types are used. CB and ME muons satisfying the $Medium$ requirements are included in the $Loose$ selection, CT and ST muons within $|\eta| < 0.1$ region are also included. In the region $|\eta| < 2.5$, about 97.5% of the $Loose$ muons are combined muons, 1.5% are CT muons and the remaining 1% are ST muons.

- *Tight* muon: tight muons are selected to maximize the purity of muons at the cost of some efficiency. Only CB muons with hits in at least two stations of the MS and satisfying the *Medium* selection criteria are considered. In addition, the normalized χ^2 of the combined track fit is required to be less than eight. A two-dimensional cut on the $\rho^{'}$ and q/p significance is applied as a function of muon p_T to further reject background.

- *High-p_T* muon: The *High-p_T* selection aims to maximize the momentum resolution for tracks with transverse momentum above 100 GeV. CB muons passing the Medium selection and having at least three hits in three MS stations are considered. Specific regions of the MS where the alignment is optimal are vetoed as a precaution.

Figure 4.3 shows the muon reconstruction efficiency as a function of η as measured from the $Z \rightarrow \mu\mu$ events for different muon selections. The overall efficiency for *medium* muon, which is used in these analyses, is over 98%.

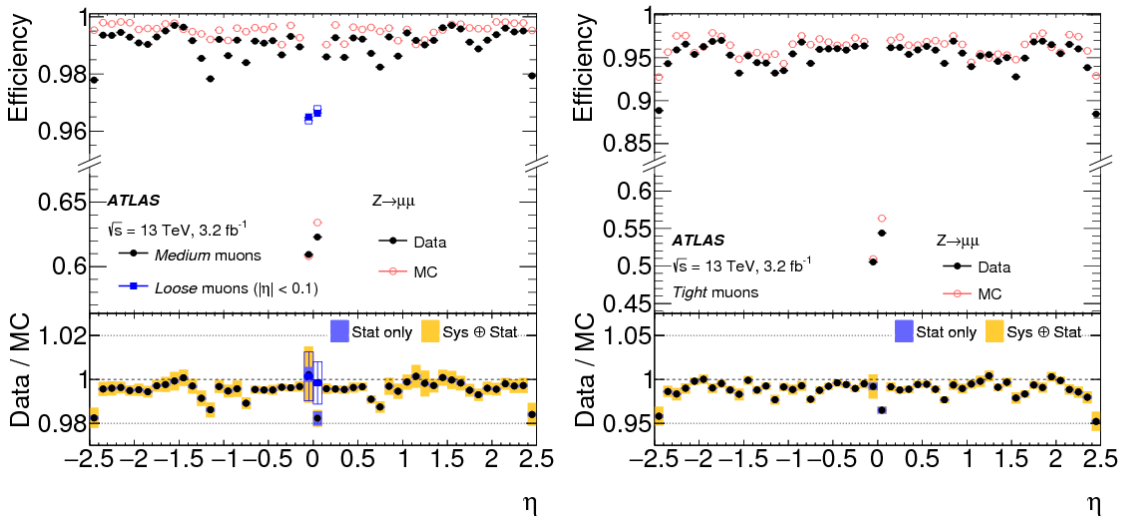

(a) (b)

Figure 4.3: Muon reconstruction efficiency as a function of η measured in $Z \rightarrow \mu\mu$ events for muons with $p_T > 10$ GeV shown for *Medium* (left), *Tight* (right) muon selections. In addition, the left plot also shows the efficiency of the *Loose* selection in the region $|\eta|$ <0.1 where the *Loose* and *Medium* selections differ significantly. The error bars on the efficiencies indicate the statistical uncertainty. Panels at the bottom show the ratio of the measured to predicted efficiencies, with statistical and systematic uncertainties [68].

4.4.3 Muon Isolation

Muons originating from the decay of heavy particles, such as W, Z, or Higgs bosons, are often produced isolated from other particles. The measurement of detector activity around a muon candidate, referred to as *muon isolation*, is a powerful tool to reject background in physics analyses. Two variables are defined to access muon isolation: a track-based isolation variable and a calorimeter-based isolation variable. The track-based isolation variable ($p_T^{varcone30}$) is defined as the scalar sum of the transverse momentum of the tracks with $p_T > 1$ GeV in a cone of size $\Delta R = \min(10 \text{ GeV}/p_T^{\mu}, 0.3)$ around the muon p_T, excluding the muon track itself. The calorimeter-based isolation variable ($E_T^{varcone20}$) is defined as the sum of the transverse energy of topological clusters in a cone of size $\Delta R = 0.2$ around the muon, subtracting the energy deposit contributed by muon itself. Contributions from pile-up and the underlying event are estimated using the ambient energy-density technique and are corrected on an event-by-event basis. Muon isolation selection criteria are defined using relative isolation variables, $p_T^{varcone30}/p_T$ and $E_T^{varcone20}/E_T$, defined as the ratio of the track- or calorimeter-based isolation variables to the transverse momentum or energy of the muon.

4.5 Jet

Jets, collimated sprays of hadrons, are the dominant physics objects in pp collision and play a key role in various physics analyses. In ATLAS, jets are observed as groups of topologically related energy deposits in the calorimeters, associated with tracks of charged particles measured in the inner tacking detector. This section will introduce the jet reconstruction and calibration.

4.5.1 Jet reconstruction and calibration

The main jet identification algorithm used by the ATLAS collaboration is the anti-k_t algorithm with a distance parameter $R = 0.4$. Jets reconstructed from tracks, also referred to as the track jets, have low dependence on the pile-up activity but limited to the coverage $|\eta| < 2.5$. Jets reconstructed using the energy deposits in the calorimeter are referred to as calorimeter jets. The inputs for calorimeter jets reconstruction are the topologically clustered calorimeter cells, so-called topo-clusters [70].

The topo-clusters are initially reconstructed at the electromagnetic (EM) scale which correctly measures the energy deposited in the calorimeter by particles pro-

duced in EM showers. A second topo-cluster collection is built by calibrating the calorimeter cell such that the response of the calorimeter to hadrons is correctly reconstructed. This calibration uses the local cell weighting (LCW) method that aims at an improved resolution compared to the EM scale by correcting the signals from hadronic deposits, and thus reduces fluctuations due to the non-compensating nature of the ATLAS calorimeter. The LCW method first classifies topo-clusters as either electromagnetic or hadronic, primarily based on the measured energy density and the longitudinal shower depth. Then energy corrections are derived according to this classification from single charged and neutral pion MC simulations. Dedicated corrections address effects of calorimeter non-compensation, signal losses due to noise threshold effects, and energy lost in non-instrumented regions close to the cluster.

The ATLAS jet energy calibration can be summarized in the following five steps:

1. Origin Correction: The origin correction forces the four-momentum of the jet to point to the hard-scatter primary vertex rather than to the center of the detector while keeping the jet energy constant.

2. Pile-up Correction: Jets formed from topo-clusters at the EM or LCW scale are first calibrated by applying a correction to account for the energy offset caused by pile-up interactions. This correction is derived from MC simulations as a function of the number of reconstructed primary vertices (N_{PV} , measuring the actual collisions in a given event) and the expected average number of interactions (μ) in bins of jet η and p_T.

3. Monte Carlo numerical inversion: The calibration of the energy and pseudorapidity of a reconstructed jet is a simple correction derived from the relation of these quantities to the corresponding ones of the matching truth jet in MC simulations. The numerical inversion calibration restores the average reconstructed jet energy to the mean value of the truth jet energy. It can be applied to jets formed from topo-clusters at EM or at LCW scale with the resulting jets being referred to as calibrated with the EM+JES or with the LCW+JES scheme.

4. Global sequential correction: A global sequential correction uses additional observables to adapt the jet energy calibration to account for the variation caused by numerical inversion, thereby improving the jet resolution without changing the scale. Three variables are used as inputs for this correction: 1) the fraction of the jet energy measured from constituent tracks; 2) the fraction of jet energy

measured in the third EM calorimeter layer and 3) he fraction of jet energy measured in the first Tile calorimeter layer.

5. Residual *in situ* Calibration: The *in situ* calibration is derived as the last step to correct the jets reconstructed in data. The correction calculates the jet response difference between data and MC simulation using transverse momentum balance between the jet and a well-measured reference object to assess the data-to-MC differences.

4.5.2 B-jet tagging

A B-jet candidate may be reconstructed by using the a new algorithm has been developed, referred to as MV2c20 [71]. The algorithm is based on a boosted decision tree approach, which utilizes jet properties and variables based on the reconstructed charged particle tracks as input. The algorithm is trained on b-jets as signal and a mix of c- and light jets, in the proportion of 80% and 20%, as background. The training is performed using simulated $t\bar{t}$ events. The MV2c20 inputs are based on algorithms that exploit the relatively long b-hadron lifetime: a likelihood-based combination of the transverse and longitudinal impact parameter significance (IP3D), the presence of a secondary vertex and related properties (SV), and the reconstruction of the b-hadron decay chain using a Kalman filter to search for a common direction connecting the primary vertex to both the beauty and the tertiary charm decay vertices, referred to as JetFitter (JF) [72].

4.6 Missing Transverse Momentum

The missing transverse momentum $E_{\mathrm{T}}^{\mathrm{miss}}$ is defined as the momentum imbalance in the plane transverse to the beam axis, where the the vector transverse momenta of the collision products should sum to zero. Such imbalance indicates the presence of undetectable particles, such as neutrinos, new weakly-interacting particles escaping the detector. The scheme of $E_{\mathrm{T}}^{\mathrm{miss}}$ production is shown in Figure 4.4. The vector momentum imbalance in the transverse plane is the negative vector sum of the momenta of all particles detected in a pp collision events.

4.6.1 $E_{\mathbf{T}}^{\mathbf{miss}}$ reconstruction and calibration

Three types of $E_{\mathrm{T}}^{\mathrm{miss}}$ reconstruction are defined according to the information they used. Calorimeter-based soft term (CST) $E_{\mathrm{T}}^{\mathrm{miss}}$ uses the energy deposits in the

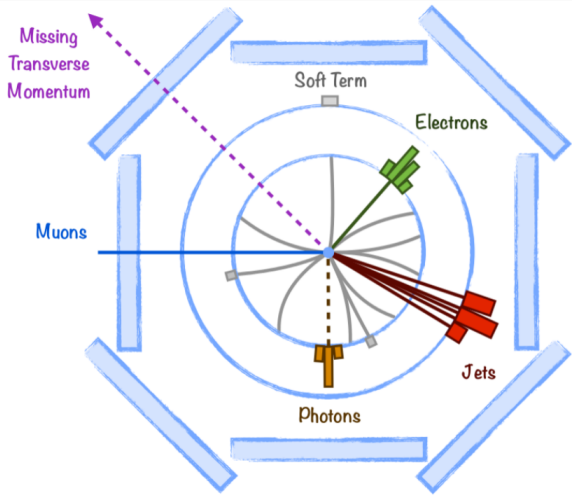

Figure 4.4: The scheme of $E_{\mathrm{T}}^{\mathrm{miss}}$ generation according to detectable particles.

calorimeters for all objects. Track-based soft term (TST) $E_{\mathrm{T}}^{\mathrm{miss}}$ uses energy deposits in the calorimeters for hard objects (e, γ, μ etc..) and track information from soft term (soft radiation, underlying event activity). Track $E_{\mathrm{T}}^{\mathrm{miss}}$ uses the information purely based on momenta of ID tracks.

The CST $E_{\mathrm{T}}^{\mathrm{miss}}$ is sensitive to pile-up interactions due to an additional contribution from calorimeter-based soft term. The track $E_{\mathrm{T}}^{\mathrm{miss}}$ is robust to pile-up, but insensitive to neutral particles since they do not leave any tracks in ID and limited to the acceptance due to tracking volume of the ATLAS detector. Therefore, TST $E_{\mathrm{T}}^{\mathrm{miss}}$, a good compromise between CST $E_{\mathrm{T}}^{\mathrm{miss}}$ and track $E_{\mathrm{T}}^{\mathrm{miss}}$ is the primary method of $E_{\mathrm{T}}^{\mathrm{miss}}$ reconstruction in ATLAS Run II.

A direct measurement of the performance of $E_{\mathrm{T}}^{\mathrm{miss}}$is performed under different pile-up conditions. The resolution in $E_{\mathrm{x}}^{\mathrm{miss}}$ and $E_{\mathrm{y}}^{\mathrm{miss}}$ is shown as a function of the number of primary vertices in the event, N_{PV} in Figure 4.5.

The $E_{\mathrm{T}}^{\mathrm{miss}}$ calculation process uses reconstructed and calibrated physics objects to estimate the transverse momentum imbalance in an event. As described above, calorimeter energy deposits are associated with reconstructed and identified hard objects in the following order: electrons (e), photons (γ), hadronically decaying tau-leptons (τ), jets and finally muons (μ). The soft term part whose energy deposits not associated with any hard objects is also considered in the $E_{\mathrm{T}}^{\mathrm{miss}}$ calculation based on ID tracks. The $E_{\mathrm{T}}^{\mathrm{miss}}$ is calculated as follows:

$$E_{x(y)}^{\mathrm{miss}} = E_{x(y)}^{\mathrm{miss},e} + E_{x(y)}^{\mathrm{miss},\gamma} + E_{x(y)}^{\mathrm{miss},\tau} + E_{x(y)}^{\mathrm{miss,jets}} + E_{x(y)}^{\mathrm{miss},\mu} + E_{x(y)}^{\mathrm{miss,SoftTerm}}, \tag{4.3}$$

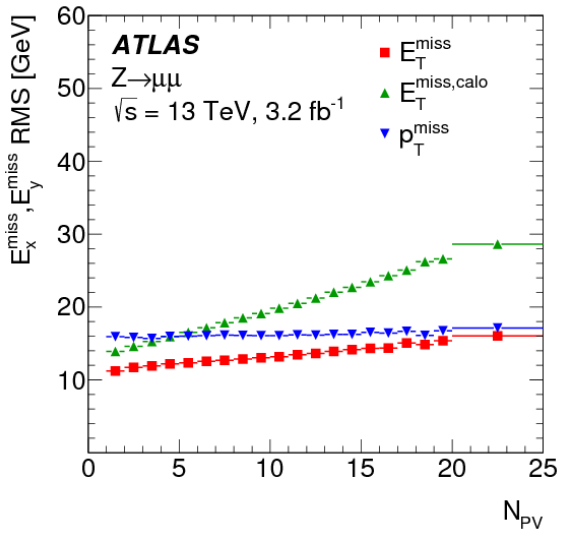

Figure 4.5: Comparison of the performance of $E_{\mathrm{T}}^{\mathrm{miss}}$ built from TST and CST, and the Track $E_{\mathrm{T}}^{\mathrm{miss}}$, under different pile-up conditions. The resolution (RMS of $E_{\mathrm{x}}^{\mathrm{miss}}$, $E_{\mathrm{y}}^{\mathrm{miss}}$) is shown shown as a function of N_{PV}. [75]

where each term is calculated as the negative sum of the calibrated reconstructed objects, project onto the transverse plane (x-y plane). The electrons are reconstructed and calibrated with the standard ATLAS calibration as described in Section 4.3. Photon identification exploits the different evolution of the electromagnetic showers resulting from photons and from jets. The *Tight* working point is used to efficiently reject fake photons from neutral meson decays as well as requirement on calibrated p_T greater than 25 GeV and $|\eta| < 2.37$. The τ-lepton are calibrated with the LCW, and the tau energy scale (TES) correction is applied [73]. In addition, hadronically decaying tau-leptons are required to have $p_T > 20$ GeV and $|\eta| < 2.5$. The jets are reconstructed with the anti-k_t algorithm with distance parameter $R = 0.4$, as described in Section 4.5. The track soft term is built on tracks coming from the hard scatter vertex and not associated to high-p_T objects. Tracks are excluded if they are within $\Delta R = 0.05$ of an electron or photon cluster, or within $\Delta R = 0.2$ of a hadronically-decaying tau-lepton and are removed if associated with jets using the ghost-association technique [74].

CHAPTER V

Search For Dark Matter Particles

This chapter presents the search for dark matter particles from an invisibly decaying Higgs boson produced in association with a leptonically decaying Z boson ($Z \to ll$) in proton-proton collisions at $\sqrt{s} = 13$ TeV. This search uses 36.1 fb^{-1} of data collected by the ATLAS experiment at the LHC.

5.1 Introduction

The Feynman diagrams for $qq \to ZH$ and $gg \to ZH$ productions are shown in Figure 5.1. In this analysis, we search for a beyond the SM (BSM) Higgs boson (h) invisible decay and assume h is produced with the SM Higgs boson (H) cross-section.

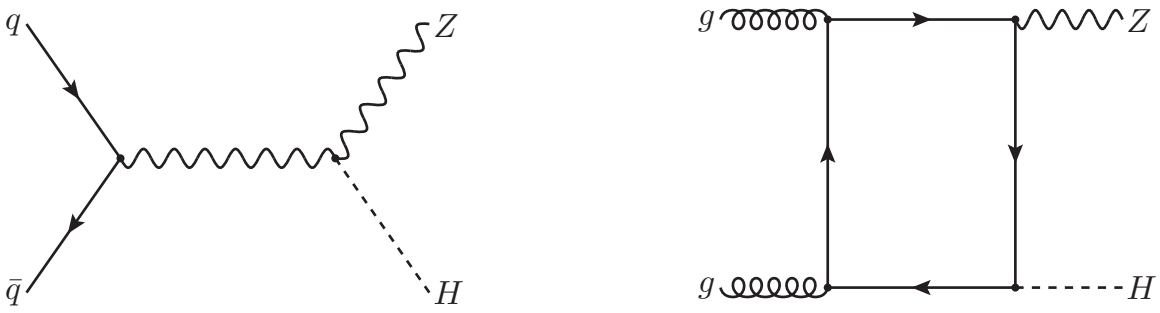

(a) (b)

Figure 5.1: Feynman diagrams for leading order ZH production through (a) qq annihilation and (b) gg fusion. In this analysis, we search for an invisible Higgs (h) decay by assuaming this Higgs boson (h) is produced with the SM Higgs Boson (H) cross section.

In experiment, the dark matter signature is large missing transverse energy ($E_{\mathrm{T}}^{\mathrm{miss}}$). The major background is SM ZZ production with one Z boson decaying to di-lepton ($\ell^+\ell^-$, ℓ = e, or μ) and another Z boson decaying to neutrino pair ($v\bar{v}$, v= e, μ, τ). ZZ is a typical irreducible background since it has exactly the same final state as the signal. The second major background is SM WZ production with Z decaying to di-lepton and W decaying to lv if the lepton decay from W is mis-classified or not recorded by the detector. Some other backgrounds also contaminate the signal. For example WW decaying to $lvlv$, Z+jets with Z decaying to di-lepton and jets faking the $E_{\mathrm{T}}^{\mathrm{miss}}$, and top processes($t\bar{t}$, tW...) and so on.

The physics analysis can be divided into following steps: 1) Object reconstruction, to reconstruct the objects (electron, muon, jets, $E_{\mathrm{T}}^{\mathrm{miss}}$...) used in this analysis; 2) Optimization, which is also known as event selection to detect the signal; 3) Background estimation, to estimate the contribution of each background; 4) Systematic uncertainties, to estimate the systematic uncertainties for both signal and backgrounds; 5) A statistical analysis to interpret the physics results.

5.2 Data and MC Samples

5.2.1 Data Sample

The proton-proton collision data used in this search were collected by the ATLAS detector at a center-of-mass energy of 13 TeV with a 25 ns bunch-spacing configuration during 2015 and 2016. Single-lepton triggers are used for data collection, a combination of a lower p_T threshold trigger with an isolation requirement and a higher p_T threshold trigger without any isolation requirement is used. The p_T threshold of the isolated electron (muon) trigger ranges from 24 (20) to 26 GeV depending on the instantaneous luminosity. The higher p_T threshold is 50 (60) for the electron (muon) case over all the data-taking periods. If any relevant detector component is not operating correctly during a period in which an event is recorded, the event is rejected. With all these quality requirements, the total accumulated data sample corresponds to an integrated luminosity of 36.1 fb^{-1} with 3.2% systematic uncertainty.

5.2.2 Monte Carlo Samples

5.2.2.1 $Zh \to \ell\ell +$ invisible signal samples

$Zh \to \ell\ell$ + invisible samples are generated by POWHEG [44] and interfaced to PYTHIA8 [77] for parton showering. Both $gg \to Zh$ and $qq \to Zh$ processes are

Process	Generator	m_h (GeV)	σ (fb)
$qq \to Zh \to \ell\ell + inv.$	POWHEG + PYTHIA8	125	76.89
$gg \to Zh \to \ell\ell + inv.$	POWHEG + PYTHIA8	125	12.42

Table 5.1: Cross section for the $Zh \to \ell\ell$ + invisible signal with $m_h = 125$ GeV, where $\ell = e, \mu, \tau$.

simulated. The Higgs boson is forced to decay to 4ν to give the invisible signature in these samples. Then, the ATLAS detector simulation is performed for each event with GEANT4 [78] framework. The invisible Higgs boson decay branching fraction is assumed to be 100% when making the distributions and estimating signal yields. The CT10nlo parton distribution function (PDF) set and AZNLO tune are used for generating these samples.

The Zh production cross sections are assumed to be the same as the SM cross section ZH, provided by the LHC XS Working Group based on the CERN Yellow Report 3 [82]. The cross sections are calculated at NNLO QCD and NLO EW accuracies. The cross sections for the $Zh \to \ell\ell +$ invisible with $m_h = 125$ GeV can be found in Table 5.1. The $gg \to Zh$ process accounts for 14% of the total Zh production. EW corrections are applied for the $qq \to Zh$ process with the $m_h = 125$ GeV, as a function of $p_T(Z)$.

5.2.2.2 Background samples

Monte Carlo samples have been used to simulate background processes as well as signal processes. All the samples have been generated for a center-of-mass energy of 13 TeV and passed through the full simulation of the ATLAS detector. Several processes can produce the same experimental signature of di-lepton plus $E_{\mathrm{T}}^{\mathrm{miss}}$ as the signal. Background topologies can be classified in these categories:

- 2 real leptons + $E_{\mathrm{T}}^{\mathrm{miss}}$ (real or fake)
- 1 real + 1 fake lepton + $E_{\mathrm{T}}^{\mathrm{miss}}$ (real or fake)

In all these cases the real $E_{\mathrm{T}}^{\mathrm{miss}}$ comes from neutrinos, while the fake $E_{\mathrm{T}}^{\mathrm{miss}}$ is mainly due to pile-up interactions, mis-calibrations and jet energy resolution.

Monte Carlo samples are used to simulate all the background processes considered. These have been centrally produced by the ATLAS Physics Modeling Group (PMG), who also provides the cross section values and the filter efficiencies (fraction of events

that pass from the general sample into the final simulated sample). If higher order cross section computation is available, it is taken into account, together with the above information, to normalize the sample to the data integrated luminosity. Different Monte Carlo generators interfaced to different parton showering programs were used, which are described in the followings.

5.2.2.3 ZZ production

Pair production of Z bosons, referred to as the ZZ process, is the main background in this analysis, which is irreducible. Samples of ZZ production for the processes $ZZ \to \ell^+\ell^-\nu\bar{\nu}$, $ZZ \to \ell^+\ell^-\ell'^+\ell'^-$, $ZZ \to \nu\bar{\nu}\nu\bar{\nu}(l = e, \mu, \tau)$ are simulated using the POWHEG event generator with AZNLO CTEQ6L1 tune, interfaced with PYTHIA8 for the parton showering. A minimum mass of 4 GeV is required for each charged lepton.

Details about these samples are given in Table 5.2.

Process	Generator	σ (pb)	k-factor	Filter efficiency
$qq \to ZZ \to \ell^+\ell^-\ell'^+\ell'^-$	POWHEG+Pythia8	1.2673	1.0	1.0
$qq \to ZZ \to \nu\bar{\nu}\nu\bar{\nu}$	POWHEG+Pythia8	0.54901	1.0	1.0
$qq \to ZZ \to \ell^+\ell^-\nu\bar{\nu}$	POWHEG+Pythia8	0.91795	1.0	1.0
$gg \to ZZ \to \ell^+\ell^-\nu\bar{\nu}$	POWHEGgg2vv+Pythia8	0.05187	1.0	0.66248
$qq \to ZZ \to \ell^+\ell^-\nu\bar{\nu}$	POWHEG+Pythia8 (m_T filtered)	0.92118	1.0	0.016068
$qq \to ZZ \to \ell^+\ell^-\nu\bar{\nu}$	SHERPA	12.465	1.0	1.0

Table 5.2: Cross sections at the NLO in perturbation theory, k-factors and filter efficiencies for ZZ POWHEG+Pythia8 samples at $\sqrt{s} = 13$ TeV. Processes listed refer to both quark-quark and gluon-gluon production modes.

5.2.2.4 WZ and WW production

Similarly to ZZ, WZ and WW productions are also simulated with POWHEG interfaced with Pythia8. In WZ, two final states have been considered as being dominant, $WZ \to \ell\nu\ell^+\ell^-$ and $WZ \to \ell\nu\nu\nu$. In WW, the final state with both W bosons decaying to leptons, $WW \to \ell\nu\ell\nu$ has been considered. A minimum mass of 4 GeV is required for each charged lepton couple. Details about these samples are given in Table 5.3.

Process	Generator	σ (pb)	k-factor	Filter efficiency
$WZ \to \ell\nu\ell^+\ell^-$	POWHEG+Pythia8	4.4625	1.0	1.0
$WZ \to \ell\nu\nu\nu$	POWHEG+Pythia8	2.7778	1.0	1.0
$WW \to \ell\nu\ell\nu$	POWHEG+Pythia8	10.631	1.0	1.0
$WZ \to \ell\nu\ell^+\ell^-$	POWHEG+Pythia8 ($m_T$filtered)	4.4953	1.0	0.004893
$WZ \to \ell\nu\ell^+\ell^-$	SHERPA	4.583	1.0	1.0

Table 5.3: Cross sections at the NLO in perturbation theory, k-factors and filter efficiencies for WZ and WW POWHEG+Pythia8 samples at $\sqrt{s} = 13$ TeV.

5.2.2.5 Z+jets production

The Z+jets process is simulated using SHERPA 2.2.1 event generator. However, studies have shown considerable Zp_T mismodeling with SHERPA samples, a bin-by-bin reweighting of the Zp_T distribution is applied to Z+jets samples, which was performed using the ratio between data and MC.

Details for SHERPA Z+jets sample are summarized in Tables 5.4, 5.5, and 5.6 for $Z \to ee$, $Z \to \mu\mu$ and $Z \to \tau\tau$ processes respectively.

Process	Generator	σ (pb)	k-factor	Filter efficiency
$Z \to ee$_MAXHTPTV0_70_CVetoBVeto	SHERPA	1981.8	0.9751	0.82106
$Z \to ee$_MAXHTPTV0_70_CFilterBVeto	SHERPA	1980.8	0.9751	0.11295
$Z \to ee$_MAXHTPTV0_70_BFilter	SHERPA	1981.7	0.9751	0.063809
$Z \to ee$_MAXHTPTV70_140_CVetoBVeto	SHERPA	110.5	0.9751	0.69043
$Z \to ee$_MAXHTPTV70_140_CFilterBVeto	SHERPA	110.63	0.9751	0.18382
$Z \to ee$_MAXHTPTV70_140_BFilter	SHERPA	110.31	0.9751	0.11443
$Z \to ee$_MAXHTPTV140_280_CVetoBVeto	SHERPA	40.731	0.9751	0.61452
$Z \to ee$_MAXHTPTV140_280_CFilterBVeto	SHERPA	40.67	0.9751	0.23044
$Z \to ee$_MAXHTPTV140_280_BFilter	SHERPA	40.643	0.9751	0.14966
$Z \to ee$_MAXHTPTV280_500_CVetoBVeto	SHERPA	8.6743	0.9751	0.56134
$Z \to ee$_MAXHTPTV280_500_CFilterBVeto	SHERPA	8.6711	0.9751	0.26294
$Z \to ee$_MAXHTPTV280_500_BFilter	SHERPA	8.6766	0.9751	0.17223
$Z \to ee$_MAXHTPTV500_1000	SHERPA	1.8081	0.9751	1
$Z \to ee$_MAXHTPTV1000_E_CMS	SHERPA	0.14857	0.9751	1

Table 5.4: Cross sections at the NNLO in perturbation theory, k-factors and filter efficiencies for Z+jets SHERPA $Z \to ee$ samples at $\sqrt{s} = 13$ TeV.

Process	Generator	σ (pb)	k-factor	Filter efficiency
$Z \to \mu\mu$_MAXHTPTV0_70_CVetoBVeto	SHERPA	1983	0.9751	0.8221
$Z \to \mu\mu$_MAXHTPTV0_70_CFilterBVeto	SHERPA	1978.4	0.9751	0.11308
$Z \to \mu\mu$_MAXHTPTV0_70_BFilter	SHERPA	1982.2	0.9751	0.064161
$Z \to \mu\mu$_MAXHTPTV70_140_CVetoBVeto	SHERPA	108.92	0.9751	0.68873
$Z \to \mu\mu$_MAXHTPTV70_140_CFilterBVeto	SHERPA	109.42	0.9751	0.18596
$Z \to \mu\mu$_MAXHTPTV70_140_BFilter	SHERPA	108.91	0.9751	0.11375
$Z \to \mu\mu$_MAXHTPTV140_280_CVetoBVeto	SHERPA	39.878	0.9751	0.60899
$Z \to \mu\mu$_MAXHTPTV140_280_CFilterBVeto	SHERPA	39.795	0.9751	0.23308
$Z \to \mu\mu$_MAXHTPTV140_280_BFilter	SHERPA	43.675	0.9751	0.13769
$Z \to \mu\mu$_MAXHTPTV280_500_CVetoBVeto	SHERPA	8.5375	0.9751	0.55906
$Z \to \mu\mu$_MAXHTPTV280_500_CFilterBVeto	SHERPA	8.5403	0.9751	0.26528
$Z \to \mu\mu$_MAXHTPTV280_500_BFilter	SHERPA	8.4932	0.9751	0.17559
$Z \to \mu\mu$_MAXHTPTV500_1000	SHERPA	1.7881	0.9751	1
$Z \to \mu\mu$_MAXHTPTV1000_E_CMS	SHERPA	0.14769	0.9751	1

Table 5.5: Cross sections at the NNLO in perturbation theory, k-factors and filter efficiencies for Z+jets SHERPA $Z \to \mu\mu$ samples at $\sqrt{s} = 13$ TeV.

Process	Generator	σ (pb)	k-factor	Filter efficiency
$Z \to \tau\tau$_MAXHTPTV0_70_CVetoBVeto	SHERPA	1981.6	0.9751	0.82142
$Z \to \tau\tau$_MAXHTPTV0_70_CFilterBVeto	SHERPA	1978.8	0.9751	0.11314
$Z \to \tau\tau$_MAXHTPTV0_70_BFilter	SHERPA	1981.8	0.9751	0.064453
$Z \to \tau\tau$_MAXHTPTV70_140_CVetoBVeto	SHERPA	110.37	0.9751	0.68883
$Z \to \tau\tau$_MAXHTPTV70_140_CFilterBVeto	SHERPA	110.51	0.9751	0.1829
$Z \to \tau\tau$_MAXHTPTV70_140_BFilter	SHERPA	110.87	0.9751	0.110886
$Z \to \tau\tau$_MAXHTPTV140_280_CVetoBVeto	SHERPA	40.781	0.9751	0.60821
$Z \to \tau\tau$_MAXHTPTV140_280_CFilterBVeto	SHERPA	40.74	0.9751	0.22897
$Z \to \tau\tau$_MAXHTPTV140_280_BFilter	SHERPA	40.761	0.9751	0.13442
$Z \to \tau\tau$_MAXHTPTV280_500_CVetoBVeto	SHERPA	8.5502	0.9751	0.56036
$Z \to \tau\tau$_MAXHTPTV280_500_CFilterBVeto	SHERPA	8.6707	0.9751	0.26245
$Z \to \tau\tau$_MAXHTPTV280_500_BFilter	SHERPA	8.6804	0.9751	0.17313
$Z \to \tau\tau$_MAXHTPTV500_1000	SHERPA	1.8096	0.9751	1
$Z \to \tau\tau$_MAXHTPTV1000_E_CMS	SHERPA	0.14834	0.9751	1

Table 5.6: Cross sections at the NNLO in perturbation theory, k-factors and filter efficiencies for Z+jets SHERPA $Z \to \tau\tau$ samples at $\sqrt{s} = 13$ TeV.

5.2.2.6 Tri-boson production

Tri-boson production VVV, with $V = W$ or Z, is simulated by the SHERPA event generator at the NLO; cross sections, k-factors and filter efficiencies are reported in Table 5.7.

Process	Generator	σ (pb)	k-factor	Filter efficiency
$WWW \to 3\ell 3\nu$	SHERPA	0.008343	1.0	1.0
$WWZ \to 4\ell 2\nu$	SHERPA	0.001734	1.0	1.0
$WWZ \to 2\ell 4\nu$	SHERPA	0.0034299	1.0	1.0
$WZZ \to 5\ell 1\nu$	SHERPA	0.00021783	1.0	1.0
$WZZ \to 3\ell 3\nu$	SHERPA	0.0019248	1.0	0.44444
$ZZZ \to 6\ell 0\nu$	SHERPA	1.7059×10^{-5}	1.0	1.0
$ZZZ \to 4\ell 2\nu$	SHERPA	0.00044125	1.0	0.22542

Table 5.7: Cross sections at the NLO in perturbation theory, k-factors and filter efficiencies for triboson samples at $\sqrt{s} = 13$ TeV.

5.2.2.7 Inclusive W production

As for W+jets, $W \to e\nu_e$, $W \to \mu\nu_\mu$ and $W \to \tau\nu_\tau$ processes have been simulated with different generators to check the modeling of various distributions. The POWHEG event generator with AZNLO CTEQ6L1 tune, interfaced with Pythia8 for the parton showering was used as a baseline, details are given in Table 5.8.

Process	Generator	σ (pb)	k-factor	Filter efficiency
$W \to e\nu_e, \mu\nu_\mu, \tau\nu_\tau$	POWHEG+Pythia8	11306.0	1.0172	1.0

Table 5.8: Cross sections at the NLO in perturbation theory, k-factors and filter efficiencies for W+jets POWHEG+Pythia8 samples at $\sqrt{s} = 13$ TeV.

5.2.2.8 Top-pair and single top production

Background samples for top-pair production, as well as single top and Wt production are simulated using POWHEG interfaced with Pythia6. The $t\bar{t}$ is filter at the event generator level requiring at least one lepton originating from a W boson with $p_T > 1$ GeV. Single top production is considered in s-channel and t-channel, while

for Wt single top associated production, di-lepton filtered samples have been used. Details about these samples are given in Table 5.9.

Process	Generator	σ (pb)	k-factor	Filter efficiency
$t\bar{t}$	POWHEG+Pythia6	696.12	1.1949	0.543
single t (s-channel, $W \to l\nu$, $l = e, \mu, \tau$)	POWHEG+Pythia6	2.052	1.005	1.0
single anti-top (s-channel, $W \to l\nu$, $l = e, \mu, \tau$)	POWHEG+Pythia6	1.262	1.022	1.0
single t (t-channel, $W \to l\nu$, $l = e, \mu, \tau$)	POWHEG+Pythia6	43.739	1.0094	1.0
single anti-top (t-channel, $W \to l\nu$, $l = e, \mu, \tau$)	POWHEG+Pythia6	25.778	1.0193	1.0
Wt (di-lepton, $W \to l\nu$, $l = e, \mu, \tau$)	POWHEG+Pythia6	3.584	1.054	1.0
$W\bar{t}$ (di-lepton, $W \to l\nu$, $l = e, \mu, \tau$)	POWHEG+Pythia6	3.581	1.054	1.0

Table 5.9: Cross sections at the NLO in perturbation theory, k-factors and filter efficiencies for top-pair, single top and Wt POWHEG+Pythia6 samples at $\sqrt{s} = 13$ TeV.

5.2.2.9 $t\bar{t}V$ and $t\bar{t}VV$ production

Background samples for top-pair production in association with one or two vector bosons (W or Z) are simulated with MadGraph generator interfaced with Pythia8. These samples have a minor impact on the total background in $\ell^+\ell^-$+$E_{\mathrm{T}}^{\mathrm{miss}}$ final state; their cross sections are given in Table 5.10.

Process	Generator	σ (pb)	k-factor	Filter efficiency
$ttZ\_Np0, Z \to ll$	MADGRAPH+Pythia8	0.018103	1.2	1.0
$ttZ\_Np1, Z \to ll$	MADGRAPH+Pythia8	0.030629	1.2	1.0
ttW_Np0	MADGRAPH+Pythia8	0.009624	1.35	1.0
ttW_Np1	MADGRAPH+Pythia8	0.017344	1.35	1.0
ttW_Np2	MADGRAPH+Pythia8	0.009625	1.35	1.0
$ttWW$	MADGRAPH+Pythia8	0.008098	1.22	1.0

Table 5.10: Cross sections at NLO in perturbation theory, k-factors and filter efficiency for ttV/ttVV MADGRAPH+Pythia8 samples at $\sqrt{s} = 13$ TeV.

5.3 Event Selection

This section describes the selection of the objects used in the analyses and event selection to separate signal from backgrounds.

5.3.1 Object Selection

5.3.1.1 Muons

Combined muons as described in Section 4.4.1 are selected and used in this analysis. A transverse momentum p_{T} greater than 20 GeV and $|\eta| < 2.5$ are required for the signal muons.

Identification is performed following recommendations provided by the Muon Combined Performance Group [85] (MCP) and is applied through the MuonSelectorTools-00-05-41. The "medium" identification criterion is chosen, which is based on the requirements on the number of hits in the different inner detector and muon spectrometer sub-systems, and on the compatibility between inner detector and muon spectrometer momentum measurements to suppress the contamination due to hadrons mis-identified as muons.

To suppress the contribution from cosmic muons and non-prompt muons a cut on the impact parameters with respect to the primary vertex is applied to the muon track in the ID, specifically $|d_0/\sigma(d_0)|$ (d_0 significance) < 3 and $|z_0 \cdot sin(\theta)| < 0.5$ mm are required.

In order to avoid muons associated with jets, in particular, to additionally suppress semi-leptonic decays of b hadrons, the candidates are required to be isolated. Isolation is based on the activity observed in the calorimeter and in the tracker respectively, in a cone of radius $\Delta R = \sqrt{(\Delta\eta)^2 + (\Delta\phi)^2} = 0.2$ around the muon object. Isolation is applied using IsolationSelection-00-06-05 tool, which defines different working points according to the target isolation efficiencies. "Loose" selection has been requested for muons, which corresponds to an isolation efficiency $\geq 99\%$ for muons with $p_{\mathrm{T}} > 20$ GeV.

Finally, to account for effects of detector resolution that are not well reproduced in MC samples, the transverse momentum of muon is smeared and weights are applied to account for the difference in efficiency. Smearing is applied through the MuonMomentumCorrections-01-00-60, which also provides scale factors for differences in efficiency between data and MC.

Table 5.11 summarizes the muon selection.

Identification	Combined with Medium quality
Kinematic cuts	$p_{\mathrm{T}} > 20$ GeV $\lvert\eta\rvert < 2.5$
Cosmic cuts	$\lvert d_0$ significance $\rvert < 3$ $\lvert z_0 \cdot sin(\theta)\rvert < 0.5$ mm
Isolation	Loose

Table 5.11: Summary of muon selection.

5.3.1.2 Electrons

Electrons are reconstructed by matching the ID track to an energy cluster in the electromagnetic calorimeter (EM). The track is required to have a minimum number of hits in the tracking detectors. To the scope of these analyses, $E_{\mathrm{T}} > 20$ GeV and $|\eta| < 2.47$ are selected.

Electrons identification is applied using the ElectronPhotonSelectorTools-00-02-92-18 tool provided by the Egamma Combined Performance group (ECP) [86]. Identification is done forming a likelihood discriminator built with the shower shapes, track-cluster matching and some of the track quality distributions. The tool provides several working points for likelihood identification of electron candidates corresponding to different efficiency and fake rejection probability. The "medium" working point is used for electrons in this analysis. The pseudorapidity of the electron is taken from the cluster when applying the fiducial cuts and from the track in all other cases.

To suppress the contribution from non-prompt electrons a cut on the impact parameters with respect to the primary vertex is applied to the electron track in the ID, specifically $|d_0$ significance $| < 5$ and $|z_0 \cdot sin(\theta)| < 0.5$ mm are required.

Electrons are required to be isolated with respect to other tracks and calorimeter clusters. A p_{T}-dependent cone-based isolation requirement is applied with the IsolationSelection-00-06-05 tool and the Loose working point is chosen.

Energy calibration and smearing are retrieved through the ElectronPhotonFour MomentumCorrection-02-03-00 package, to account for differences in data and MC, and the corresponding efficiency scale factors are obtained with the package Electron EfficiencyCorrection-00-01-94.

Table 5.12 summarizes the electron selections.

Identification	Likelihood Medium ID
Kinematic cuts	$p_{\mathrm{T}} > 20$ GeV $\lvert\eta\rvert < 2.47$
Cosmic cuts	$\lvert d_0$ significance$\rvert < 5$ $\lvert z_0 \cdot sin(\theta)\rvert < 0.5$ mm
Isolation	Loose

Table 5.12: Summary of electron selection.

5.3.1.3 Jets

Jets are reconstructed with the anti-k_T algorithm [87] with a radius parameter of R = 0.4. Three dimensional topological clusters (topo-clusters) of calorimeter cell energies are used to feed the jet finding algorithm [88]. The three-dimensional topo-clusters are built from topologically connected calorimeter cells that contain a significant signal above noise. Jets are first calibrated to the hadronic scale with the effect of removing pile-up, then in-situ techniques are used to obtain calibration constants that correct MC to obtain a better agreement with data.

Jet with $p_{\mathrm{T}} > 20$ GeV and reconstructed in the region $|\eta| < 4.5$ are used in the analyses. To further reduce the effect of pile-up jets a cut on the jet-vertex-fraction (JVF) variable is applied for each jet. The JVF is defined as the scalar sum of the transverse momentum of the tracks associated to the jet and originates from the hard-scattering vertex, divided by the scalar sum of the transverse momentum of all the tracks. The JVF is combined with other variables in a multivariate discriminant called the Jet Vertex Tagger (JVT) which is then used in the corresponding tool at the analysis level to select jets from the hard-scatter vertex [89]. The recommended 0.59 upper threshold on the JVT is used in the analyses to reject jets with $p_{\mathrm{T}} < 60$ GeV, $|\eta| <2.4$, which corresponds to an efficiency of 92% and to an observed fake rate of 2%. If such a jet passes the JVT cut, but is "bad" [95], then the whole event is rejected.

Last, jets are retained in the analyses only if they pass the "Loose" selection criteria for the Jet Cleaning [90], designed to provide an efficiency of selecting jets from proton-proton collisions above 99.5% for $p_{\mathrm{T}} > 20$ GeV.

A veto on b-tagged jets with $p_{\mathrm{T}} > 20$ GeV and $|\eta| < 2.5$ is applied in the analyses

to reject the contribution from $t\bar{t}$ background events. For these analyses, a jet is b-tagged if the MV2c10 weight is larger than a cut value corresponding to approximately 85% b-tagging efficiency for b-jets in $t\bar{t}$ events.

5.3.1.4 Missing Transverse Momentum

The imbalance of visible momenta in the plane transverse to the beam axis is known as the Missing Transverse Momentum, $E_{\mathrm{T}}^{\mathrm{miss}}$. It is computed as the negative of the global vector sum of all identified physics objects (electrons, muons, jets, etc.) as well as "soft term" accounting for unclassified soft tracks and calorimeter clusters.

These analyses use the track-based soft term $E_{\mathrm{T}}^{\mathrm{miss}}$, also called TST $E_{\mathrm{T}}^{\mathrm{miss}}$ [93]. It is built by combining the information provided by the ID and the calorimeter in order to minimize the effect of pile-up which causes a degradation of $E_{\mathrm{T}}^{\mathrm{miss}}$ performance, as already observed in Run-I. In TST $E_{\mathrm{T}}^{\mathrm{miss}}$ the soft term is computed using momentum of those tracks associated to the primary vertex, while the momentum of hard objects is computed at the calorimeter level, to allow also the measurement of neutral particles momenta.

$E_{\mathrm{T}}^{\mathrm{miss}}$ is reconstructed at the analysis level using the METUtilities-00-02-46 package provided by the Jet-$E_{\mathrm{T}}^{\mathrm{miss}}$ performance group [94], considering all the calibrated objects in the event. The $E_{\mathrm{T}}^{\mathrm{miss}}$ interface is provided by METInterface-00-02-08 package.

Jet-muon overlap handling is enabled in $E_{\mathrm{T}}^{\mathrm{miss}}$. This corrects for fake jets due to pile up close to muons which pass the JVT requirement and double counts jets from muon energy losses. In addition, jets from final-state-radiation (FSR) photons are converted from hadronic jet energy scale to EM scale.

5.3.1.5 Overlap Removal

Possible overlaps among the various objects are resolved followed recommendations from the harmonization group [92].

Table 5.13 summarizes the overlaps removal strategy used in the analyses.

5.3.2 Event Selection

5.3.2.1 Trigger Requirement

The data used in the analysis are triggered with single lepton triggers (electron or muon). The trigger menu used is reported in Table 5.14.

	Reference objects	Criteria
Remove jets	electrons	$\Delta R_{e-jet} < 0.2$
	muons	$\Delta R_{\mu-jet} < 0.2$ if $N_{Trk}(jet) < 3$ OR ($p_{\mathrm{T}}^{jet}/p_{\mathrm{T}}^{\mu} < 2$ and $p_{\mathrm{T}}^{\mu}/\Sigma_{TrkPt} > 0.7$)
Remove electrons	jets	$0.2 < \Delta R_{e-jet} < 0.4$ **AND** pile-up jets check
	muons	share the same ID track
remove muons	jets	$\Delta R_{\mu-jet} < 0.4$ **AND** pile-up jets check

Table 5.13: Overlap removal criteria adopted in the analyses. Pile-up jets check means JVT > 0.59 if jet $p_{\mathrm{T}} < 60$ GeV and $|\eta| < 2.4$.

	Trigger selection
Single Muon	mu20_iloose_L1MU15 OR mu50 (2015) mu24_ivarmedium OR mu50 (2016) mu26_ivarmedium OR mu50 (2016, after $10^{34}\mathrm{cm}^{-2}\mathrm{s}^{-1}$)
Single Electron	e24_lhmedium_L1EM18VH OR e60_lhmedium OR e120_lhloose (2015) e24_lhtight_nod0_ivarloose OR e60_lhmedium_nod0 (2016) OR e140_lhloose_nod0 (2016) e26_lhtight_nod0_ivarloose OR e60_lhmedium_nod0 (2016, after $10^{34}\mathrm{cm}^{-2}\mathrm{s}^{-1}$) OR e140_lhloose_nod0 (2016, after $10^{34}\mathrm{cm}^{-2}\mathrm{s}^{-1}$)

Table 5.14: Trigger requirement in $\ell^+\ell^-+E_{\mathrm{T}}^{\mathrm{miss}}$ analyses in 2015 and 2016 data periods.

According to the studies using with 2015 data and MC15b [96], the combination of the single-electron and single-muon trigger turns out to be always greater than 99%. Similarly, checks were done for single lepton triggers with 2016 data and MC15c for signals. Efficiencies for individual triggers always exceeded 95%. Due to the sharp turn-on curve of single lepton trigger efficiencies, we use the $p_{\mathrm{T}} > 30$ GeV for the leading lepton, which has been proven to keep the high signal efficiency.

5.3.2.2 Event Preselection

To exclude events in problematic luminosity blocks, all data events are required to pass the "All_Good" Good Run List (GRL). A set of other quality checks on data events are applied, following the recommendations of the data preparation group. In particular events affected by detector/read-out problems are removed if either Calorimeter quality flags are not good or events are incomplete.

The presence of an hard-scattering vertex with at least two associated tracks is required, being this vertex the one with the highest sum of p_{T}^2.

In order to remove jets originating from non-collision events, such as hardware problems, cosmic-ray showers or beam related backgrounds, a set of jet cleaning criteria is applied. These jets can give rise to fake missing transverse momentum that manifests in a poor description of the tail of the $E_{\mathrm{T}}^{\mathrm{miss}}$ distribution. Events with bad quality jets, defined as $p_{\mathrm{T}} > 20$ GeV jets not passing the "Loose" selection criteria for the Jet Cleaning [90], are then rejected.

5.3.2.3 Final Event Selection

By studying various physics kinematic distributions related to the di-lepton + $E_{\mathrm{T}}^{\mathrm{miss}}$ final state, one can choose seven most sensitive variables (as shown in Figure 5.3) to separate signal and backgrounds.

Potential signal candidate can be selected by applying the following requirements:

- The invariant mass of the two leptons is required to be compatible with Z boson mass: $76 < m_{\ell\ell} < 106$ GeV. This requirement can significantly reduce the events that do not include Z boson, for example, $t\bar{t}$, $WW \to \ell\nu\ell\nu$, etc. Figure 5.2 shows the invariant mass of the two selected leptons for 5.2a electron channel and for 5.2b muon channel.

- In order to suppress the Z+jets background, the signal events are required to have $E_{\mathrm{T}}^{\mathrm{miss}}$ greater than 90 GeV.

- Due to the large p_{T} of the boosted Z boson in $Zh \to \ell\ell +$ invisible signal, the angular distance ($\Delta R = \sqrt{\Delta\phi^2 + \Delta\eta^2}$) between the two leptons is required to be smaller than 1.8.

- Considering that the $E_{\mathrm{T}}^{\mathrm{miss}}$ is expected to be back-to-back with the Z boson in the signal, the azimuthal angular difference between $E_{\mathrm{T}}^{\mathrm{miss}}$ and Z boson is required to be greater than 2.7.

- Given the momentum conservation in the transverse plane, the $E_{\mathrm{T}}^{\mathrm{miss}}$ plus jets are expected to be balanced against the p_{T} of Z boson. Hence, the fractional p_{T} difference $|p_{\mathrm{T}}^{\mathrm{miss,jet}} - p_{\mathrm{T}}^{\ell\ell}|/p_{\mathrm{T}}^{\ell\ell} < 0.2$, where $p_{\mathrm{T}}^{\mathrm{miss,jet}} = |\vec{E}_{\mathrm{T}}^{\mathrm{miss}} + \sum_{\mathrm{jet}} \vec{p}_{\mathrm{T}}^{\mathrm{jet}}|$.

- To further suppress the $Z+$ jets background, events are required to have $E_{\mathrm{T}}^{\mathrm{miss}}/H_{\mathrm{T}} > 0.6$, where $H_{\mathrm{T}} = \sum_{\mathrm{jet}} p_{\mathrm{T}}^{\mathrm{jet}} + p_{\mathrm{T}}^{\ell_1} + p_{\mathrm{T}}^{\ell_2}$.

- Finally, in order to suppress the top backgrounds, the events with at least one b-tagged jet are vetoed.

The criteria for selecting signal events are summarized in Table 5.15.

Variable	Value
Di-lepton selection	Exactly one ee or $\mu\mu$ pair (as defined above) with leading (subleading) lepton $p_{\mathrm{T}} > 30$ (20) GeV. Opposite charge is required for both ee and $\mu\mu$ pairs.
Third lepton	Veto any additional leptons with $p_{\mathrm{T}} > 7$ GeV.
$m_{\ell\ell}$	76 - 106 GeV
$E_{\mathrm{T}}^{\mathrm{miss}}$	> 90 GeV
$\Delta R_{\ell\ell}$	< 1.8
$\lvert\Delta\phi(p_T^Z, E_{\mathrm{T}}^{\mathrm{miss}})\rvert$	> 2.7
Fractional p_{T} difference	< 0.2
$E_{\mathrm{T}}^{\mathrm{miss}}/H_{\mathrm{T}}$	> 0.6
b-jet veto	Veto events with b-tagged jets

Table 5.15: List of the event selections.

The cut points (optimal values) in the above table can be derived by performing statistical significance scan of all the variables in a multi-dimensional space. The combination of each cut values achieving the highest significance will be the optimal values. The significance is defined as [111]:

$$Z = \sqrt{2\left((S+B)\log(1+S/B) - S\right)}, \tag{5.1}$$

which is a standard for Poisson counting experiment for regions of high and low statistics where the background is known with small uncertainty. In the equation, S means signal yields and B represents background yields.

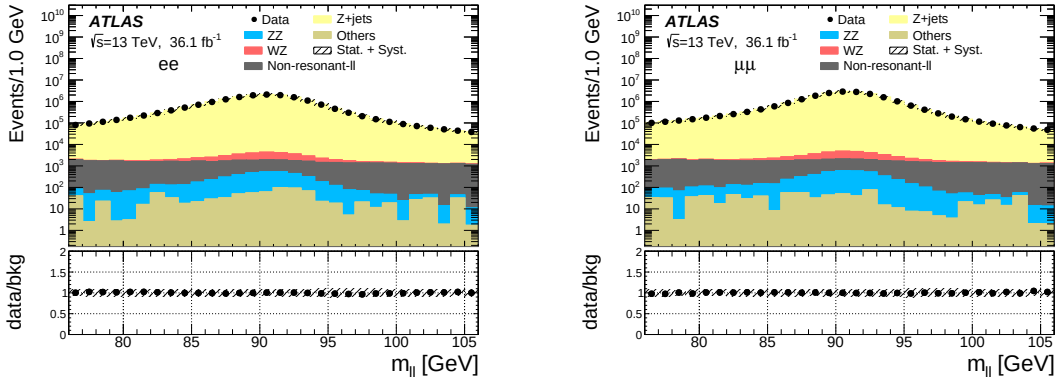

(a) (b)

Figure 5.2: The invariant mass of leptons that pass the object selections in the (a) electron channel and (b) muon channel. Only events with two same flavor and opposite sign leptons and no additional leptons are accepted, whose invariant mass is 76 $< M_{ll} <$106 GeV. MC samples are normalized to their cross section values as given in Section 5.2.2 and re-scaled to the data integrated luminosity reported in figure. The error band in the ratio plot shows the systematic uncertainty on the MC.

5.3.2.4 Signal acceptance and systematic uncertainties

After all the cuts applied, the expectation for signal is 107.8 for ee channel and 113.9 for $\mu\mu$ channel (numbers are scaled to 36.1 fb^{-1}). The cutflow of signal sample is summarized in Table 5.16.

The theoretical uncertainties considered in the signal come from the following sources: the choice of PDF set, QCD scale uncertainties, and parton shower (PS) parameters. In addition, EW corrections are applied to the $m_h = 125$ GeV sample, and the systematic errors are also discussed.

- **PDF uncertainty:** The $Zh \to \ell\ell +$invisible signal samples are generated with the CT10nlo PDF set. Alternative PDF sets considered in the estimation of the PDF systematic uncertainty are the 26 eigenvector variations of the CT10nlo set, the nominal value of the MSTW2008nlo set, and the nominal value of the NNPDF set. The estimation of the systematic error is done by reweighting the events with the alternative MC weights (calculated using alternative PDF

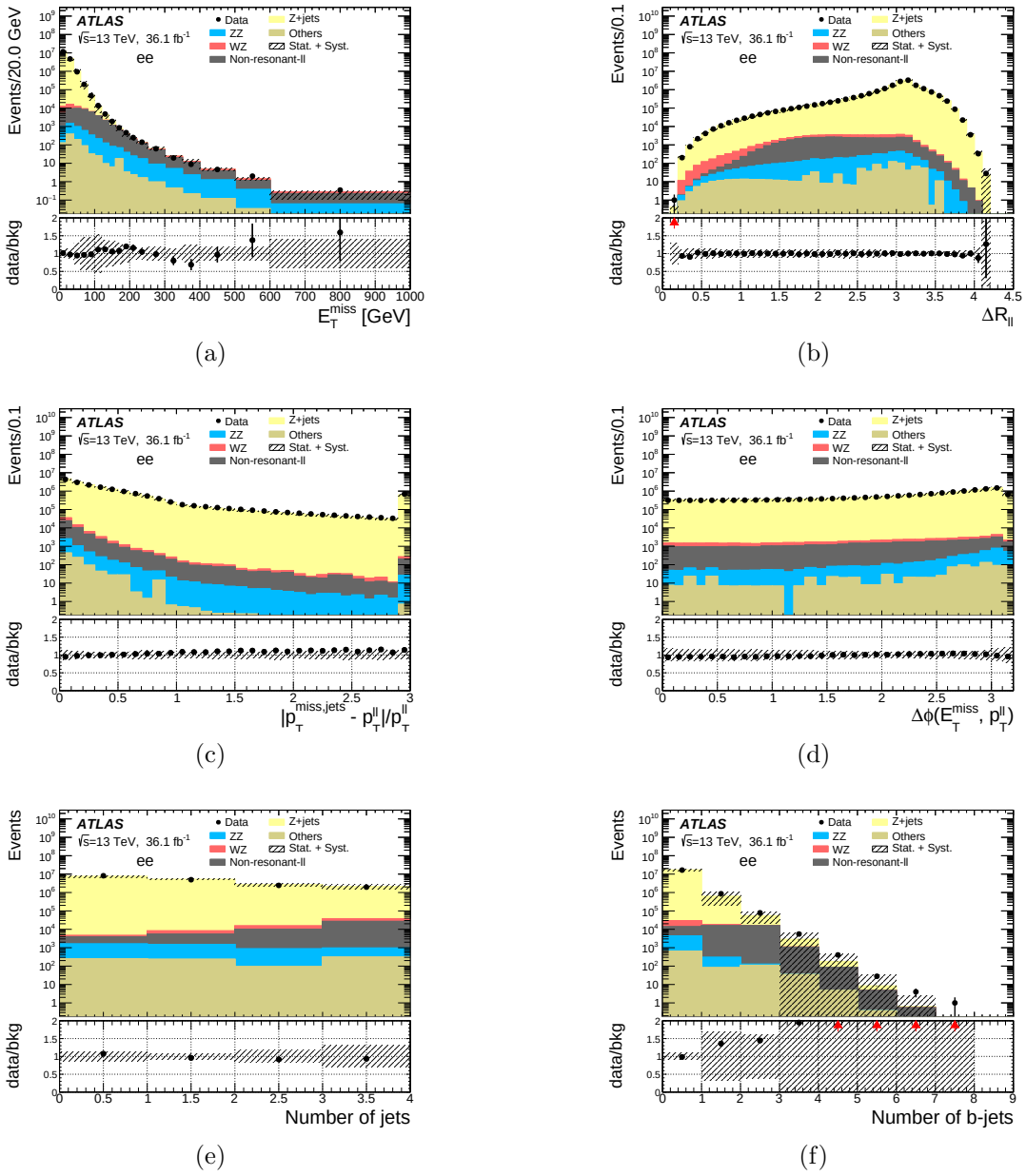

Figure 5.3: Kinematic distributions that are used for event selections in the $\ell\ell$+ $E_{\mathrm{T}}^{\mathrm{miss}}$ analyses for the signal, backgrounds and data in the electron channel after applying Z mass window cut : (a) $E_{\mathrm{T}}^{\mathrm{miss}}$, (b) the distance between leptons, ΔR_{ll}, (c) the fractional p_{T} difference, (d) the opening angle between $E_{\mathrm{T}}^{\mathrm{miss}}$ and di-lepton pair, (e) number of central jets that have $p_{\mathrm{T}} > 20$ GeV and $|\eta| < 2.5$, and (f) number of b-tagged jets. The bottom plot shows the ratio between data and all the background MC expectation. MC samples are normalized to their cross section values as given in Section 5.2.2 and re-scaled to the data integrated luminosity reported in figure. The error band in the ratio plot shows the systematic uncertainty on the MC expectation.

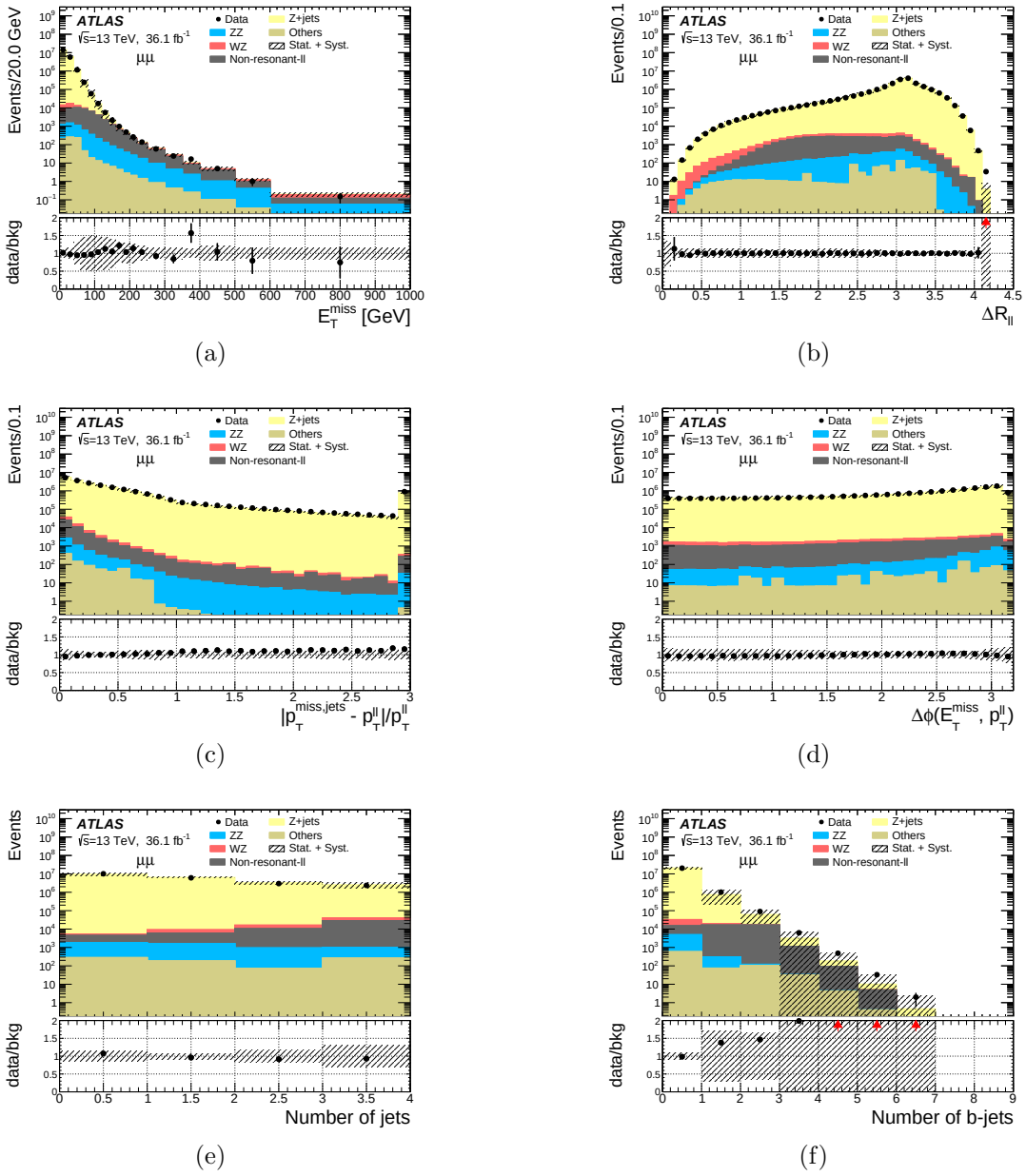

Figure 5.4: Kinematic distributions that are used for event selections in the $\ell\ell+$ $E_{\mathrm{T}}^{\mathrm{miss}}$ analyses for the signal, backgrounds and data in the muon channel after applying Z mass window cut : (a) $E_{\mathrm{T}}^{\mathrm{miss}}$, (b) the distance between leptons, ΔR_{ll}, (c) the fractional p_{T} difference, (d) the opening angle between $E_{\mathrm{T}}^{\mathrm{miss}}$ and di-lepton pair, (e) number of central jets that have $p_{\mathrm{T}} > 20$ GeV and $|\eta| < 2.5$, and (f) number of b-tagged jetse. The bottom plot shows the ratio between data and all the background MC expectation. MC samples are normalized to their cross section values as given in Section 5.2.2 and re-scaled to the data integrated luminosity reported in figure. The error band in the ratio plot shows the systematic uncertainty on the MC expectation.

Selection	$Zh \to \ell\ell + inv$ ($m_H = 125$ GeV) ee	$\mu\mu$
$m_{\ell\ell}$	399.8 ± 5.5	436.4 ± 6.0
$E_{\mathrm{T}}^{\mathrm{miss}}$	206.9 ± 3.1	220.1 ± 3.5
$\Delta R_{\ell\ell}$	170.1 ± 2.5	178.9 ± 2.8
$\Delta\phi(p_T^Z, E_{\mathrm{T}}^{\mathrm{miss}})$	138.7 ± 2.3	145.7 ± 2.5
frac. p_{T} diff.	136.9 ± 2.2	142.7 ± 2.5
$E_{\mathrm{T}}^{\mathrm{miss}}/H_T$	113.0 ± 2.1	119.5 ± 2.3
b-jet veto	107.8 ± 2.0	113.9 ± 2.3

Table 5.16: Expected $Zh \to \ell\ell$+invisible cutflow yields scaled to 36.1 fb^{-1}. Statistical errors are included.

sets) and comparing to the nominal results. The envelope that can cover the differences is treated as the systematic uncertainty. The errors evaluated for the $m_h = 125$ GeV signal are given in Table 5.17.

- **QCD scale uncertainty:** The choice of the QCD renormalization scale μ_R and factorization scale μ_F is arbitrary, and for the $Zh \to \ell\ell +$ invisible signal they are chosen as $\mu_R = \mu_F = m_{Zh}$. In order to estimate the uncertainties due to the choice of these scales, μ_R and μ_F are varied individually by a factor of 1/2 and 2 with respect to the nominal values. There are 8 combination of variations in the scales, including the case where only one scale is set to the nominal value, and excluding the case where both are nominal. The estimation is done by reweighting the nominal results with alternative weights (calculated using alternative QCD scales) and comparing to the nominal results. The envelope that can cover the differences between the scale variations and the nominal results is taken to be the QCD scale systematic uncertainty. The results are shown in Table 5.17

- **Parton Shower uncertainty:** The parton shower (PS) uncertainty is estimated by modifying the showering procedure. The nominal showering in the analysis is done using Pythia8. The alternative showering tool, Herwig 7, is interfaced with the same generator. The acceptances are derived at the truth level and compared and the difference is at the level of 0.5% for both electron and muon channels, therefore we neglect them. The results are once again shown in Table 5.17.

- **EW correction uncertainty:** NLO EW correction can have a sizable impact

on the shape of the distribution of the Higgs boson momentum, which is not accounted for in the MC Powheg + Pythia8 prediction. The EW correction has therefore been applied to the $qq \to Zh$ ($m_h = 125$ GeV)sample as a function of the truth $p_{\mathrm{T}}(Z)$, extracted from the computation of the $Zh \to \ell\ell +$invisible differential cross section using the HAWK MC software. The corrections are provided by the LHC cross-section working group [105]. The systematic uncertainty on the EW correction is computed following the prescriptions in YR4 I.5.20 [106], and shown in Figure 5.5. Its impact on the signal acceptance is evaluated to be $-1.8\%^{+2.7\%}_{-2.9\%}$ in the ee channel and $-1.9\%^{+2.8\%}_{-2.6\%}$ in the $\mu\mu$ channel.

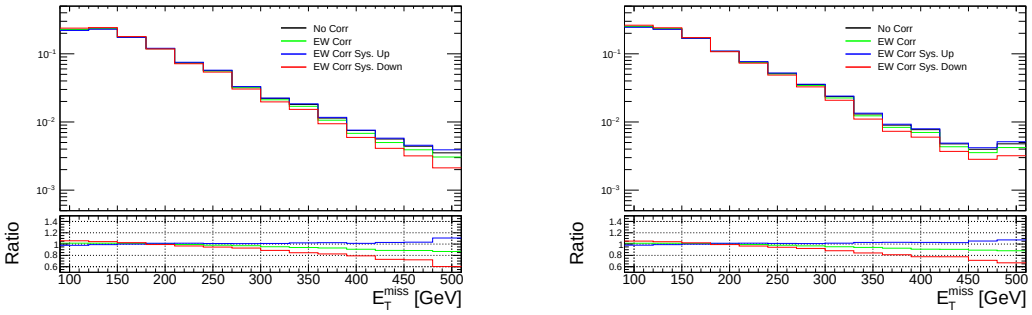

(a) (b)

Figure 5.5: $E_{\mathrm{T}}^{\mathrm{miss}}$ distributions for the $Zh \to \ell\ell +$invisible process with EW correction systematic uncertainty applied in the (a) ee and (b) $\mu\mu$ channels.

	PDF		QCD Scale		PS	
	up	down	up	down	up	down
ee	1.1%	1.2%	2.7%	5.3%	0.5%	0.5%
$\mu\mu$	1.2%	1.2%	2.3%	2.7%	0.5%	0.5%

Table 5.17: Uncertainties from PDF, QCD scale, and PS variations on the $Zh \to \ell\ell +$ invisible ($m_h = 125$ GeV) signal acceptance.

The experimental systematic uncertainties are mainly from luminosity, pileup and objects reconstruction.

Luminosity Uncertainty

The uncertainty on the integrated luminosity of combined 2015 and 2016 ATLAS data is $\pm 3.2\%$, which assumes partially correlated uncertainties, and is applied to signal and the backgrounds estimated from MC predictions.

Electron

The systematic uncertainties for electron are considered from following sources:

- Electron energy calibration and smearing: The uncertainties on the electron energy calibration and smearing are introduced and provided by ATLAS egamma group based the description [108]. A simplified model, used for this analysis, considers two systematic uncertainties: resolution and scale.

- Electron reconstruction, identification and isolation efficiency: Electron reconstruction, identification and isolation efficiencies are corrected based on the difference of MC and Data and the corresponding uncertainties are assigned as systematic uncertainties in the analysis.

- Electron trigger efficiency: The difference between Data and MC on electron trigger efficiency are corrected and the corresponding systematic uncertainty is assigned.

Muon

The systematic uncertainties for muon are considered from following sources.

- Muon momentum calibration and smearing: The estimation of effect of muon momentum calibration and smearing follow the recommendations from ATLAS Muon group[85]. Two systematic variation considered for smearing: muon_id and muon_ms represent the effect of smearing variation for ID track and MS track respectively. One scale uncertainty muon_scale is included for the effect of varying the scale of muon momentum.

- Muon reconstruction and identification: Muon reconstruction efficiency is corrected using the difference between data and MC. Two systematic variation assigned for the correction considering the statistic part and systematic part.

- Muon isolation: Similar to reconstruction efficiency, two systematic uncertainty terms for the isolation are included from statistic and systematic parts.

- Muon trigger efficiency: Similar to reconstruction efficiency, two systematic uncertainty terms for muon trigger efficiency are included: muon trigger efficiency stats uncertainty and muon trigger efficiency systematic uncertainty.

Jet

The systematic uncertainties for jets include following sources:

- Jet energy scale(JES): The determination of JES uncertainties can be found in [109]. The uncertainty from JES for each jet can be retrieved using `JetUncertainties` package which is provided by ATLAS Jet group. Three grouped uncertainties are considered i this analysis. One additional uncertainty, calibtation non-closure, is added because of an observed highly localized non-closure at $2.4 < \eta < 2.5$.

- Jet energy resolution(JER): Jet resolution (jet_JER) is corrected due to the difference of data and MC with assigned uncertainty.

- The systematic uncertainty on efficiency of JVT requirement is also included in the analysis.

Jet flavor tagging

The flavor tagging efficiency has been corrected comparing data and MC with assigned systematic uncertainty. The envelope method used in this analysis which only considers three systematic uncertainties corresponding to the uncertainties for the correction on the tagging efficiency of bottom, charm and light jets (not bottom and charm) respectively. Two additional systematic uncertainties considered for the jets with $p_T > 300$ GeV are extrapolated using MC-based method[110].

Missing Transverse Momentum

The determination and description of $E_{\mathrm{T}}^{\mathrm{miss}}$ systematic uncertainty can be found in ATLAS PubNote[93]. In this analysis, only the systematic uncertainties on $E_{\mathrm{T}}^{\mathrm{miss}}$ soft term(track-based soft term) are estimated. The effects on $E_{\mathrm{T}}^{\mathrm{miss}}$ from other terms (electron, muon, jets, and etc.) will be automatically considered when varying their corresponding objects uncertainties. Three systematic uncertainties resolution_parallel, resolution_perpendicular, soft_term_scale are included representing the uncertainties from the soft term resolution effect on the direction parallel to vector sum of hard objects p_{T} ($p_{\mathrm{T}}^{\mathrm{hard}}$), soft term resolution effect on the direction perpendicular to $p_{\mathrm{T}}^{\mathrm{hard}}$ and the effect of soft term scale on the direction parallel to $p_{\mathrm{T}}^{\mathrm{hard}}$ respectively.

The experimental systematic uncertainties on signal acceptance are summarized in the Table 5.18 below.

Experimental Systematic Uncertainty	ee channel		$\mu\mu$ channel	
	up (%)	down (%)	up (%)	down (%)
Luminosity	3.2	3.2	3.2	3.2
pile-up	2.15	2.38	1.26	1.32
Electron (reso., scale, effi.)	1.75	1.83	0.0	0.0
Muon (iso. reco. id.)	0.0	0.0	1.91	1.88
Jet (scale, reso.)	3.34	4.58	3.67	3.91
$E_{\mathrm{T}}^{\mathrm{miss}}$	0.05	0.35	0.07	0.07
Total	5.4	6.4	5.4	5.6

Table 5.18: Experimental systematic uncertainties on the $Zh \to \ell\ell + \text{invisible}$ ($m_h = 125$ GeV) signal acceptance. Up/down means the impact on fianl yields by varying the systematic uncertainties of one standard deviation upwards and downwards

The final $Zh \to \ell\ell + \text{invisible}$ signal acceptance is 107.8 $\pm$ 2.0 (stats) $\pm$ 9.4 (sys.) for ee channel and 113.9 $\pm$ 2.3 $\pm$ 7.5 for $\mu\mu$ channel.

5.4 Background Estimation and Systematic Uncertainty

The main backgrounds in this search are the Standard Model productions of ZZ and WZ, where the W bosons decay leptonically. Other backgrounds considered in the analysis are Z+jets, W+jets, WW, top single and pair productions. The following methods are used for each background estimations:

- ZZ: $ZZ \to \ell\ell\nu\nu$ is the main irreducible background. Both normalization and shape are estimated from theoretical predictions. The higher order corrections [100] are applied to MC samples to get better description for data.

- WZ: Second dominant background in the high $E_{\mathrm{T}}^{\mathrm{miss}}$ region. Normalization is derived from the three lepton control region (3lCR) and the shape is taken from data.

- Z+jets: The normalization for Z+jets background is derived from data using the ABCD method. The shape of this background is estimated from data.

- top/$Z\tau\tau$/WW: The normalization is derived from data using $e\mu$ Control Region considering the flavor symmetry and the shape is estimated from data.

- W+jets: Both normalization and shape are estimated from data using fake factor method.

- ttV/tri-boson: Small backgrounds, both normalization and shape are estimated from theory predictions.

5.4.1 ZZ Background

The ZZ background consists of contributions from two production modes, the $qqZZ$ and $ggZZ$ processes. In this analysis the simulated Monte Carlo sample for ZZ background originating from initial states with quarks ($q\bar{q} \to ZZ$) are generated with PowhegBox which is next-to-leading order in QCD and leading order in EW effects. Subsequently, Pythia8 is used for parton showering and final state radiation of the leptons. Recent theory calculations suggest an enhancement of the inclusive cross section due to NNLO QCD effects [102, 103]. To incorporate those results, an event-based k-factor reweighting of the Monte Carlo sample depending on the invariant mass of the ZZ system is performed. The k-factor is calculated using "MATRIX", which is a tool provided by the NNLO paper author.

The "MATRIX" computation is carried out differentially in m(4l) spectrum and an optimized scheme of defining m(4l) intervals (mass slicing) is used to ensure that the NNLO QCD k-factors are calculated with sufficient statistical precision. This optimization turned to be important, and it is found that an improper mass slicing could result in artificial statistical fluctuations on the differential NNLO cross-sections and cause unexpected features in the k-factor distribution. The derived NNLO QCD k-factors binned in m(4l) for the $q\bar{q} \to ZZ$ process are shown in Figure 5.6.

Besides QCD effect, there is another effect: NLO electroweak (EW) effect [104] taken account for the Powheg prediction using a reweighting method. It only corrects for weak effects in order to avoid potential double counting of final state radiation of the leptons which has already been included in the MC generation. The details of EW correction are described in [100].

The Higher order correction (NLO/LO) to the $gg \to ZZ$ continuum is considered by calculating a k-factor for massless quark loops, in the heavy top approximation and for $gg(\to h^*) \to ZZ$. A flat k-factor of 1.7 ± 1.0 is applied while the applied uncertainty of 60% results from conservative consideration.

The yields of $qqZZ$ and $ggZZ$ are summarized in Table 5.19 below:

For $qqZZ$ process, experimental systematic uncertainty sources are from the items listed in 5.3.2.4 and major ones are JET term 4% and luminosity 3.2%, as indicated in the Table below:

For $ggZZ$, the uncertainty is mainly from 60% variation on flat k-factor.

As for the theoretical uncertainties, details can be found in Section 5.4.7.1.

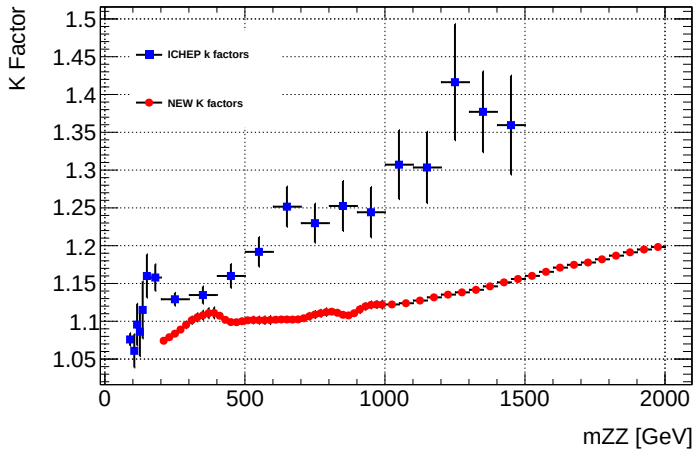

Figure 5.6: The derived NNLO QCD k-factors in binned m(4l) for the $q\bar{q} \to ZZ$ process. Also shown for comparison with the k-factors used in the previous study note which are calculated from the charged four-lepton channel [100]. The error bar in the plot represents the statistical uncertainty on the k-factor.

process	ee	$\mu\mu$
$q\bar{q} \to ZZ$	212.08 $\pm$ 2.94 $\pm$ 15.39	220.69 $\pm$ 2.94 $\pm$ 16.94
$gg \to ZZ$	18.89 $\pm$ 0.32 $\pm$ 11.18	19.25 $\pm$ 0.32 $\pm$ 11.41

Table 5.19: $qqZZ$ and $ggZZ$ yields in signal region for both ee and $\mu\mu$ channel. In each box, first number is central value of yields, second number is statistical uncertainty and third one is systematic uncertainty.

Experimental Systematic Uncertainty	ee channel		$\mu\mu$ channel	
	up (%)	down (%)	up (%)	down (%)
Luminosity	3.2	3.2	3.2	3.2
pile-up	1.16	1.51	1.60	2.76
Electron	1.81	1.75	0.0	0.0
Muon	0.0	0.0	1.84	1.82
Jet	3.61	4.07	3.53	4.17
$E_{\mathrm{T}}^{\mathrm{miss}}$	0.10	0.18	3.53	4.17
Total	5.3	5.7	5.4	6.2

Table 5.20: Experimental systematic uncertainties on the $q\bar{q} \to ZZ$ background process.

5.4.2 WZ Background

$WZ \to \ell\nu\ell^+\ell^-$ process in which the lepton from the W decay is not reconstructed is the second largest background for $\ell^+\ell^- + E_{\mathrm{T}}^{\mathrm{miss}}$ analysis. To correct the normaliza-

tion of $WZ \to \ell\nu\ell^+\ell^-$ prediction with data, we defined a 3-lepton control region (**3lCR**), where one additional lepton is required in addition to the two leptons from the Z boson decay. The third lepton is defined in the same way as the two leptons from the Z boson decay, as given in Table 5.11 and Table 5.12. Figure 5.7 and Figure 5.8 show p_{T}, η and ϕ distribution for the third lepton in 3lCR.

The shape of the final discriminant (the variable used for fit) is extracted from MC and the effect of theoretical uncertainties, coming from the variation of QCD scale and PDFs, are considered as systematic uncertainties for the shape. More details on the shape systematics are described in Section 5.4.7.1. The effect of experimental systematic uncertainties has also been considered in the shape.

5.4.2.1 Scale factor for WZ 3-lepton Control Region (3lCR)

The 3lCR is used to obtain a scale factor for the correction between observed events and WZ expectation. The scale factor is applied to renormalize the WZ expectation in the signal regions.

$$\mathrm{N}_{\mathrm{2lSR}}^{\mathrm{expected}} = \mathrm{N}_{\mathrm{2lSR}}^{\mathrm{MC}} \cdot \frac{\mathrm{N}_{\mathrm{3lCR}}^{\mathrm{data}}}{\mathrm{N}_{\mathrm{3lCR}}^{\mathrm{MC}}} = \mathrm{N}_{\mathrm{3lCR}}^{\mathrm{data}} \cdot \frac{\mathrm{N}_{\mathrm{2lSR}}^{\mathrm{MC}}}{\mathrm{N}_{\mathrm{3lCR}}^{\mathrm{MC}}} \tag{5.2}$$

Figure 5.9 shows the transverse mass m_T between the additional lepton and the $E_{\mathrm{T}}^{\mathrm{miss}}$. In a region with the transverse mass between the additional lepton and the $E_{\mathrm{T}}^{\mathrm{miss}}$ greater than 60 GeV and b-jet veto, the WZ events dominate. Figure 5.10 shows the $E_{\mathrm{T}}^{\mathrm{miss}}$ distribution after the 60 GeV cut on m_T, and the b-jet veto cut. The m_T selection removes the Z+jets contribution from the 3lCR, and the purity of WZ events in that region turns out to be ∼90%.

Three Lepton Control Region definition
Two same flavor opposite-sign leptons (e^+e^- OR $\mu^+\mu^-$)
Require one additional lepton with $p_{\mathrm{T}} > 20$ GeV
$76 < M_{\ell\ell} < 106$ GeV
$m_T(W) > 60$ GeV
b-jet Veto

Table 5.21: List of selections applied at the event selection level for the 3lCR.

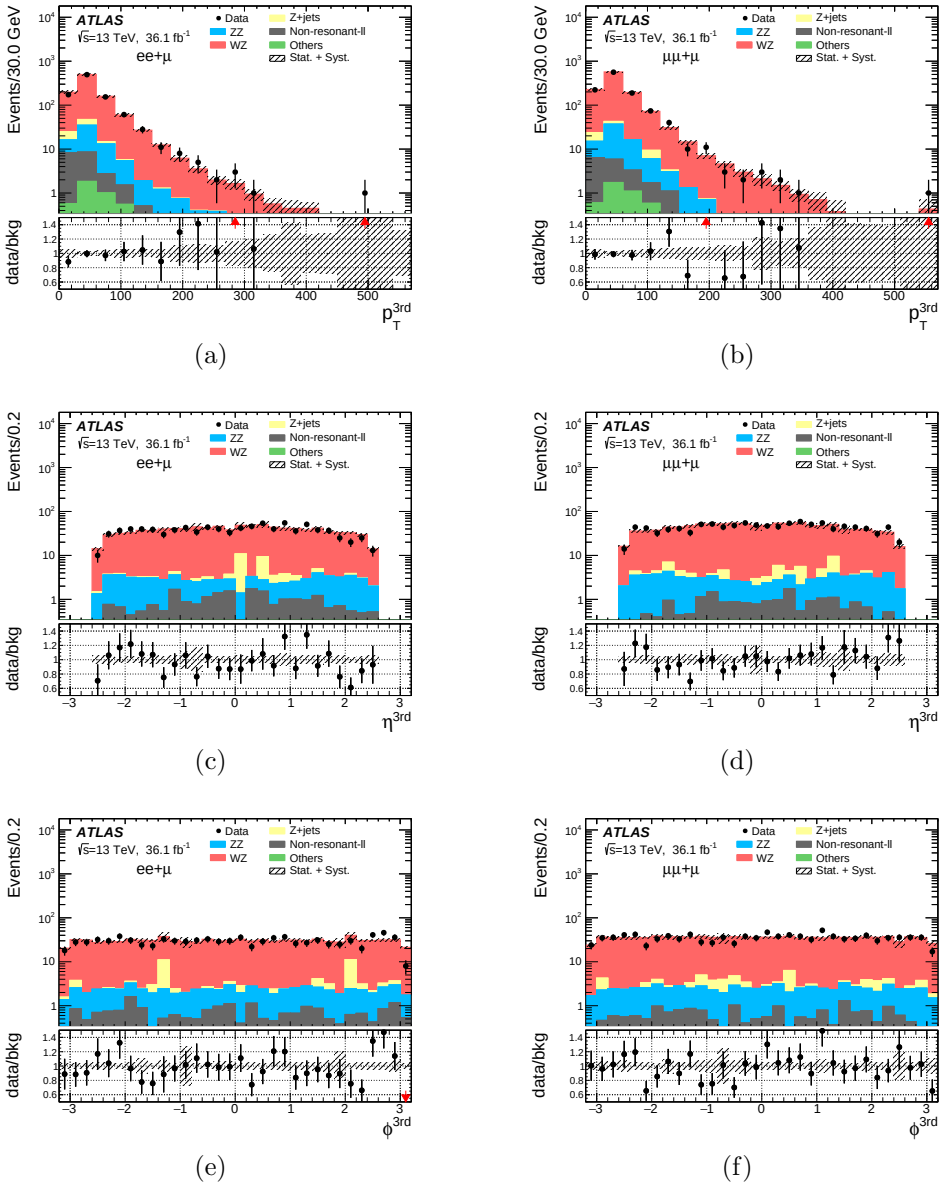

Figure 5.7: The p_{T} (top two), η (middle two) and ϕ (bottom two) distributions of the additional muon in events with two electrons (left three) or two muons (right three) with an invariant mass consistent with Z boson mass. MC samples are normalized to their cross section values as given in Section 6.2.2.2 and re-scaled to the data integrated luminosity reported in the figure. The scale factor of $1.29 \pm 0.03 \pm 0.07$ is applied to the WZ MC, and NNLO and NLO corrections are applied for ZZ. The error band in the ratio plot includes only the statistical uncertainty on MC.

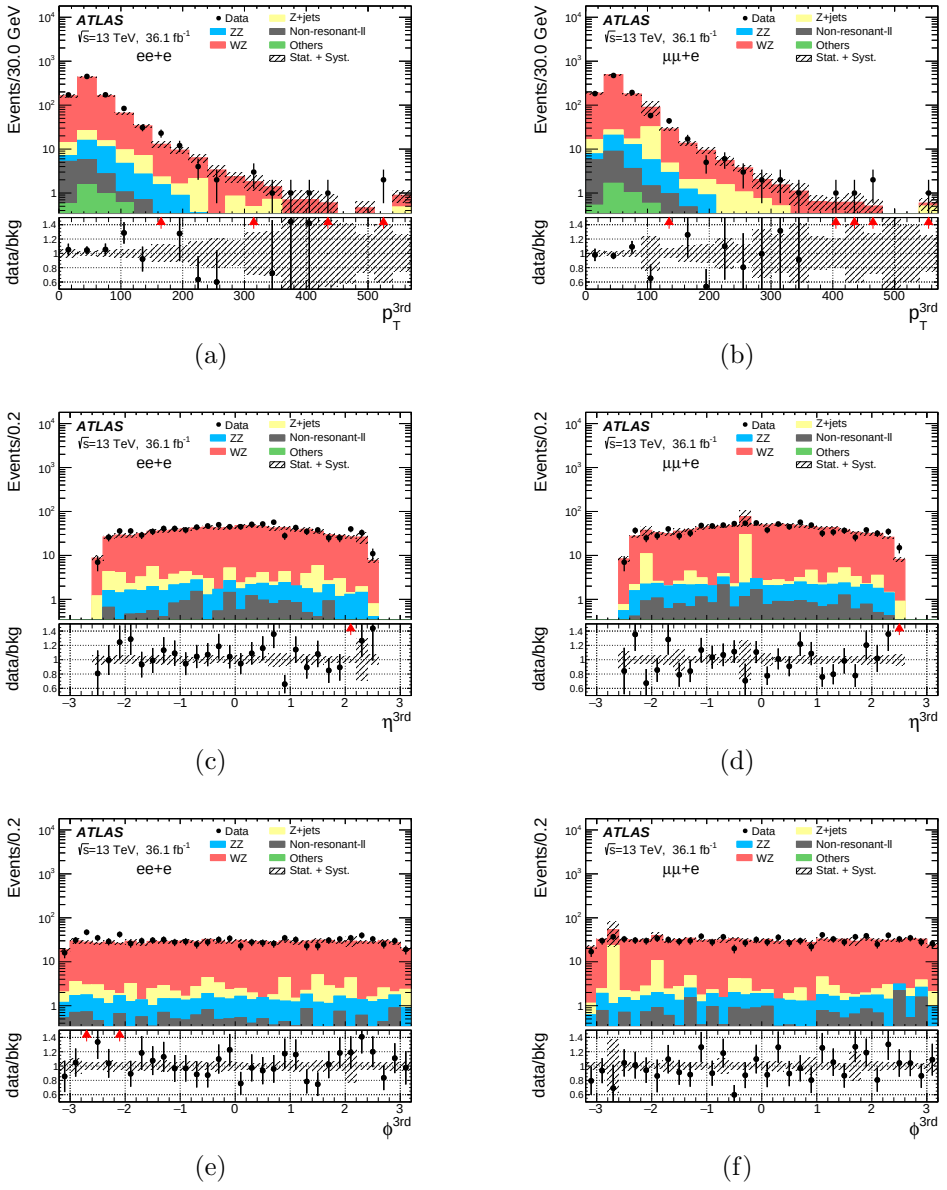

Figure 5.8: The p_{T} (top two), η (middle two) and ϕ (bottom two) distributions of the additional electron in events with two electrons (left three) or two muons (right three) with an invariant mass consistent with Z boson mass. MC samples are normalized to their cross section values as given in Section 6.2.2.2 and re-scaled to the data integrated luminosity reported in the figure. The scale factor of $1.29 \pm 0.03 \pm 0.07$ is applied to the WZ MC, and NNLO and NLO corrections are applied for ZZ. The error band in the ratio plot only includes the statistical uncertainty on MC.

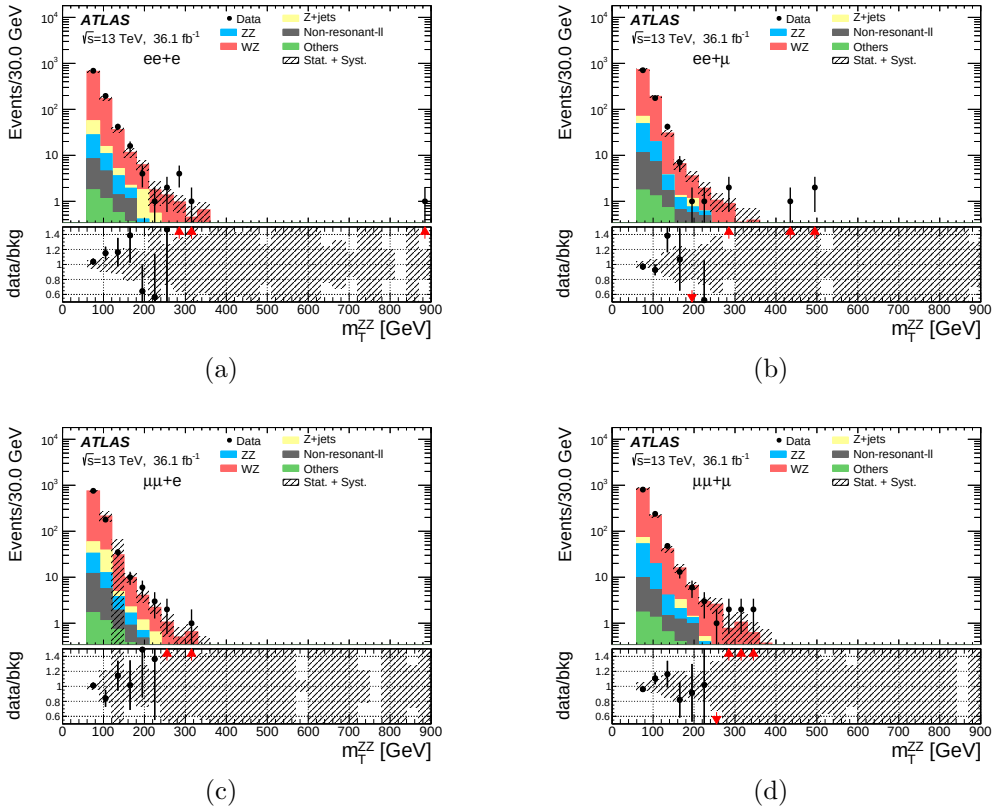

Figure 5.9: Transverse mass of the W boson for both data and Monte Carlo in (a) the ee + e channel, (b) ee + μ channel, (c) $\mu\mu$ + e channel and (d) $\mu\mu$ + μ channel in events with one additional electron or muon with respect to the lepton pair whose invariant mass is consistent with the Z boson mass. MC samples are normalized to their cross section values as given in Section 6.2.2.2 and re-scaled to the data integrated luminosity reported in the figure. The scale factor of $1.29 \pm 0.03 \pm 0.07$ is applied to the WZ MC, and NNLO and NLO corrections are applied for ZZ. The bottom plots show the ratio of the data and Monte Carlo. The red arrow in the ratio plot indicates the ratio is up/down beyond y-axis range.

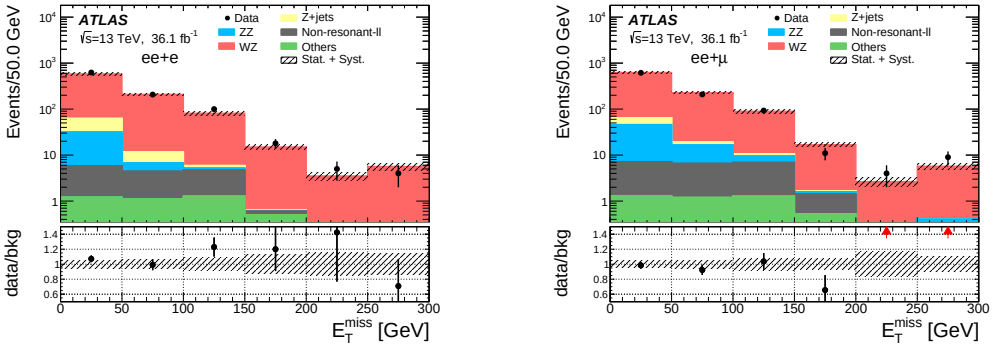

(a)

(b)

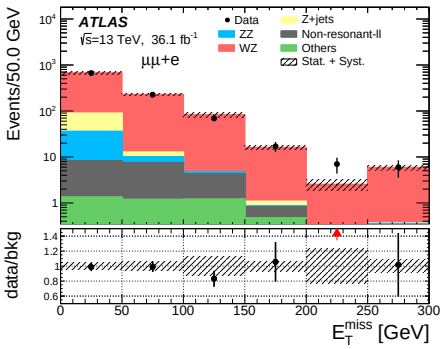

(c)

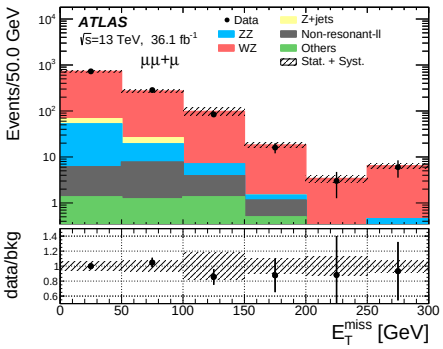

(d)

Figure 5.10: $E_{\mathrm{T}}^{\mathrm{miss}}$ distributions after M_T cut for data and Monte Carlo in (a) the ee + e channel, (b) ee + μ channel, (c) $\mu\mu$ + e channel and (d) $\mu\mu$ + μ channel in events with one additional electron or muon with respect to the lepton pair whose invariant mass is consistent with the Z boson mass. MC samples are normalized to their cross section values as given in Section 6.2.2.2 and re-scaled to the data integrated luminosity reported in the figure. For WZ background, the scale factor of $1.29 \pm 0.03 \pm 0.07$ from data-driven estimate is applied, NNLO and NLO corrections are applied for ZZ. The bottom plots show the ratio of the data and Monte Carlo. The red arrow in the ratio plot indicates that the ratio is up/down beyond y-axis range.

The systematic uncertainty on the simulation-based transfer factor between control region (CR) and signal region (SR), shown in Equation 5.2, is evaluated through the difference in acceptance due to PDF and scale variation, and has been found to be negligible (less that 5 permil as discussed in Section 5.4.7.1). The effect of the experimental systematics on this factor is taken into account and found to be $\sim 4\%$. In addition, a systematic uncertainty has been considered on the MC expectation for the two-lepton signal region concerning the third lepton veto and the inefficiency scale factor for additional leptons in the events. Finally, the statistical uncertainty on the scale factor comes from the statistics of the 3lCR in data.

In Table 5.22 the number of background and data events in the 3lCR is given for each decay mode of the Z and W bosons, together with the corresponding scale factors obtained.

channel	Expected	Observed	factor
ee + e	632.2 ± 5.0	958	1.39 ± 0.05
ee + μ	673.7 ± 5.2	941	1.25 ± 0.05
$\mu\mu$ + e	702.7 ± 5.3	993	1.26 ± 0.06
$\mu\mu$ + μ	797.6 ± 5.7	1121	1.28 ± 0.04
Total	2806.1 ± 10.6	4013	1.29 ± 0.03

Table 5.22: The expected number of background and observed number of events in the 3lCRs in $M_T > 60$ GeV and b-jet veto region. The final column shows the scale factor. It is obtained by subtracting other backgrounds (in MC) from the observed events in data, and taking the ratio between this and the expected number of events from the WZ MC. Number of observed events is for an integrated luminosity of 36.1 fb^{-1}. Error is statistical only.

The final scale factor to normalize WZ contribution is then obtained by averaging all the different decay modes together. A scale factor of $1.29 \pm 0.03 \pm 0.07$ is applied on the expected WZ yield as shown in Table 5.23.

Channel	MC only	Data-driven
ee	82.39 ± 1.91 ± 6.28	106.28 ± 2.47 ± 6.12
$\mu\mu$	87.91 ± 1.88 ± 6.87	113.40 ± 2.64 ± 5.39

Table 5.23: WZ yields in signal region for both ee and $\mu\mu$ channel. First column shows estimates based on MC only, numbers in second column are applied with scale factor $1.29 \pm 0.03 \pm 0.07$.

5.4.3 Top, WW, Wt and $Z \to \tau\tau$ Background

$t\bar{t}$, WW, Wt and $Z \to \tau\tau$ production all have a minor impact on the total background of $\ell^+\ell^- + E_{\mathrm{T}}^{\mathrm{miss}}$ analyses. Physics processes with one or more top quarks in the final state are suppressed by applying the b-jet veto cut. The WW contribution is mainly removed by requiring first that the two leptons have an invariant mass compatible with a Z boson (the "$m_{\ell\ell}$" selection), and then by applying a high $E_{\mathrm{T}}^{\mathrm{miss}}$ cut. $Z \to \tau\tau$ is suppressed because the two leptons usually have a lower invariant mass than the Z mass (due to the presence of neutrinos in the taus decay which carry away part of the energy). Finally, the Wt contribution is suppressed by the low cross section.

5.4.3.1 The method

The contribution of these backgrounds is estimated from data through a dedicated control region, named the $e\mu$ Control Region, built with the same selections as the SR except the requirement of two opposite flavor leptons (see Table 5.24). The reason for selecting opposite flavor leptons is the following: $t\bar{t}$, WW, Wt and $Z \to \tau\tau$ backgrounds all decay in the $ee : \mu\mu : e\mu$ channel with the relative probability of 1 : 1 : 2. This allows the measurement of these backgrounds directly from data using the $e\mu$ final state; the contribution in the SR is then obtained by considering the difference in the electron/muon reconstruction efficiency, accounted in the so-called ϵ-*factor*, defined as:

$$\epsilon^2 = \frac{N_{ee}}{N_{\mu\mu}} \tag{5.3}$$

where N_{ee} and $N_{\mu\mu}$ are the number of ee and $\mu\mu$ events with an invariant mass compatible with a Z boson.

The number of $e\mu$ background events in the SR is obtained as:

$$N_{SRee}^{e\mu} = \frac{1}{2} \times \epsilon \times N_{e\mu}^{data,sub} \tag{5.4}$$

$$N_{SR\mu\mu}^{e\mu} = \frac{1}{2} \times \frac{1}{\epsilon} \times N_{e\mu}^{data,sub} \tag{5.5}$$

where $N_{e\mu}^{data,sub}$ is the number of $e\mu$ data events in the CR, estimated as

$$N_{e\mu}^{data,sub} = N_{e\mu}^{data} - N_{sub}^{other} \tag{5.6}$$

$e\mu$ **Control Region Definition**
$Zh \to \ell\ell +$ **invisible**
Two Opposite flavor Opposite sign leptons ($e^{\pm}\mu^{\mp}$)
Veto any additional lepton with Loose ID and p_{T} >7 GeV
$76 < M_{e\mu} < 106$ GeV
$E_{\mathrm{T}}^{\mathrm{miss}} > 90$ GeV
$\Delta R_{e\mu} < 1.8$
$\Delta\phi(Z, E_{\mathrm{T}}^{\mathrm{miss}}) > 2.7$
Fractional p_{T} difference < 0.2
$E_{\mathrm{T}}^{\mathrm{miss}}/H_T > 0.6$
b-jet Veto

Table 5.24: Event selection applied to define the $e\mu$ Control Region. The control region reflects the SR definition except the opposite flavor requirement of the two selected leptons.

N_{sub}^{other} is defined as the non-$t\bar{t}/WW/Wt/Z \to \tau\tau$ background subtracted using data-driven (DD) estimates where available, or Monte Carlo simulations where no DD estimates are available, as in Equation 5.7.

$$N_{sub}^{other} = \sum_{i}^{non-e\mu} N_i \tag{5.7}$$

The benefit of the $e\mu$ CR defined with two opposite flavor leptons is that the $e\mu$ events from $t\bar{t}/WW/Wt/Z \to \tau\tau$ dominate in this region, since most of the contribution from processes with a Z boson is eliminated.

5.4.3.2 Efficiency correction as functions of p_{T} and η

In order to estimate the $e\mu$ background more precisely, the efficiency factor ϵ has been computed in bins of p_{T} and η for the leading and sub-leading lepton, Equation 5.3 becomes:

$$\epsilon^2 = \frac{N_{e^1_{(p_{\mathrm{T}},\eta)}e^2_{(p_{\mathrm{T}},\eta)}}}{N_{\mu^1_{(p_{\mathrm{T}},\eta)}\mu^2_{(p_{\mathrm{T}},\eta)}}} \tag{5.8}$$

The binning is chosen to ensure enough statistics in each bin to obtain efficiency factors with low statistical uncertainty. The η phase space has been divided in Barrel (B) and Endcap (E) resulting four different bins: BB, BE, EB, EE. The order is related to the order in p_{T}. For example: BE stands for a leading lepton in the Barrel and subleading lepton in the Endcap. The binning in p_{T} has been optimized as well by requiring the same amount of events for the leading lepton in three p_{T} bins for each η region. Those values have been cross-checked to provide enough and homogeneous statistics in each bin of the p_{T} scatter plot among leading and subleading lepton for each η region. The final choice of the 3 p_{T} bins is the following: $p_{\mathrm{T}} < 44$ GeV, 44 GeV $< p_{\mathrm{T}} < 52$ GeV, 52 GeV $< p_{\mathrm{T}} < 2$ TeV. The efficiency factors are then evaluated in each bin using Data, shown in Table 5.25.

The final estimates are evaluated event-by-event by applying the binned efficiency factor.and are shown in Table 6.13.

5.4.4 Z+jets background

Z+jets background is largely reduced by the $E_{\mathrm{T}}^{\mathrm{miss}}$ requirement. Moreover, other selections applied in the SR, such as $\Delta R_{\ell\ell}$, $\Delta\phi(Z, E_{\mathrm{T}}^{\mathrm{miss}})$, the fractional p_{T} difference, $E_{\mathrm{T}}^{\mathrm{miss}}/H_T$, also contribute to the reduction of Z+jets, ending with a small number of events left in the SR. However, this background has significant uncertainties, as

Lepton p_{T}(lead, sub-lead)	BB	BE	EB	EE
(30-44,20-44)	0.9469 ± 0.0004	0.8745 ± 0.0005	0.8429 ± 0.0004	0.8291 ± 0.0012
(44-52,20-44)	0.9686 ± 0.0004	0.8435 ± 0.0007	0.8226 ± 0.0006	0.7985 ± 0.0006
(44-52,44-52)	0.9380 ± 0.0007	0.7742 ± 0.0019	0.7748 ± 0.0019	0.7248 ± 0.0009
(52-2000,20-44)	0.9980 ± 0.0005	0.8715 ± 0.0008	0.8537 ± 0.0008	0.7898 ± 0.0007
(52-2000,44-52)	0.9808 ± 0.0014	0.8605 ± 0.0030	0.8648 ± 0.0030	0.7639 ± 0.0018
(52-2000,52-2000)	1.0331 ± 0.0019	0.9024 ± 0.0037	0.9180 ± 0.0038	0.8395 ± 0.0028

Table 5.25: Efficiency factor values in bin of p_{T} and η from Data. Errors contain statistical uncertainty only.

Channel	MC only	Data-driven
ee	25.52 ± 2.63 ± 5.93	29.47 ± 3.79 ± 1.58
$\mu\mu$	26.11 ± 2.86 ± 4.81	33.22 ± 4.27 ± 1.62

Table 5.26: $e\mu$ background yields in signal region for both ee and $\mu\mu$ channel. The first column shows estimates based on MC only, numbers in second column are estimated using data-driven method. Both statistical and systematic uncertainties are included.

the modeling of $E_{\mathrm{T}}^{\mathrm{miss}}$ mis-measurement in the Mc depends strongly on the correct modeling of detector, pile-up interactions, the jet energy response and the track reconstruction. It is crucial to estimate the Z+jets background by using data.

The Z+jets background is estimated by two independent data-driven methods: the "ABCD" method 5.4.4.1 and the one side-band method 5.4.4.2. The strategy is to:

- Estimate the background yields in the SR by using the "ABCD" method
- Estimate the shape of the discriminant variable distributions from the MC with a looser selection
- Estimate the uncertainty on the shape of $E_{\mathrm{T}}^{\mathrm{miss}}$ from experimental uncertainties and compare to the single side-band method.

5.4.4.1 ABCD Method

The "ABCD" method is a data-driven technique that is used to estimate the number of background events in a defined SR. The side-band control regions are built in such a way to enrich the background events and diminish the number of signal events, which is achieved by reversing some signal selections. The non-Z+jets

backgrounds contribution is further reduced by subtracting other backgrounds from side-band regions based on MC and data-driven estimates.

Provided the variables are uncorrelated, event count in signal region (A) can be estimated from side-band regions (B,C,D) using the following formula:

$$N_A^{\text{est}} = N_C^{\text{obs,sub}} \times \frac{N_B^{\text{obs,sub}}}{N_D^{\text{obs,sub}}}, \tag{5.9}$$

where N_A^{est} is the number of estimated background events in SR, while $N_X^{\text{obs,sub}}$ are the numbers of observed events in side-band regions X = B, C, D, where the contribution of non-Z+jets background is subtracted before applying this equation.

Due to large Z+jets reduction by applying additional cuts (in particular, $E_{\text{T}}^{\text{miss}}/H_T$), all attempts to construct "ABCD" suffered from very low event counts in some side-band regions and poor agreement between data and MC, as well as high correlation after final cuts, resulting in non-closure. Non-closure in this section means that particular implementation of the method does not work on MC, i.e. $N_C^{\text{MC}} \times \frac{N_B^{\text{MC}}}{N_D^{\text{MC}}} \neq N_A^{\text{MC}}$. It is decided to combine several selections in one boolean variable (pass/fail), thus increasing event counts in side-band regions by allowing events to fail any of the cuts used to construct boolean variable instead of just one cut as in traditional two-variable "ABCD". Scheme of a boolean "ABCD" regions can be seen in Figure 5.11.

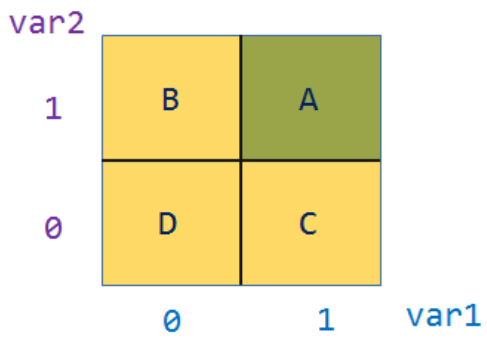

Figure 5.11: Scheme of the boolean "ABCD" method. Signal region A is defined by both variables equal true, representing all selections passed.

In order to construct combination of boolean variables with low correlation, cuts on highly-correlated variables are combined in one boolean variable. The following boolean variables are chosen based on correlation studies:

$$\text{var1} = E_{\mathrm{T}}^{\mathrm{miss}} > 90 \text{ GeV and } E_{\mathrm{T}}^{\mathrm{miss}}/H_T > 0.6 \tag{5.10}$$

$$\text{var2} = |E_T^{\mathrm{miss,jets}} - p_{\mathrm{T}}^{\ell\ell}|/p_{\mathrm{T}}^{\ell\ell} < 0.2 \text{ and } \Delta\phi(Z, E_{\mathrm{T}}^{\mathrm{miss}}) > 2.7 \text{ and } \Delta R_{\ell\ell} < 1.8 \text{ and } N_{\text{b-jets}} = 0. \tag{5.11}$$

However, with regions defined above, the method still suffers from high level of correlation, indicated by more than two-fold difference in ratios N_A^{MC}/N_B^{MC} and N_C^{MC}/N_D^{MC}. Two additional cuts are added to all side-band regions: $E_{\mathrm{T}}^{\mathrm{miss}} > 60$ GeV and $E_{\mathrm{T}}^{\mathrm{miss}}/H_T > 0.12$, which are optimized to remove the highly-correlated Z+jets bulk. The sizes of experimental uncertainties are also considered for optimization: the optimal points where the detector response are not well modeled by MC, resulting large uncertainties, are rejected. The resulting ratios for MC, as well as for data, are shown in Tables 5.27. Data-driven estimates are presented in Table 5.28.

	N_A/N_C [MC]	N_B/N_D [MC]	N_B/N_D [Data]
ee channel	0.017 ± 0.005	0.0137 ± 0.0004	0.0159 ± 0.0003
$\mu\mu$ channel	0.012 ± 0.003	0.0125 ± 0.0003	0.0145 ± 0.0002

Table 5.27: Ratios N_A/N_C, N_B/N_D for the ee- and $\mu\mu$-channel. Only the statistical errors shown. Statistical errors due to the MC subtraction are also considered for N_B/N_D (Data). WZ background yields for subtraction from data are rescaled using a scale factor of 1.29. For ZZ background, NNLO QCD & NLO EW corrections are applied. Sherpa 2.2.1 samples are used for the Z+jets background.

Channel	MC only	Data-driven
ee	35.04 ± 10.75 ± 14.50	30.45 ± 1.09 ± 27.57
$\mu\mu$	34.78 ± 7.48 ± 13.71	37.03 ± 1.21 ± 18.82

Table 5.28: Summary of the Z+jets background estimation using the "ABCD" method with statistical and systematic uncertainties. Systematic uncertainties come from the level of correlation in MC, estimated by difference between N_A/N_C (MC) and N_B/N_D (MC), experimental uncertainties on this difference and subtraction of non-Z+jets backgrounds.

To determine systematic uncertainties of the method, the difference between N_A/N_C (MC) and N_B/N_D (MC), which is representing correlation-induced bias in

MC (non-closure), is taken into account. The impact of the experimental uncertainties on this difference is also investigated. Experimental uncertainties on subtraction of non-Z+jets background are also included. Contribution of each source to the total systematic uncertainties is summarized in Table 5.29.

	ee-channel	$\mu\mu$-channel
Methodology	$^{+90.2\%}_{-54.5\%}$	$^{+37.2\%}_{-49.4\%}$
Non-Z+jets sub.	13.6%	11.2%
Total systematic unc.	$^{+91.3\%}_{-56.2\%}$	$^{+38.8\%}_{-50.6\%}$

Table 5.29: Systematic uncertainties sources combine methodology uncertainty and uncertainty on subtraction of non-Z+jets backgrounds from MC. Methodology uncertainty consists of correlation-induced bias $1-\frac{N_C * N_B}{N_D * N_A}$ including experimental uncertainties (dominated by JetGroupedNP_1&3 5.3.2.4) and uncertainty associated with selection of optimal additional $E_{\mathrm{T}}^{\mathrm{miss}}$and $E_{\mathrm{T}}^{\mathrm{miss}}/H_T$ cuts, estimated by varying the cuts by 40% from their nominal values; both of these sources having roughly equal contribution.

5.4.4.2 Single Side-band Method

The single side-band method is a simple and straightforward approach, constructing a single side-band by reversing one of the selection cuts to enhance the Z+jets events as schematically described in Figure 5.12, where the events in the signal region are estimated with Equation 5.12.

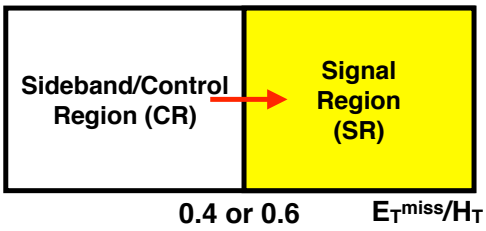

Figure 5.12: Scheme of the one side-band method. A selection is reversed to construct the side-band region.

$$N_{\mathrm{SR}}^{\mathrm{est}} = N_{\mathrm{CR}}^{\mathrm{data,sub}} \times \frac{N_{\mathrm{SR}}^{\mathrm{MC}}}{N_{\mathrm{CR}}^{\mathrm{MC}}} \tag{5.12}$$

The $E_{\mathrm{T}}^{\mathrm{miss}}/H_{\mathrm{T}}$ is considered to construct the side-band, since this variable provides a good separation between the Z+jets and other events with intrinsic $E_{\mathrm{T}}^{\mathrm{miss}}$, i.e. diboson, Top or signal events. However, the method also works with other variables in principle.

The pros of this method are the simplicity and the fact that the method does not suffer from non-trivial correlations between the various kinematic variables as is the case with the "ABCD" method. One drawback is the fact that it fully relies on the MC for the SR/CR ratio. The main systematic uncertainty comes from the prediction of this ratio. With the full selection applied, the purity of the Z+jets events in the side-band region is 67.7 ± 4.0% (73.9 ± 2.9%) for the ee ($\mu\mu$) channel.

Z+jets background estimation with the single side-band method is summarized in Table 5.30. The estimations have larger yields with the single side-band method than the MC expectation due to more data observed in the side-band region. The statistical uncertainties of $N_{\mathrm{SR}}^{\mathrm{MC}}/N_{\mathrm{CR}}^{\mathrm{MC}}$ are included in the statistical uncertainties of the estimation. Uncertainties on $N_{\mathrm{SR}}^{\mathrm{MC}}/N_{\mathrm{CR}}^{\mathrm{MC}}$ from JES, JER, and $E_{\mathrm{T}}^{\mathrm{miss}}$ soft-term experimental systematic uncertainties are 29% (55%) in the ee- ($\mu\mu$-) channel. The systematic uncertainties from the non-Z backgrounds is 7.4% (4.6%) in the ee- ($\mu\mu$-) channel.

Z+jets	ee-channel	$\mu\mu$-channel
Yields	37.7 ± 12.2 (stat) ± 23.5 (syst) [32.4 ± 10.1 (stat)]	41.8 ± 9.6 (stat) ± 21.4 (syst) [30.1 ± 6.7 (stat)]

Table 5.30: Estimated Z+jets background yields with the one side-band method. Numbers in brackets are from the MC expectation for comparison. Errors are shown for both statistical uncertainty and systematic uncertainty.

5.4.5 W+jets background

A contribution to the $\ell^+\ell^-$+$E_{\mathrm{T}}^{\mathrm{miss}}$ final state can arise from a misidentified lepton from a jet, when it is produced in association with a leptonically decaying W boson.

The rate at which hadronic jets are misidentified as leptons may not be accurately described in the simulation, because these events are produced due to rare fragmentation processes or interactions with the detector. This background is therefore estimated from data. Although this background is found to be negligible, it is still important to set up a methodology with a robust data-driven estimate of this fake-dominated background. Two different methods have been explored to estimate the W+jets contribution, the same-sign method and the fake-factor method. However, the estimation with the same-sign method is found to be contaminated by the

Z+jets, whose modeling is shown not to be well represented by MC. For this reason the estimation is done using the fake-factor method only.

5.4.5.1 Fake factor method

The fake-factor method is used to estimate the W+jets contribution in SR, by first evaluating the probability for a jet to be mis-identified as a lepton, and then by applying the fake factor to data events in a W+jets control sample.

The fake factor is measured by using control samples dominated by Z+jets where all the other components are subtracted using simulation (W+jets control samples are used for comparison). In the Z+jets control sampples, a di-lepton pair from Z boson decay is selected as a "tag". In addition to the "tag", it requires an extra electron or muon passing the full selection criteria (referred to as "good" lepton) and a lepton-like jet (referred to as "bad" lepton), which is a reconstructed electron or muon that is selected as likely to be faked from a jet. For electrons, the lepton-like jets are electron candidates that fail the requirements on isolation or likelihood ID. For muons, lepton-like jets are muon candidates that fail the requirement on isolation. These events are further required to pass the full event selection, treating the lepton-like jet as if it is a fully identified lepton. The W+jets background is then estimated by scaling this control sample by a measured p_{T}-dependent or η-dependent fake-factor. The fake-factor is the ratio of the probability for a jet to satisfy the full lepton identification criteria to the probability to satisfy the lepton-like jet criteria, as shown in Equation 5.13:

$$F.F. = N_{Good}^{fake}/N_{Bad}^{fake} \tag{5.13}$$

The following part describes the fake-factor determination and the W+jets control region definition for the background estimation. Before the data-driven estimate is performed, the robustness of the method is checked by evaluating the fake factor in two different jet-enriched MC samples, the W+jets and the Z+jets samples, and a consistency test between them is done.

5.4.5.2 MC consistency

For the consistency test, control samples dominated by W+jets and Z+jets events are used, where the other background components are subtracted using simulation. Details of the W+jets and the Z+jets samples are given below.

For W+jets MC: The fake factor is measured via a *Tag* and *Probe* method using W+jets events. The events are constructed by requiring one lepton as a tag passing the full selection criteria and then an additional "Good" lepton or "Bad" lepton as a probe. The "Good" lepton is defined in the same way as the lepton in the nominal analysis, but requiring the charge to be opposite to that of the W boson. The one that has same sign as the W boson is regarded to come from the W. The "Bad" lepton, which is our lepton-like jet, has the same selection as the nominal one but with one or two cuts that are reverted. For "Bad" electron, one can invert track isolation and medium working point, while for "Bad" muon, only invert track isolation cut. The definitions of "Good" and "Bad" leptons are summarized in Table 5.31. With these definitions one can select a sample of events which have a reconstructed lepton from $W^{\pm} \to l^{\pm} + \nu$ as the tag and then look for an additional lepton-object in the event that satisfies either the "Good" lepton or "Bad" lepton requirements, as the probe. The details of the "W-tagged" jet event selection can be found in Table 5.32.

For Z+jets MC: The "Good" lepton selection for the Z+jets sample is the same as the lepton selection in the nominal analysis. The "Bad" lepton selection has instead one or two cuts that are reverted. The definitions of "Good" and "Bad" leptons are summarized in Table 5.31. Then select a sample of events which have a reconstructed $Z \to l^{+}l^{-}$ as the tag and then look for an additional lepton-object in the event that satisfies either the "Good" lepton or "Bad" lepton requirements, as the probe. The details of the "Z-tagged" jet event selection can be found in Table 5.33.

For the final data-driven estimate, the fake factor is instead estimated from data. In this case the same selection used in the Z+jets MC sample above is applied on data. Subtracting the contribution from ZZ and WZ processes using MC, the remaining part can be regarded as coming from Z+jets. The fake-factor comparison among Z+jets MC, W+jets MC and data-driven is shown in Figure 5.13 for the ee channel and in Figure 5.14 for the $\mu\mu$ channel.

Difference of MC-based fake factor between W+jets and Z+jets samples, the "MC inconsistency", is used as a systematic uncertainty for the data-driven estimate, along with uncertainties associated with subtraction of non-W+jets backgrounds from MC.

	Good (G)	Bad (B)
Electrons	Track iso: Loose and lh: Medium	Track iso: !Loose or lh: !Medium
Muons	Track iso: Loose	Track iso: !Loose

Table 5.31: Summary of requirements for "Good" and "Bad" leptons

Criteria	Selection
Tag lepton	1 selected Muon or Electrons
Probe lepton	only one extra lepton
Trigger	Single lepton trigger
$E_{\mathrm{T}}^{\mathrm{miss}}$	$>$ 20 GeV

Table 5.32: Summary of the requirements used to select a control sample from W+jets MC for fake factor measurement.

Criteria	Selection
Leptons	2 selected Muons or 2 selected Electrons
Trigger	Single lepton trigger
Z-reconstruction	oppositely charged leptons
	$\lvert M_{ll} - M_Z \rvert$ <15 GeV
Probe lepton	only one extra lepton

Table 5.33: Summary of the requirements used to select a control sample from Z+jets MC for fake factor measurement.

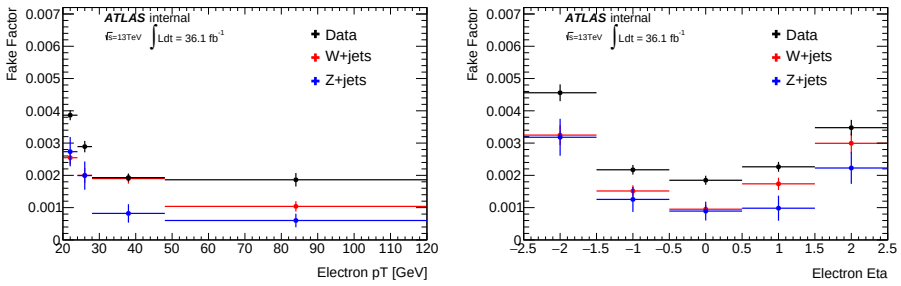

(a) (b)

Figure 5.13: (a) Fake factor as measured in data, W+jets, and Z+jets MC samples with regarding to lepton p_{T}(a), η (b) in ee channel

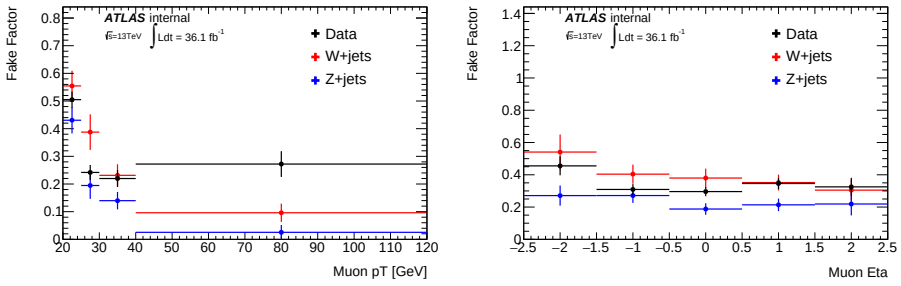

(a) (b)

Figure 5.14: (a) Fake factor as measured in data, W+jets and Z+jets MC samples with regarding to lepton p_{T}(a), η (b) in $\mu\mu$ channel.

5.4.5.3 W+jets background estimation

For the final estimation, the W+jets control region is defined by requiring the presence of one "Good" lepton and one "Bad" lepton with same flavor, both passing the nominal selection criteria. The fake factor is then applied to the event with regarding to bad lepton η. For the events selected from data, we subtract the contribution of WW, WZ, ZZ and $t\bar{t}$ (normalized to current luminosity: 36.1 fb^{-1}). The final W+jets contributions to SR are summarized in Table 5.34.

	Data-driven yields
ee	$0.43 \pm 0.09 \pm 0.04$
$\mu\mu$	$1.53 \pm 1.92 \pm 0.73$

Table 5.34: W+jets estimation in the electron and muon channel as obtained from the "fake factor" data-driven technique. The systematic uncertainties are calculated as the differences between the W+jets and Z+jets MC-based fake-factors, as well as uncertainty associated with subtraction of non-W+jets backgrounds from MC.

5.4.6 Other Backgrounds

Other backgrounds including $t\bar{t}V/VVV$ make minor contribution to the contamination. Such small backgrounds are estimated based on MC prediction for both yields and shapes. The yields in final SR are $0.96 \pm 0.04 \pm 0.08$ for ee channel and $0.96 \pm 0.03 \pm 0.10$ for $\mu\mu$ channel.

5.4.7 Systematic Uncertainty

In general, uncertainties that can impact the analysis come from event reconstruction, theory calculation, data-driven estimation of backgrounds as well as luminosity determination. For the signal process, reconstruction and theory uncertainties both play a role in the determination of the $E_{\mathrm{T}}^{\mathrm{miss}}$ shape as well as acceptance. Theory part is described in Section 5.3.2.4 while reconstruction uncertainties are introduced below. For MC-based backgrounds, both yield and shape can be affected by reconstruction and theory uncertainties as well as the luminosity uncertainty. For backgrounds estimated with data, the yield and shape are fully determined in data, while for the WZ background the predicted yield is determined from data and the $E_{\mathrm{T}}^{\mathrm{miss}}$ shape comes from MC. Table 5.35 summarizes the implementation of various types of uncertainties on the physics processes involved in this analysis.

The following sections will briefly discuss the experimental and theoretical uncertainties concerned in this analysis and for simplicity the uncertainties are demonstrated as their impact on the predicted yields of given processes.

Process	Lumi.	Reconstruction	Data-Driven	Theory
Signal	Yield	Yield, Shape	-	Yield
ZZ	Yield	Yield, Shape	-	Yield, Shape
WZ	-	Shape	Yield	Shape
$Z+$jets	-	Shape	Yield	-
$top/WW/Z\tau\tau$	-	Shape	Yield	-
$W+$jets	-	Shape	Yield	-
ttV/VVV	Yield	-	-	Yield, Shape

Table 5.35: Impact of various uncertainty sources on the physics processes involved in this analysis. For processes labeled with "Yield," the number of events in the signal region is affected (.e.g by uncertainties on the luminosity). For processes labeled with "Acceptance," (e.g. the signal), the cross section is unknown and so the uncertainties will affect the acceptance but not the yield.

5.4.7.1 Theoretical Uncertainty

The theoretical uncertainties involved in background estimation are mainly for ZZ and WZ processes. The $q\bar{q} \to ZZ$ background (modeled with Powheg + Pythia8) has been normalized to NNLO total cross section using mass-binned k-factors (approximately 10% in average), and the theoretical uncertainty is considered using the MC samples which are at NLO+PS precision. The PDF and scale uncertainties on the expected yields are evaluated using MC truth events produced with the nominal Powheg generator showered with official Pythia8 release, and found quite constant along the $E_{\mathrm{T}}^{\mathrm{miss}}$ and m_T distribution. The typical sizes of PDF and QCD scale uncertainties are about 2.4% and 3.6%, respectively. The theoretical shape uncertainty (PDF and QCD scales) is found to be insignificant (up to 0.5%). In addition, the effect of parton-shower choices are studied by comparing Powheg truth events showered with Pythia8 and *Herwig*, the difference is found to be less than 0.1% and flat across the mass spectrum. In addition, the NLO electroweak correction is applied to the $q\bar{q} \to ZZ$ process, and the averaged effects on $q\bar{q} \to ZZ$ yield is about 10%. The k-factors are applied to the central value and results are shown in Figure 5.15.

The non-resonant $gg \to ZZ$ process (modeled with $gg2VV$ + Pythia8) is a subprocess of the total ZZ production process and it enters formally at α_s^2. The $gg \to ZZ$

predicted has been calculated to its relative next-to-leading order and we apply a constant k-factor of 1.7 ± 1.0 to the MC prediction that is at the LO. This relative 60% uncertainty on the $gg \to ZZ$ prediction is applied in the $E_{\mathrm{T}}^{\mathrm{miss}}$ distribution.

The WZ background is estimated partially based on data, i.e. the normalization comes from data, while its shape is predicted by MC. Therefore, the shape uncertainty is evaluated for the WZ background and considered in the limit setting. The theoretical shape uncertainty (PDF and QCD scales) is also found to be negligible (up to 0.5%) and total results are shown in Figure 5.16,

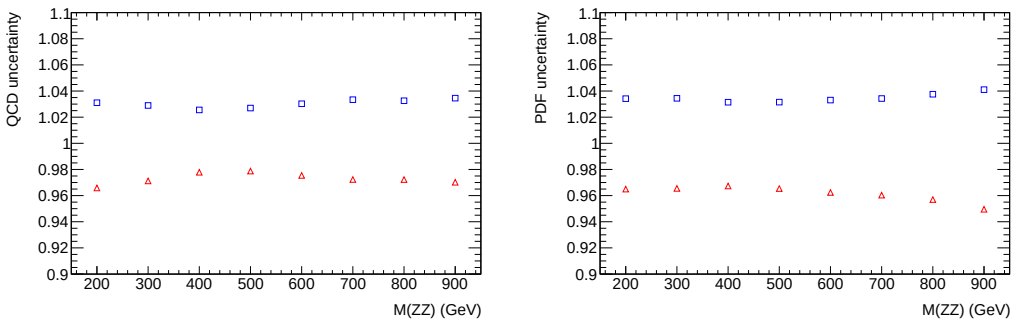

Figure 5.15: Theoretical systematic uncertainties on ZZ background due to QCD scale and PDF variation, as a function of the transverse mass of the ZZ resonance.

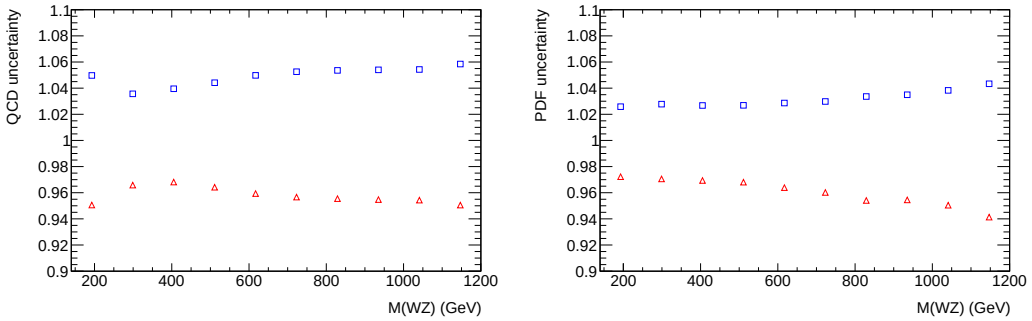

Figure 5.16: QCD and PDF scale included shape uncertainties as a function of the mass of the WZ resonance.

5.5 Results

5.5.1 Data Comparison with Predicted Background and Signal

Table 5.36 gives the observed data yields, the estimated background contributions, and the expectation for the signal processes after the final selection. The $E_{\mathrm{T}}^{\mathrm{miss}}$ dis-

tributions after applying full event selections and with signals overlaid are shown in Figure 5.17.

	ee	$\mu\mu$
Data	437	497
Zhinv ($m_h = 125\,\text{GeV}$, MC)	107.79 ± 2.02 ± 9.39	113.91 ± 2.29 ± 7.54
$qqZZ$ (MC)	212.08 ± 2.94 ± 15.39	220.69 ± 2.94 ± 16.94
$ggZZ$ (MC)	18.89 ± 0.32 ± 11.18	19.25 ± 0.32 ± 11.41
WZ (Data-Driven)	106.28 ± 2.47 ± 6.12	113.40 ± 2.64 ± 5.39
Z+jets (Data-Driven)	30.45 ± 1.09 ± 27.57	37.03 ± 1.21 ± 18.82
$Z\tau\tau$/top/WW/Wt (Data-Driven)	29.47 ± 3.79 ± 1.58	33.22 ± 4.27 ± 1.62
W+jets (Data-Driven)	0.43 ± 0.09 ± 0.05	1.53 ± 1.92 ± 0.82
Others (MC)	0.96 ± 0.04 ± 0.08	0.96 ± 0.03 ± 0.10
Total Bkg.	398.56 ± 5.51 ± 34.09	426.08 ± 6.24 ± 28.35

Table 5.36: The observed data and expected yields in ee and $\mu\mu$ SRs after full event selections for 36.1 fb^{-1}. Estimates include statistical and systematic errors given where available in both MC and data-driven estimations. The data-driven estimation on WZ has a significant impact on total background yields. The statistical and systematic errors on the total background prediction are summed quadratically from each individual process. The "Others" category is composed of ttV and VVV backgrounds.

5.5.2 Likelihood definition

As shown in Figure 5.17, data is observed to agree with the SM background prediction well, which means no obvious signal of $h \to inv.$. Therefore, an upper limit is set on BR($h \to$ inv.). The statistical analysis of the data uses a binned likelihood function constructed as the product of Poisson probability terms,

$$\text{Pois}(n|\mu S + B) \left[\prod_{b \in \text{bins}} \left(\frac{\mu \nu_b^{\text{sig}} + \nu_b^{\text{bkg}}}{\mu S + B} \right)^{n_b} \right], \tag{5.14}$$

where μ, a signal strength parameter, multiplies the expected signal yield ν_b^{sig} in each histogram bin b, and ν_b^{bkg} represents the background content for bin b. n_b is the oberserved data events in bin b. The dependence of the signal and background predictions on the systematic uncertainties is described by a set of nuisance parameters (NP) θ, which are parametrized by Gaussian priors; the latter are used for normaliza-

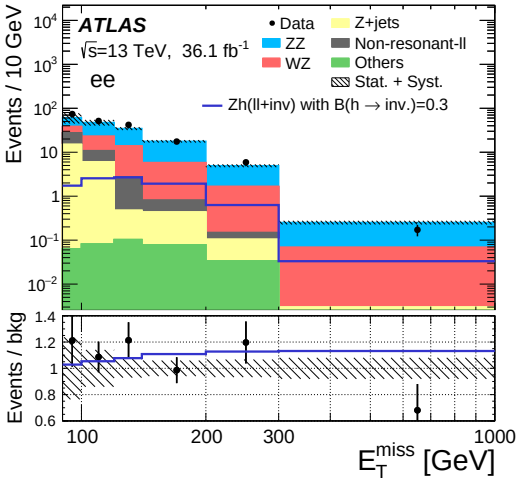

(a)

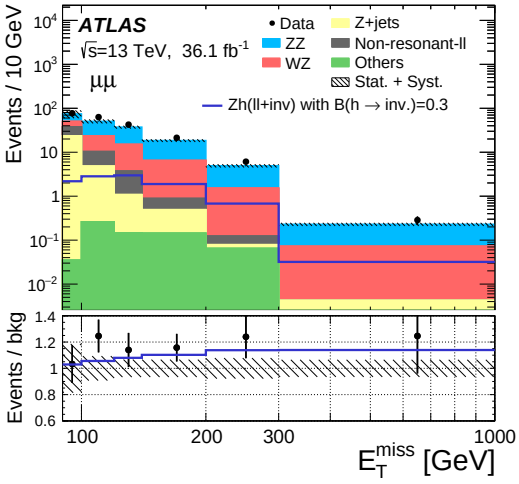

(b)

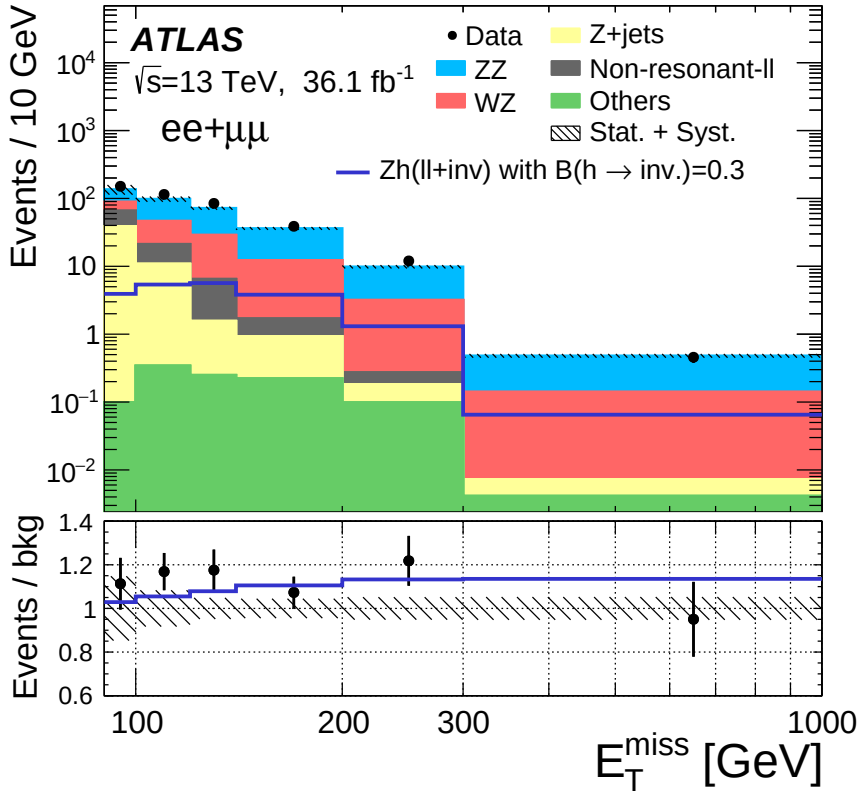

(c)

Figure 5.17: The $E_{\mathrm{T}}^{\mathrm{miss}}$ distribution after final selections in the (a) ee channel, (b) $\mu\mu$ channel, and (c) $ee + \mu\mu$ combined channel. The yields of WZ, $Top/WW/Z \to \tau\tau$ (Non-resonant-ll) and $Z \to ee/Z \to \mu\mu$ backgrounds are estimated using data-driven method and the $E_{\mathrm{T}}^{\mathrm{miss}}$ shapes for these backgrounds are derived from MC samples. The ZZ backgrounds are fully estimated from theoretical predictions and higher order corrections are applied. Both statistical and systematic uncertainties are included in the uncertainties bands, and they are summed quadratically.

tion uncertainties in order to maintain a positive likelihood. The expected numbers of signal and background events in each bin are functions of θ and μ (in the case of signal process).

The priors act to constrain the NPs to their nominal values within their assigned uncertainties. They are implemented via so-called penalty or auxiliary measurements added to the likelihood which will always increase when any nuisance parameter is shifted from the nominal value. The likelihood function, $\mathcal{L}(\mu, \theta)$, is therefore a function of μ and θ.

The nominal fit result in terms of μ and σ_μ is obtained by maximizing the likelihood function with respect to all parameters. This is referred to as the maximized log-likelihood value, MLL. The best statistic q_μ is then constructed according to the profile likelihood: $q_\mu = -2\ln(\mathcal{L}(\mu, \hat{\hat{\theta}})/\mathcal{L}(\hat{\mu}, \hat{\theta}))$, where $\hat{\mu}$ and $\hat{\theta}$ are the parameters that maximize the likelihood (with the constraint $0 \leq \hat{\mu} \leq \mu$), and $\hat{\hat{\theta}}$ are the nuisance parameter values that maximize the likelihood for a given μ.

The compatibility (p-value) between data and the assumed signal+background model with μ is tested using $\tilde{q}_\mu$. The corresponding p-value, p_μ, is defined as:

$$p_\mu = \int_{\tilde{q}_{\mu,\text{obs}}}^{\infty} f(\tilde{q}_\mu|\mu)\mathrm{d}\tilde{q}_\mu \tag{5.15}$$

Here $f(\tilde{q}_\mu|\mu)$ is the probability density function of $\tilde{q}_\mu$ assuming the μ hypothesis, and $\tilde{q}_{\mu,\text{obs}}$ is the value of $\tilde{q}_\mu$ computed for the observed data. The asymptotic formula [111], widely used in ATLAS statistical analyses, are used to calculate the closed form for $f(\tilde{q}_\mu|\mu)$. p_μ can also be written as:

$$p_\mu \equiv p_{s+b} = P(\tilde{q}_\mu \geq \tilde{q}_{\mu,\text{obs}}|s+b) \tag{5.16}$$

Performing exclusion tests with p_{s+b} is known as the CL_{s+b} method. This analysis uses the CL_s method, where the p-value, or the "CL_s value," is defined as:

$$\text{CL}_s \equiv \frac{p_{s+b}}{1-p_b}, \tag{5.17}$$

where

$$p_b = P(\tilde{q}_\mu \leq \tilde{q}_{\mu,\text{obs}}|b). \tag{5.18}$$

For the $Zh \to \ell\ell + \text{invisible}$ signal, any μ values that give $\text{CL}_s < 0.05$ are excluded at the 95% CL. The observed limit can be compared with the expected limit derived using an Asimov dataset treated as the $E_{\text{T}}^{\text{miss}}$ distribution after profiling the

background-only model (μ=0) to data. In this case, the $\pm1\sigma$ and $\pm2\sigma$ bands on the expected limits can also be reported to test the compatibility between observed and expected limits. The limits on BR($h \to$ inv.) is exact the limits on μ. The corresponding limits on $\sigma(Zh \to \ell\ell + inv.)$ production cross section are calculated based on the limits on μ and the theoretical cross section for different models.

5.5.3 Limits

Assuming the Higgs boson is produced in both the $qq \to ZH$ and $gg \to ZH$ processes, the upper limit on BR($h \to$ inv.) can be derived using the SM cross section and branching ratio: $\sigma(qq \to ZH) \times BR(Z \to \ell\ell, \ell = e, \mu, \tau) = 76.89$ fb and $\sigma(gg \to ZH) \times BR(Z \to \ell\ell, \ell = e, \mu, \tau) = 12.42$ fb. Limits on BR($h \to$ inv.) are shown in Tables 5.37 and 5.38. Table 5.37 shows the limit results using only statistical uncertainties in the fit. Table 5.38 presents the limits using statistical and systematic uncertainties. With the full statistical and systematic treatment, the observed upper limit on BR($h \to$ inv.) is 66.8%, with an expected value of 38.8%. A CL scan is performed with BR($h \to$ inv.) varying from 0 to 1.0, and the results are shown in Figure 5.18.

Mass points	Exp. limit	Exp. $+2\sigma$	Exp. $+1\sigma$	Exp. -1σ	Exp. -2σ	Obs. limit
			Combined			
125 GeV	0.240	0.457	0.337	0.1701	0.127	0.579
			ee			
125 GeV	0.347	0.668	0.490	0.248	0.183	0.539
			$\mu\mu$			
125 GeV	0.338	0.652	0.478	0.242	0.179	0.891

Table 5.37: The 95% CL upper limits on BR($h \to$ inv.) for ee, $\mu\mu$, and ee+$\mu\mu$ channel fits. Both observed and expected limits are presented as well as the $\pm1\sigma$ and $\pm2\sigma$ error bands on the expected limit. Only statistical uncertainties are included in the fit.

In order to check the effects of systematic uncertainties from different sources on BR($h \to$ inv.), we break down the systematic uncertainties into several independent groups and repeat the limit setting by including each group exclusively as well as statistical uncertainties. The relative differences with respect to the nominal limit (computed without systematic uncertainties) are treated as the systematic uncertainty impact on the limit for a certain group. These results are summarized in Table 5.39 for both the observed and expected limits. Inclusion of pileup and

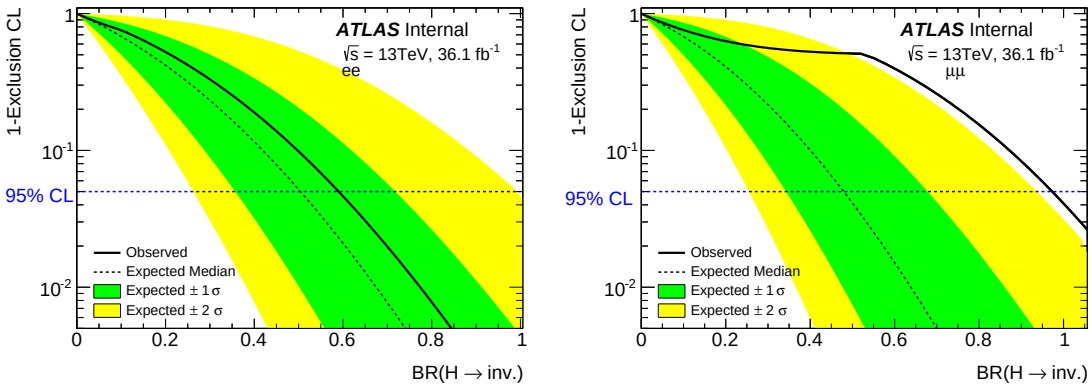

(a)

(b)

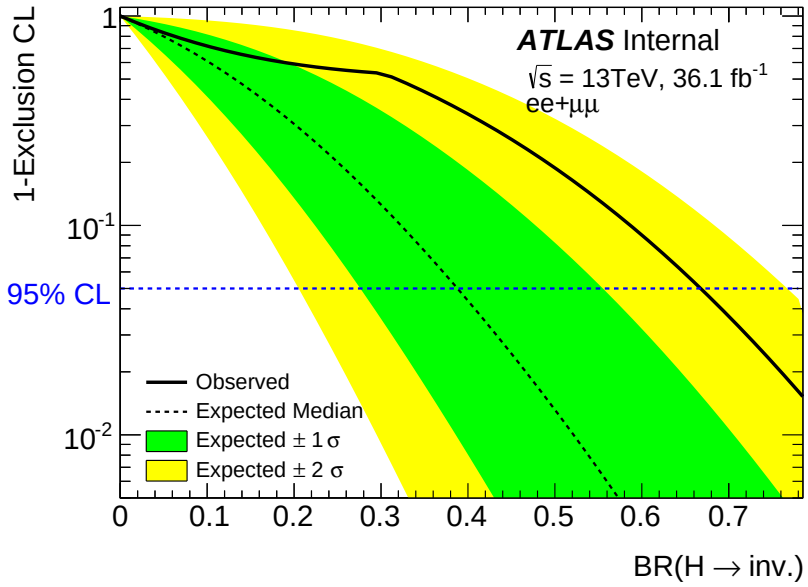

(c)

Figure 5.18: The CL scan as function of BR($h \to$ inv.) for $Zh \to \ell\ell +$ invisible with $m_{\mathrm{h}} = 125\,\mathrm{GeV}$. Plots (a) and (b) are the ee and $\mu\mu$ channel results, and plot (c) is the $ee + \mu\mu$ combined channel results. The observed and expected curves are shown with solid and dashed lines. Signal is scaled to the SM cross section value times the best-fit μ value 0.3. The $\pm 1\sigma$ and $\pm 2\sigma$ bands are shown as yellow and green bands respectively. The crossing point between 95% CL line solid (dashed) line gives the observed (expected) upper limit on BR($h \to$ inv.).

Mass points	Exp. limit	Exp. $+2\sigma$	Exp. $+1\sigma$	Exp. -1σ	Exp. -2σ	Obs. limit
			Combined			
125 GeV	0.388	0.768	0.555	0.276	0.206	0.668
			ee			
125 GeV	0.505	0.994	0.718	0.357	0.263	0.591
			$\mu\mu$			
125 GeV	0.480	0.938	0.679	0.344	0.256	0.974

Table 5.38: The 95% CL upper limits on BR($h \to$ inv.) for ee, $\mu\mu$, and ee+$\mu\mu$ channel fits. Both observed and expected limits are presented as well as the $\pm1\sigma$ and $\pm2\sigma$ error bands on the expected limit. No significant excess is seen in all channels, and the observed and expected limits are compatible within the error bands. *Both statistical and systematic uncertainties are included in the fit.*

Z+jets uncertainties makes the observed limit better than that from the stat-only case, and that is due to that fact there is a slight data excess over the SM expectation in the low $E_{\mathrm{T}}^{\mathrm{miss}}$ bins. The nuisance parameters responsible for Z+jets and pileup uncertainties are pulled during the fit to reduce the excess.

Category	Change in expected $BR(H \to inv.)$ (%)	Change in observed $BR(H \to inv.)$ (%)
electron	1.46	2.09
muon	1.00	0.27
jet	4.34	0.75
$E_{\mathrm{T}}^{\mathrm{miss}}$	0.09	0.06
luminosity	11.44	8.22
pileup	0.14	-1.01
WZ	9.36	4.05
$qq \to ZZ$	19.55	7.26
$gg \to ZZ$	58.07	13.98
Z+jets	5.54	-0.93
bkg MC statistics	1.77	0.84
signal MC statistics	0.02	0.11

Table 5.39: The systematic uncertainty impact on the expected and observed limits for BR($h \to$ inv.) (relative errors). The systematic uncertainties are grouped into different categories. For each repetition of the limit setting, one group is added on top of the stat-only configuration. The difference w.r.t. to the stat-only limit is then taken as the systematic uncertainty impact.

In addition to the limits on the invisible decay branching fraction of h with the mass of $m_h = 125$ GeV, limits on $\sigma(pp \to Zh \to \ell\ell + inv.)$ are also calculated as a

function various non-SM values of m_h. Table 5.40 presents the cross section limits for m_h from 110-400 GeV as obtained from the combined $ee + \mu\mu$ fit. Observed limits range from 4.70 fb for $m_h = 400$ GeV to 136.82 fb for $m_h = 110$ GeV. Figure 5.19 shows the 95% CL limit as a function of m_h. The observed limits are compatible with the expected limits.

Mass points	Exp. Limits [fb]	Exp. $+2\sigma$	Exp. $+1\sigma$	Exp. -1σ	Exp. -2σ	Obs. Limits
110.0 GeV	78.42	153.03	111.67	55.98	41.62	136.82
120.0 GeV	27.80	54.14	39.56	19.85	14.76	46.78
125.0 GeV	25.83	50.32	36.77	18.46	13.73	44.58
130.0 GeV	23.61	45.98	33.59	16.86	12.53	39.26
140.0 GeV	20.12	39.24	28.63	14.37	10.68	33.01
150.0 GeV	18.17	35.53	25.87	12.97	9.62	29.77
200.0 GeV	9.98	19.64	14.21	7.10	5.27	14.54
250.0 GeV	7.03	13.88	10.01	4.99	3.69	9.33
300.0 GeV	5.22	10.36	7.46	3.70	2.73	6.60
400.0 GeV	4.09	8.16	5.86	2.89	2.13	4.70

Table 5.40: The 95% CL upper limits on $\sigma(pp \to Zh \to \ell\ell + inv.)$ for various values of m_H as obtained from the combined $ee+\mu\mu$ channels. Both observed and expected limits are given, as well as $\pm 1\sigma$ and $\pm 2\sigma$ error bands on the expected limits. No significant excess is seen in all channels, and the observed and expected limits are compatible within the error bands. Full statistical and systematic uncertainties are included in the fit.

5.5.4 Short Summary

No significant deviation from the SM prediction is observed. Assuming the Standard Model ZH production cross-section, an observed upper limit of 67% at 95% confidence level (CL) is set on the branching ratio of invisible decays of the Higgs boson with mass $m_h = 125$ GeV. The corresponding limits on the production cross-section (σ) of the BSM Zh process with the invisible Higgs boson decay are also presented in the mass between 110 GeV and 400 GeV.

5.5.5 Discussion on DM Searches

5.5.5.1 Compare to search for invisible Higgs boson decay with VBF Higgs productions

The invisible Higgs boson decay is also searched in VBF Higgs production mode in ATLAS. Instead of di-lepton from Z boson decay as a tag, two forward jets with large p_T (> 60 GeV) are used as the tag in VBF process.

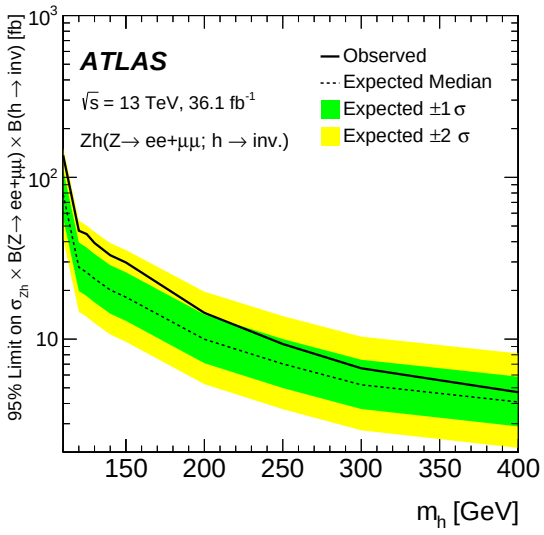

Figure 5.19: The 95% CL upper limits on $\sigma(pp \to Zh \to \ell\ell + inv.)$ as a function of m_H, as obtained from the combined ee+$\mu\mu$ channels. Observed and expected limits are given, as well as $\pm 1\sigma$ and $\pm 2\sigma$ error bands on the expected limit. No significant excess is seen in all channels, and the observed and expected limits are compatible within the error bands. Full statistical and systematic uncertainties are included in the fit.

The Higgs boson VBF production cross section is 3.8 pb at center-of-mass energy of 13 TeV, which is significantly higher than the ZH production cross section times BR($Z \to \ell\ell$), 0.08 pb. However, the event tag (forward jets) in VBF process has large systematic uncertainty in both modeling and measurement. The expected limit in ATLAS Run II (36.1 fb^{-1}data) is 33% for invisible Higgs decay in VBF production mode, which is compatible with the search sensitivity in ATLAS Run I with the luminosity of 20.3 fb^{-1}. The systematic uncertainties dominate this channel.

For the search of invisible Higgs decay produced in association with a Z boson, the signal from $Z \to \ell\ell$ is robust to high lumionosity and pile-up experimental conditions. The search in this mode, the statistical error still dominates. The current expected limit is 39% with 36.1 fb^{-1} data. By the end of Run II, the total data size will increase by a factor of ≈ 3.9 and the expected limit will be suppressed to 20%, which looks more prosmising than the search with the Higgs VBF production mode.

5.5.5.2 Comparisons with the underground direct DM search experiments

The direct detection experiments typically operate in deep underground laboratories to reduce the background from cosmic rays. Experiments can be sensitive to both nuclear spin-independent (SI) interactions and spin-dependent (SD) interactions. Example of the direct detection experiments are: **XENON** [112], **COUPP** [113], and **CDMS** [114]. Figure 5.20 [115] shows the current SI landscape, where strict upper limits exist for higher mass WIMPs. It is possible to relate the invisible Higgs branch-

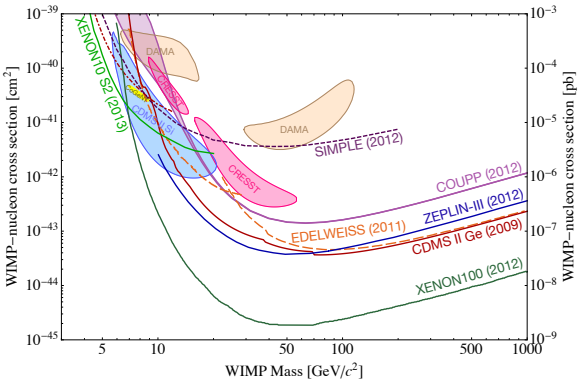

Figure 5.20: Spin-independent WIMP-nucleon cross section limits vs WIMP mass as of summer 2013 [115].

ing fraction to the direct detection cross section. Both partial Higgs decay width into dark matter $\Gamma(h \to \chi\chi)$ and the SI χ-proton elastic cross section $\sigma^{\rm SI}_{\chi p}$ are proportional to $\lambda^2_{h\chi\chi}$; therefore, the ratio $\Gamma(h \to \chi\chi)/\sigma^{\rm SI}_{\chi p}$ depends only on the dark matter mass M_χ and known masses and couplings [116]. By the end of LHC Run II, the expected limit of Higgs invisible decay will be 20%, which implies a limit on the direct detection cross section that is stronger than the current bounds from XENON100, as shown in the Figure 5.21. Hence, in the context of Higgs-portal model, the LHC is currently the most sensitive dark matter detection apparatus.

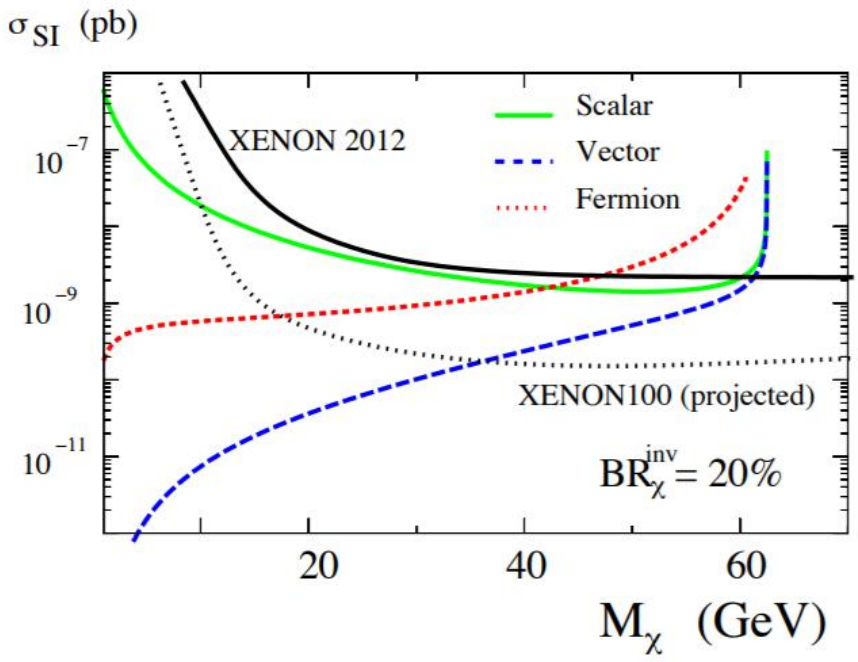

Figure 5.21: Bounds on the spin-independent direct detection cross section $\sigma^{\rm SI}_{\chi p}$ in Higgs portal models derived for $m_h = 125$ GeV and the invisible branching fraction of 20% (colord lines). For comparison, the current and future direct bounds from the XENON experiments are plotted (black lines) [116].

CHAPTER VI

Search For New Resonances in High Mass Scale

This chapter presents the search for heavy resonances decaying into a pair of Z bosons leading to $\ell^+\ell^-\nu\bar{\nu}$ final state using the full 2015 and 2016 dataset collected by the ATLAS detector in 13 TeV pp collisions. Different mass ranges for the hypothetical resonances are considered, depending on the model.

6.1 Introduction

This section introduces the search for a new heavy resonance (X) in the $X \to ZZ \to \ell\ell\nu\nu$ process. X represents an additional heavy Higgs boson (H) or a bulk RS graviton (G^*). The Feynman diagram is shown in Figure 6.1.

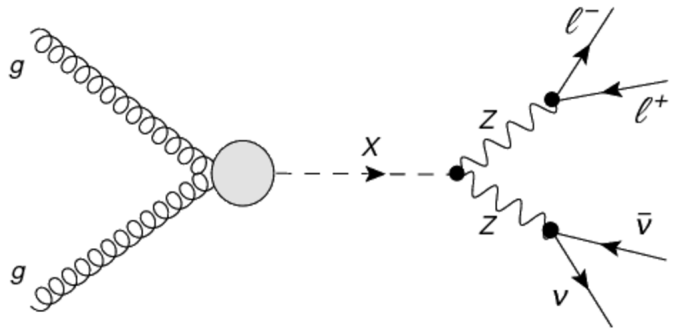

Figure 6.1: Feynman diagram for new heavy resonance produced in gluon-gluon fusion and decay to dilepton + $E_{\mathrm{T}}^{\mathrm{miss}}$ final state. X represents an additional heavy Higgs boson (H) or a bulk RS graviton (G^*).

The transverse mass of the dilepton and $E_{\mathrm{T}}^{\mathrm{miss}}$ system, m_T^{ZZ}, is used to discriminate between the high mass Higgs boson and the SM prediction. The transverse mass is defined as follows:

$$m_{\mathrm{T}}^2 \equiv \left[\sqrt{m_Z^2 + |\vec{P}_T^{ll}|^2} + \sqrt{m_Z^2 + |\vec{P}_T^{miss}|^2}\right]^2 - \left[\vec{P}_T^{ll} + \vec{P}_T^{miss}\right]^2. \quad (6.1)$$

The irreducible background originating from non-resonant ZZ production predicted by the SM is the major background in regions sensitive to the search. The Drell-Yan process contributes largely at lower mass than signal region due to large production cross section and possibility of jets faking $E_{\mathrm{T}}^{\mathrm{miss}}$. Other backgrounds including WZ, WW, top processes also contribute to the signal region due to their capability of decaying to or faking $\ell^+\ell^-\nu\bar{\nu}$ final states. Details about background estimation are introduced in Section 5.4.

The observed m_T distribution is compared to SM prediction for events satisfying the full kinematic selections. In the case no obvious deviation from the SM is observed, 95% C.L. upper limits on the production cross sections of additional heavy Higgs bosons are derived as a function of the pole mass of the new particles. In addition, the m_T distribution is also used to set upper limit on the production cross section of the graviton candidate (G^*) predicted by the bulk RS model.

6.2 Data and MC Samples

6.2.1 Data Sample

The data used in this search is exactly same as the one used in search for dark matter, as described in Section 6.2.1

6.2.2 Monte Carlo Samples

6.2.2.1 Heavy Higgs and RS Graviton signal samples

The heavy Higgs boson produced through gluon-gluon fusion and its subsequent decay to the $\ell\ell\nu\nu$ final state is modeled with POWHEG + PYTHIA8 using CT10 PDF set. The MC samples, as listed in Table 6.1 are generated using the narrow width approximation (NWA) for various Higgs pole masses ranging from 300 GeV to 1400 GeV. The provided cross sections of heavy Higgs production with different masses are calculated at the NLO in α_S with the POWHEG generator assuming a Standard Model Higgs Boson at that mass.

A bulk Randall-Sundrum (RS) Graviton sample, featuring a spin-2 graviton (G^*) is produced with the MadGraph generator and showered with PYTHIA8, using the A14 tune and the NNPDF23LO PDF set. The MC samples with mass from 600 GeV

Process	Generators	PDF	Events	Filter eff.	Cross section
ggH300NW	Powheg + Pythia8	CT10	99600	0.44477	6.646 pb
ggH400NW	Powheg + Pythia8	CT10	100000	0.44411	6.356 pb
ggH500NW	Powheg + Pythia8	CT10	100000	0.44467	3.077 pb
ggH600NW	Powheg + Pythia8	CT10	98000	0.44463	1.376 pb
ggH700NW	Powheg + Pythia8	CT10	100000	0.44610	640.57 fb
ggH750NW	Powheg + Pythia8	CT10	99000	0.44517	446.36 fb
ggH800NW	Powheg + Pythia8	CT10	99800	0.44549	315.39 fb
ggH900NW	Powheg + Pythia8	CT10	100000	0.44543	163.61 fb
ggH1000NW	Powheg + Pythia8	CT10	99600	0.44499	88.953 fb
ggH1200NW	Powheg + Pythia8	CT10	100000	0.44598	26.437 fb
ggH1400NW	Powheg + Pythia8	CT10	100000	0.44521	9.546 fb
ggH1600NW	Powheg + Pythia8	CT10	99800	0.44448	3.778 fb

Table 6.1: Summary of the heavy Higgs signal samples. The cross sections are for Standard Model Higgs Boson of corresponding masses

.

to 2 TeV are listed in Table 6.2 below.

Process	Generators	PDF	Events	Filter eff.	Cross section
RS_G_ZZ_llvv_c10_m0600	MadGraphPythia8	NNPDF23LO	30000	1	31.41 pb
RS_G_ZZ_llvv_c10_m0700	MadGraphPythia8	NNPDF23LO	30000	1	12.76 pb
RS_G_ZZ_llvv_c10_m0750	MadGraphPythia8	NNPDF23LO	30000	1	8.568 pb
RS_G_ZZ_llvv_c10_m0800	MadGraphPythia8	NNPDF23LO	30000	1	5.915 pb
RS_G_ZZ_llvv_c10_m0900	MadGraphPythia8	NNPDF23LO	30000	1	3.012 pb
RS_G_ZZ_llvv_c10_m1000	MadGraphPythia8	NNPDF23LO	28000	1	1.644 pb
RS_G_ZZ_llvv_c10_m1200	MadGraphPythia8	NNPDF23LO	30000	1	0.568 pb
RS_G_ZZ_llvv_c10_m1400	MadGraphPythia8	NNPDF23LO	30000	1	0.225 pb
RS_G_ZZ_llvv_c10_m1600	MadGraphPythia8	NNPDF23LO	30000	1	0.098 pb
RS_G_ZZ_llvv_c10_m1800	MadGraphPythia8	NNPDF23LO	29000	1	0.046 pb
RS_G_ZZ_llvv_c10_m2000	MadGraphPythia8	NNPDF23LO	30000	1	0.022 pb

Table 6.2: Summary of the RS graviton samples used in this analysis.

6.2.2.2 Background samples

Background MC samples are same as the ones used in dark matter search, as described in Section 5.2.2.2.

6.3 Event Selection

The object selection and event pre-selection are same as the requirements described in Section 5.3.1 and 5.3.2.2, respectively.

6.3.1 Final Event Selection

The Final event selections are similar but not identical to the cuts used in dark matter search. For example the $E_{\mathrm{T}}^{\mathrm{miss}}$ cut is required to be larger than 120 GeV. The minimal space angle $\Delta\phi$ between $E_{\mathrm{T}}^{\mathrm{miss}}$ and any jet with $p_T > 100$ GeV should be larger than 0.4.

The following Table 6.3 lists the details about each cut used in this analysis.

Criterion
$\lvert m_Z - m_{\ell\ell}\rvert < 15$ GeV
$E_T^{\mathrm{miss}} > 120$ GeV
$\Delta R_{\ell\ell} < 1.8$
$\Delta\phi(p_T^Z, E_T^{\mathrm{miss}}) > 2.7$
Fractional p_T difference < 0.2
$\min(\Delta\phi(jet, E_T^{\mathrm{miss}})) > 0.4$, (jet $p_{\mathrm{T}} > 100$ GeV)
$E_{\mathrm{T}}^{\mathrm{miss}}/H_T > 0.4$
$\mathrm{n_{b\text{-}jets}} = 0$, (jet $p_{\mathrm{T}} > 20$ GeV, b-tagging WP 85%)

Table 6.3: Summary of the event selection for the high mass resonance search.

6.3.2 Kinematic Distributions

This section shows various kinematic distributions related to the cuts listed in Section 6.3.1. When showing each variable, all the previous used variable cuts are applied. Here is the list of what is shown in each plot:

- Figure 6.2 contains the $E_{\mathrm{T}}^{\mathrm{miss}}$ distribution after applying all analysis cuts up through the di-lepton invariant mass cut.
- Figure 6.3 contains the ΔR distribution after applying all analysis cuts up through the E_T^{miss} cut.
- Figure 6.4 contains the $\Delta\phi(Z, E_{\mathrm{T}}^{\mathrm{miss}})$ distribution after applying all analysis cuts up through the ΔR cut.

- Figure 6.5 contains the fractional p_{T} difference distribution after applying all analysis cuts up through the $\Delta\phi$ cut.
- Figure 6.6 contains the $min(\Delta\phi(j, E_{\mathrm{T}}^{\mathrm{miss}}))$ distribution after applying all analysis cuts up through the fractional p_{T} difference cut.
- Figure 6.7 contains the $E_{\mathrm{T}}^{\mathrm{miss}}/H_T$ distribution after applying all analysis cuts up through the $min(\Delta\phi(j, E_{\mathrm{T}}^{\mathrm{miss}}))$ cut.
- Figure 6.8 contains the distribution of the number of b-tagged jets after applying all analysis cuts up through the $E_{\mathrm{T}}^{\mathrm{miss}}/H_T$ cut.

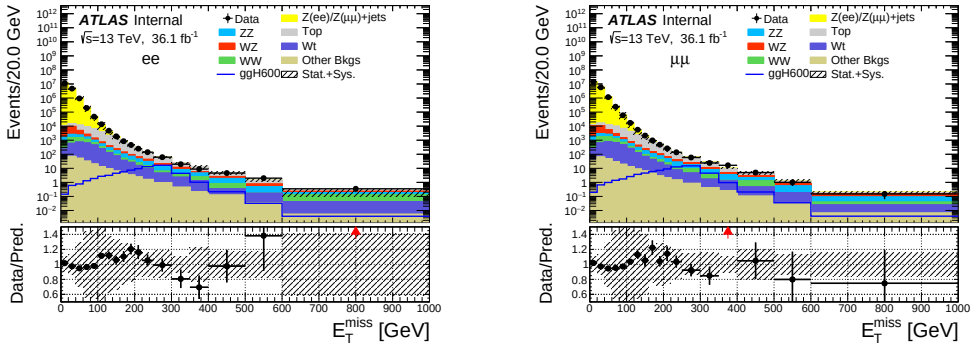

Figure 6.2: The $E_{\mathrm{T}}^{\mathrm{miss}}$ distribution of the expected backgrounds after applying all analysis cuts up through the di-lepton invariant mass window. The plot on the left shows the result for the di-electron channel whereas the right plot shows the result for the di-muon channel. The structure in the data/MC ratio is due to mismodeling of the $E_{\mathrm{T}}^{\mathrm{miss}}$, and is covered by the relevant jet and $E_{\mathrm{T}}^{\mathrm{miss}}$ systematics. The red arrows in the ratio plot indicate that the point is off the scale. The uncertainty band in the ratio includes systematic uncertainties, while the statistical uncertainty is propagated to the data/MC points.

6.3.3 Signal Acceptance and Systematic Uncertainties

The cutflow of signal sample $H \to ZZ^* \to \ell^+\ell^-\nu\bar{\nu}$ (with $m_H = 600$ GeV) are shown in Table 6.4. Numbers are normalized to integrated luminosity of 36.1 fb^{-1}. With all cuts applied, the signal efficiency is about 15% for both ee and $\mu\mu$ channel. Figure 6.9 shows the signal acceptance for both NWA heavy higgs and graviton with various pole masses.

The theoretical uncertainties on signal acceptance are considered for heavy Higgs signal samples including PDF, QCD scale and parton shower, as introduced in Sec-

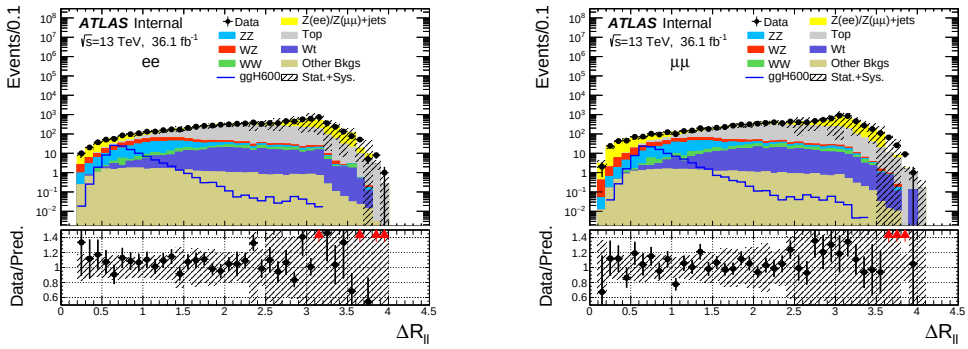

Figure 6.3: The ΔR distribution of the expected backgrounds after applying all analysis cuts up through the E_T^{miss} cut. The plot on the left shows the result for the di-electron channel whereas the right plot shows the result for the di-muon channel. The red arrows in the ratio plot indicate that the point is off the scale. The uncertainty band in the ratio includes systematic uncertainties, while the statistical uncertainty is propagated to the data/MC points.

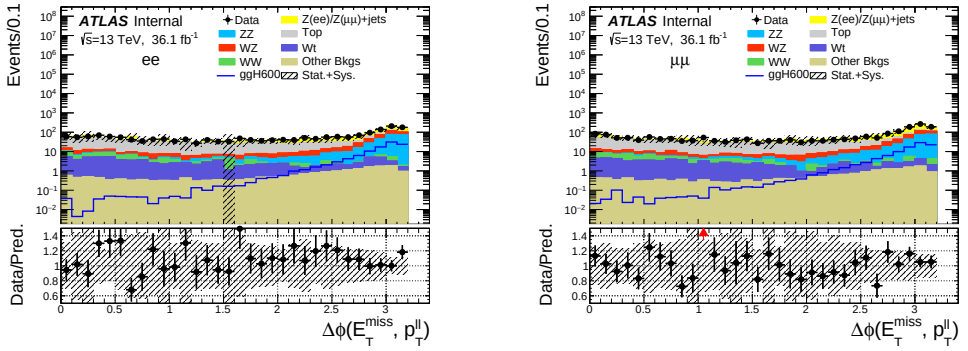

Figure 6.4: The $\Delta\phi(Z, E_{\text{T}}^{\text{miss}})$ distribution of the expected backgrounds after applying all analysis cuts up through the ΔR cut. The plot on the left shows the result for the di-electron channel whereas the right plot shows the result for the di-muon channel. The red arrows in the ratio plot indicate that the point is off the scale. The uncertainty band in the ratio includes systematic uncertainties, while the statistical uncertainty is propagated to the data/MC points.

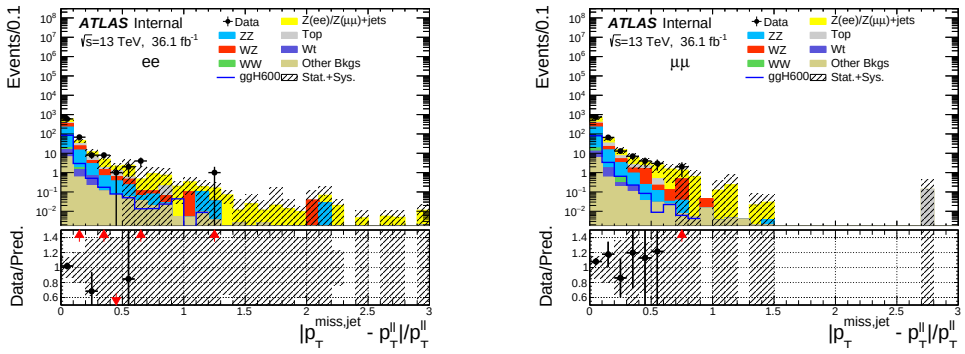

Figure 6.5: The fractional p_{T} difference distribution of the expected backgrounds after applying all analysis cuts up through the $\Delta\phi(Z, E_{\mathrm{T}}^{\mathrm{miss}})$ cut. The plot on the left shows the result for the di-electron channel whereas the right plot shows the result for the di-muon channel. The red arrows in the ratio plot indicate that the point is off the scale. The uncertainty band in the ratio includes systematic uncertainties, while the statistical uncertainty is propagated to the data/MC points.

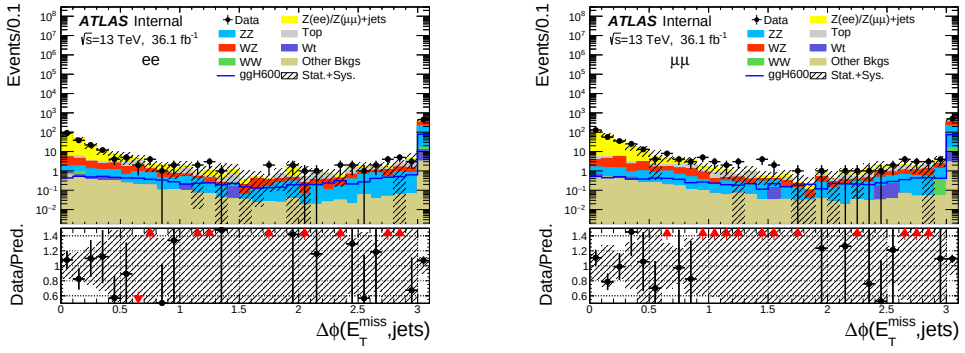

Figure 6.6: The $min(\Delta\phi(j, E_{\mathrm{T}}^{\mathrm{miss}}))$ distribution of the expected backgrounds after applying all analysis cuts up through the fractional p_{T}difference cut. The plot on the left shows the result for the di-electron channel whereas the right plot shows the result for the di-muon channel. The red arrows in the ratio plot indicate that the point is off the scale. The uncertainty band in the ratio includes systematic uncertainties, while the statistical uncertainty is propagated to the data/MC points.

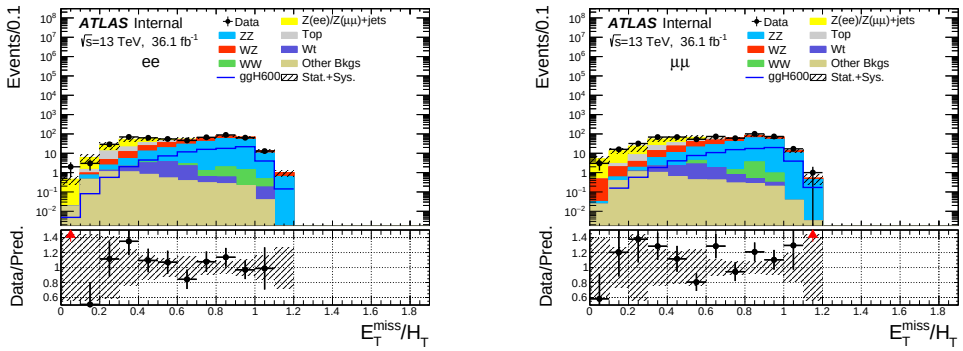

Figure 6.7: The $E_{\mathrm{T}}^{\mathrm{miss}}/H_T$ distribution of the expected backgrounds after applying all analysis cuts up through the $min(\Delta\phi(j, E_{\mathrm{T}}^{\mathrm{miss}}))$ cut. The plot on the left shows the result for the di-electron channel whereas the right plot shows the result for the di-muon channel. The red arrows in the ratio plot indicate that the point is off the scale. The uncertainty band in the ratio includes systematic uncertainties, while the statistical uncertainty is propagated to the data/MC points.

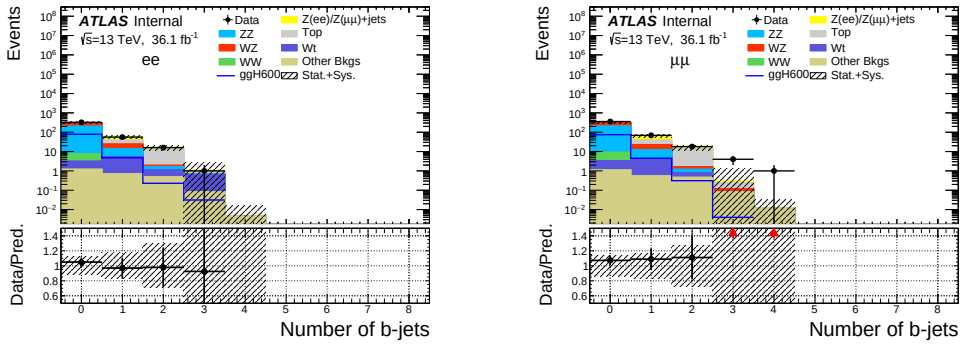

Figure 6.8: The n_{b-jets} distribution of the expected backgrounds after applying all analysis cuts up through the $E_{\mathrm{T}}^{\mathrm{miss}}/H_T$ cut. The plot on the left shows the result for the di-electron channel whereas the right plot shows the result for the di-muon channel. The red arrows in the ratio plot indicate that the point is off the scale. The uncertainty band in the ratio includes systematic uncertainties, while the statistical uncertainty is propagated to the data/MC points.

Criterion	Electron Channel			Muon Channel		
	Events	Abs. [%]	Rel. [%]	Events	Abs. [%]	Rel. [%]
$\lvert m_Z - m_{\ell\ell}\rvert < 15$ GeV	113.35	100	100	109.25	100	100
$E_T^{\text{miss}} > 120$ GeV	105.92	93.45	93.45	101.65	93.04	93.04
$\Delta R < 1.8$	104.84	92.52	98.98	100.42	91.92	98.79
$\Delta\phi(Z, E_T^{\text{miss}}) > 2.7$	89.04	78.55	84.93	84.91	77.72	84.55
Fractional p_T difference < 0.2	88.13	77.75	98.98	83.91	76.81	98.82
$min(\Delta\phi(jet, E_T^{\text{miss}})) > 0.4$	86.17	76.02	97.78	82.08	75.13	97.82
$E_T^{\text{miss}}/H_T > 0.4$	83.48	73.65	96.88	79.51	72.78	96.87
b-jet veto	75.85	66.92	90.86	72.26	66.14	90.88

Table 6.4: Cutflow table presenting absolute event counts as well as relative and absolute efficiencies for the $H \to ZZ^* \to \ell^+\ell^-\nu\bar{\nu}$ sample ($m_H = 600$ GeV).

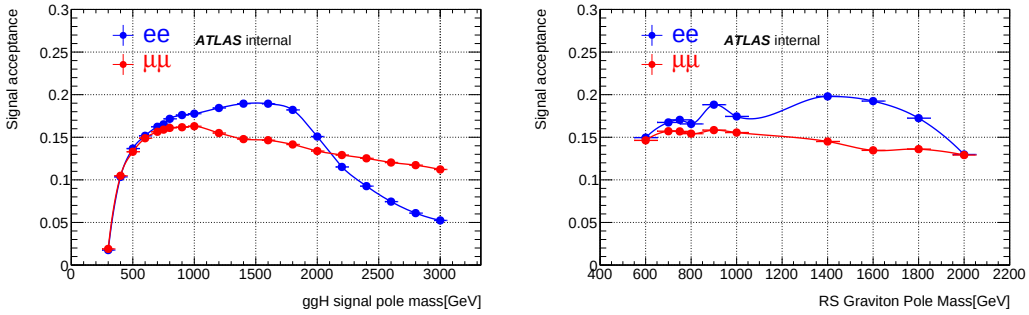

Figure 6.9: The signal acceptance versus resonance mass for heavy Higgs and Graviton. Only the statistical uncertainty is shown.

tion 5.3.2.4. The impact of these uncertainties are listed in Table 6.5 for signals with different masses.

	PDF		QCD		SHW	
	ee (%)	$\mu\mu$ (%)	ee (%)	$\mu\mu$ (%)	ee (%)	$\mu\mu$ (%)
NW300 GeV	$+0.9-0.7$	$+1.2-1.4$	$+0.5-0.5$	$+0.6-0.8$	$+2.6-2.6$	$+9.0-9.0$
NW400 GeV	$+0.7-0.9$	$+0.8-0.9$	$+0.4-0.5$	$+0.4-0.4$	$+1.0-1.0$	$+3.0-9.0$
NW500 GeV	$+0.6-0.8$	$+0.6-0.8$	$+0.4-0.4$	$+0.3-0.4$	$+1.0-1.0$	$+2.5-2.5$
NW600 GeV	$+0.5-0.7$	$+0.5-0.7$	$+0.3-0.4$	$+0.3-0.4$	$+0.8-0.8$	$+2.5-2.5$
NW700 GeV	$+0.5-0.8$	$+0.4-1.1$	$+0.3-0.4$	$+0.2-0.3$	$+0.2-0.2$	$+0.6-0.6$
NW800 GeV	$+0.4-0.6$	$+0.6-0.6$	$+0.2-0.3$	$+0.2-0.3$	$+1.7-1.7$	$+0.7-0.7$
NW900 GeV	$+0.3-0.6$	$+0.3-0.5$	$+0.2-0.3$	$+0.2-0.3$	$+0.8-0.8$	$+0.1-0.1$
NW1000 GeV	$+0.3-0.5$	$+0.3-0.7$	$+0.2-0.2$	$+0.2-0.2$	$+1.0-1.0$	$+0.6-0.6$
NW1200 GeV	$+0.2-0.3$	$+0.2-0.4$	$+0.2-0.2$	$+0.1-0.2$	$+0.2-0.2$	$+1.0-1.0$
NW1400 GeV	$+0.1-0.2$	$+0.2-0.3$	$+0.1-0.2$	$+0.1-0.2$	$+0.4-0.4$	$+3.2-3.2$

Table 6.5: Theory uncertainties of PDF, QCD and shower variation on acceptance of heavy higgs signals with mass point from 300 GeV to 1400 GeV.

Theoretical uncertainties on the acceptance of RS graviton samples have been examined and the effects are found to be much less than 1%. Given that in the high mass region sensitive to Graviton exclusion limit, data statistical uncertainty dominates the obtained limits, the theoretical uncertainties are ignored.

The experimental systematic uncertainties also impact signal acceptance, such as luminosity, pile-up, $E_{\mathrm{T}}^{\mathrm{miss}}$, jet and so on. These experimental uncertainty sources are introduced in Section 5.3.2.4 in dark matter search analysis. Table 6.6 exhibits various experimental systematic uncertainty impacts on the $H \to ZZ^* \to \ell^+\ell^-\nu\bar{\nu}$ (with m_H = 600 GeV) signal acceptance.

Tables 6.7 and 6.8 show the overall experiment systematic uncertainties for heavy Higgs and Graviton with different masses, respectively.

6.4 Background Estimation and Systematic Uncertainty

The main backgrounds and estimation strategies in this search are same as dark matter search. For ZZ process, MC is used for both yield and shape, for WZ a 3lCR is defined and involved the data-driven method, for Z+jets, a boolean "ABCD" method is adopted while for WW and Top physics, an $e\mu$ CR is defined. One major difference is that in this analysis, transverse mass m_T^{ZZ} spectrum is used for final fit while $E_{\mathrm{T}}^{\mathrm{miss}}$ spectrum is used in dark matter search analysis.

Exp. Sys. Unc. Terms	ee chancel		$\mu\mu$ chancel	
	up (%)	down (%)	up (%)	down (%)
Luminosity	3.2	3.2	3.2	3.2
pile-up	0.5	0.71	0.7	1.1
Electron	2.5	2.48	0.0	0.0
Muon	0.0	0.0	2.33	2.3
Jet	2.68	2.68	2.7	3.0
$E_{\mathrm{T}}^{\mathrm{miss}}$	0.09	0.0	0.0	0.07
Total	4.9	4.9	4.8	5.1

Table 6.6: Experimental systematic uncertainties on the $H \to ZZ^* \to \ell^+\ell^-\nu\bar{\nu}$ (with $m_H = 600$ GeV) signal acceptance.

Heavy Higgs Signals	ee chancel		$\mu\mu$ chancel	
	up (%)	down (%)	up (%)	down (%)
NW300 GeV	5.6	4.7	4.9	4.1
NW400 GeV	4.8	4.9	4.9	4.9
NW500 GeV	4.7	4.8	4.8	5.0
NW600 GeV	4.9	4.9	4.8	5.1
NW700 GeV	5.1	5.1	5.0	5.1
NW800 GeV	5.3	5.5	5.3	5.2
NW900 GeV	5.6	5.5	5.3	5.3
NW1000 GeV	5.6	5.6	5.6	5.5
NW1200 GeV	6.0	6.0	5.9	5.7
NW1400 GeV	6.4	6.3	6.3	5.9

Table 6.7: Overall experimental systematic uncertainties on the acceptance of $H \to ZZ^* \to \ell^+\ell^-\nu\bar{\nu}$ signal with different masses.

RS_G Signals	ee chancel		$\mu\mu$ chancel	
	up (%)	down (%)	up (%)	down (%)
RS_G 600 GeV	5.2	5.2	4.9	4.8
RS_G 700 GeV	5.2	5.3	5.1	5.0
RS_G 750 GeV	5.3	5.2	5.2	5.3
RS_G 800 GeV	5.5	5.2	5.1	5.1
RS_G 900 GeV	5.5	5.6	5.4	5.2
RS_G 1000 GeV	5.9	5.6	5.6	5.5
RS_G 1200 GeV	6.1	6.0	5.9	5.8
RS_G 1400 GeV	6.4	6.4	6.3	6.1
RS_G 1600 GeV	7.1	7.0	6.9	6.5
RS_G 1800 GeV	7.7	7.5	6.9	6.8
RS_G 2000 GeV	8.1	7.7	7.1	7.2

Table 6.8: Overall experimental systematic uncertainties on the acceptance of RS Graviton signal with different masses.

6.4.1 ZZ Background

The MC used for ZZ background including $qqZZ$ and $ggZZ$ processes are listed in Section 5.2.2.3. Higher order corrections NNLO QCD (as in Section 5.4.1) is applied for $qqZZ$ as a function of m_{zz} and a flat NLO/LO k-factor 1.7 $\pm$ 1.0 applied to the $ggZZ$ continuum. With all event selections shown in Table 6.3 applied, the final ZZ contributions to the signal region are:

process	ee	$\mu\mu$
$q\bar{q} \to ZZ$	161.2 $\pm$ 2.6 $\pm$ 18.6	163.8 $\pm$ 2.5 $\pm$ 18.9
$gg \to ZZ$	16.0 $\pm$ 0.4 $\pm$ 9.4	15.9 $\pm$ 0.4 $\pm$ 9.4

Table 6.9: $qqZZ$ and $ggZZ$ yields in signal region for both ee and $\mu\mu$ channel. In each box, the first number is central value of yields, the second number is statistical uncertainty and the third one is systematic uncertainty.

For the $qqZZ$ process, the experimental systematic uncertainty sources are from the items listed in 5.3.2.4 and most significant contribution is luminosity 3.2%, as indicated in Table 6.10. The theory uncertainties due to choices of PDF and QCD scales are considered, using same method as in Section 5.4.7.1. The size of the PDF and QCD scale uncertainties are about 3.0% and 10.0%, respectively. The effect of parton shower choices are found to be less than 0.1% and thus been ignored. For $ggZZ$, the uncertainty is mainly from 60% uncertainty on the flat k-factor.

Experimental Systematic Uncertainty	ee channel		$\mu\mu$ channel	
	up (%)	down (%)	up (%)	down (%)
Luminosity	3.2	3.2	3.2	3.2
pile-up	0.03	0.0	0.6	1.48
Electron	2.2	2.1	0.0	0.0
Muon	0.0	0.0	1.98	1.94
Jet	1.7	2.06	1.98	1.62
$E_{\mathrm{T}}^{\mathrm{miss}}$	0.43	0.03	0.07	0.00
Total	4.3	4.3	4.3	4.3

Table 6.10: Experimental systematic uncertainties on the $q\bar{q} \to ZZ$ background process.

6.4.2 WZ Background

Same as strategy used in dark matter search, a 3lCR is applied involving data-driven method. The scale factor $1.29 \pm 0.03 \pm 0.07$, as described in Section 5.4.2.1, is applied to MC in 3lCR. Table 6.11 shows WZ background yields in final SR using MC only and data-driven methods. Numbers from data-driven one are used in the final fit.

Channel	MC only	Data-driven
ee	$71.5 \pm 1.7 \pm 4.5$	$92.8 \pm 2.2 \pm 4.3$
$\mu\mu$	$75.6 \pm 1.8 \pm 4.4$	$99.5 \pm 2.3 \pm 3.2$

Table 6.11: WZ yields in signal region for both ee and $\mu\mu$ channel. First column shows estimates based on MC only, numbers in second column are applied with scale factor $1.29 \pm 0.03 \pm 0.07$.

The experimental systematic uncertainties on WZ process are reflected by the experimental uncertainties of scale factor about 5.5%, which is elaborated in Section 5.4.2.1. The theoretical uncertainties are from PDF and QCD scales and have an impact less than 0.5% on m_T^{ZZ} shape.

6.4.3 Top, WW, Wt and $Z \to \tau\tau$ Background

$t\bar{t}$, WW, Wt and $Z \to \tau\tau$ production all have a minor impact on the total background of $\ell^+\ell^- + E_{\mathrm{T}}^{\mathrm{miss}}$ analyses. Physics processes with one or more top quarks in the final state are suppressed by applying a b-jet veto. WW contribution is mainly removed by requiring first that the two leptons have an invariant mass compatible with that of a Z boson (the "$m_{\ell\ell}$" selection), and then by applying a high $E_{\mathrm{T}}^{\mathrm{miss}}$ cut.

$Z \to \tau\tau$ is suppressed because the two leptons usually have a lower invariant mass with respect to the Z mass (due to the presence of neutrinos in the taus decay which take part of the energy). Finally the Wt contribution is suppressed by the low cross section.

The contribution of $t\bar{t}$, WW, Wt and $Z \to \tau\tau$ backgrounds is estimated from data-driven method using $e\mu$ control region, same as the strategy in Section 5.4.3.1. The $e\mu$ control region definition is a bit different from the one defined in dark matter search, and is shown in the Table 6.12 below:

$e\mu$ **Control Region Definition**
Two Opposite flavor Opposite sign leptons ($e^{\pm}\mu^{\mp}$)
Veto any additional lepton with Loose ID and p_{T} >7 GeV
$76 < M_{e\mu} < 106$ GeV
$E_{\mathrm{T}}^{\mathrm{miss}} > 120$ GeV
$\Delta R_{e\mu} < 1.8$
$\Delta\phi(Z, E_{\mathrm{T}}^{\mathrm{miss}}) > 2.7$
Fractional p_{T} difference < 0.2
$\Delta\phi(\mathrm{jet}(p_{\mathrm{T}} > 100\mathrm{GeV}), E_{\mathrm{T}}^{\mathrm{miss}}) > 0.4$
$E_{\mathrm{T}}^{\mathrm{miss}}/H_T > 0.4$
b-jet Veto

Table 6.12: Event selection applied to define the $e\mu$ Control Region. The control region reflects the SR definition except that the opposite flavor requirement of the two selected leptons.

By applying the efficiency factor reported in Table 5.25 to the events defined in $e\mu$ CR defined above (Table 6.12), the final $e\mu$ background contribution is:

6.4.4 Z+jets background

Z+jets background is largely reduced by the $E_{\mathrm{T}}^{\mathrm{miss}} > 120$ GeV requirement but has a larger systematic uncertainty. To accurately estimate this background, we use the

Channel	MC only	Data-driven
ee	$9.9 \pm 1.6 \pm 2.4$	$9.2 \pm 2.2 \pm 1.4$
$\mu\mu$	$14.0 \pm 2.4 \pm 2.7$	$10.7 \pm 2.5 \pm 0.9$

Table 6.13: $e\mu$ background yields in signal region for both ee and $\mu\mu$ channel. First column shows estimates based on MC only, numbers in second column are estimated using data-driven method. Both statistical and systematic uncertainties are included.

same boolean "ABCD" method as described in Section 5.4.4.1. However, different from the boolean variables defined in Equations 5.10 and 5.11, two new boolean variables are defined below:

$$\text{var1} = E_{\mathrm{T}}^{\mathrm{miss}} > 120 \text{ GeV and } E_{\mathrm{T}}^{\mathrm{miss}}/H_T > 0.4 \tag{6.2}$$

$$\begin{aligned}\text{var2} = |E_T^{\mathrm{miss,jets}} - p_{\mathrm{T}}^{\ell\ell}|/p_{\mathrm{T}}^{\ell\ell} < 0.2 \text{ and } \Delta\phi(Z, E_{\mathrm{T}}^{\mathrm{miss}}) > 2.7 \text{ and } \Delta R_{\ell\ell} < 1.8 \\ \text{and } \Delta\Phi(\mathrm{jet}(p_{\mathrm{T}} > 100\mathrm{GeV}), E_{\mathrm{T}}^{\mathrm{miss}}) > 0.4 \text{ and } N_{b-jets} = 0\end{aligned} \tag{6.3}$$

to match the signal region selections.

To further reduce the correlation between two variables, two additional cuts were added to all side-band regions: $E_{\mathrm{T}}^{\mathrm{miss}} > 30$ GeV and $E_{\mathrm{T}}^{\mathrm{miss}}/H_T > 0.1$, which were optimized to remove the highly-correlated Z+jets bulk. The sizes of experimental uncertainties are also considered for optimization.

The resulting ratios for MC, as well as for data, are shown in Tables 6.14. Data-driven estimates are presented in Table 6.15.

	N_A/N_C [MC]	N_B/N_D [MC]	N_B/N_D [Data]
ee channel	0.005 ± 0.002	0.007 ± 0.0001	0.0086 ± 0.00006
$\mu\mu$ channel	0.008 ± 0.002	0.0066 ± 0.0001	0.0076 ± 0.00005

Table 6.14: Ratios N_A/N_C, N_B/N_D for the ee- and $\mu\mu$-channel. Only the statistical errors are shown. Statistical errors due to the MC subtraction are also considered for N_B/N_D (Data). WZ background yields for subtraction from data were rescaled using a scale factor of 1.29 obtained using data-driven estimate. For ZZ background, NNLO QCD & NLO EW corrections were applied. Sherpa 2.2.1 samples are used for the Z+jets background.

To determine the systematic uncertainties of the method, the difference between N_A/N_C (MC) and N_B/N_D (MC), which represents the bias induced by correlation

Channel	MC only	Data-driven
ee	8.9 ± 3.2 ± 8.1	16.6 ± 0.6 ± 11.4
$\mu\mu$	18.6 ± 5.6 ± 7.5	19.3 ± 0.6 ± 17.2

Table 6.15: Summary of the Z+jets background estimation using the boolean "ABCD" method with statistical and systematic uncertainties. Systematic uncertainties come from the level of correlation in MC, estimated by difference between N_A/N_C [MC] and N_B/N_D [MC], experimental uncertainties on this difference and subtraction of Non-Z+jets backgrounds.

in MC (non-closure), was taken into account. The impact of the experimental uncertainties on this difference was also investigated. Experimental uncertainties on subtraction of non-Z+jets background were also included. The contribution of each source to the total systematic uncertainties is summarized in Table 6.16.

	ee-channel	$\mu\mu$-channel
Methodology	$^{+30.8\%}_{-66.2\%}$	$^{+84.2\%}_{-42.8\%}$
Non- Z+jets sub.	26.3%	21.3%
Total systematic unc.	$^{+40.5\%}_{-67.5\%}$	$^{+86.9\%}_{-47.8\%}$

Table 6.16: Systematic uncertainties sources combine methodology uncertainty and uncertainty on subtraction of Non-Z+jets backgrounds from MC. Methodology uncertainty consists of correlation-induced bias $1 - \frac{N_C * N_B}{N_D * N_A}$ including experimental uncertainties (dominated by JetGroupedNP_1&3 5.3.2.4) and uncertainty associated with selection of optimal additional $E_{\mathrm{T}}^{\mathrm{miss}}$ and $E_{\mathrm{T}}^{\mathrm{miss}}/H_T$ cuts, estimated by varying them by 40% from their nominal values; both of these sources having roughly equal contribution.

6.4.5 W+jets background

The details of "fake factor" method to estimate W+jets minor background has been described in Section 5.4.5.1. The final contribution after applying all the event selection within this analysis are shown in Table 6.17 below:

	Data-driven yields
ee	$0.38 \pm 0.1 \pm 0.04$
$\mu\mu$	$1.27 \pm 1.53 \pm 0.75$

Table 6.17: W+jets estimation in the electron and muon channel as obtained from the "fake factor" data-driven technique. The systematic uncertainties are calculated as the differences in the W+jets and Z+jets MC-based fake-factors, as well as uncertainty associated with subtraction of non-W+jets backgrounds from MC.

6.4.6 Other Background

Other backgrounds including $t\bar{t}V/VVV$ make minor contribution to the contamination. Such small backgrounds are estimated based on MC-only prediction for both yields and shapes. The yields in final SRs are $1.12 \pm 0.04 \pm 0.09$ for ee channel and $1.03 \pm 0.04 \pm 0.08$ for $\mu\mu$ channel.

6.5 Results

6.5.1 Data Comparison with Predicted Background and Signal

Table 6.18 shows the observed data yields, the estimated background contributions, and the expectation for the signal processes after the final selection. The m_T^{ZZ} distributions after applying full event selections and with signals overlaid are show in Figure 6.10.

6.5.2 Limits

As shown in Figure 6.10, data is observed to agree with the SM background. No obvious new resonance in high mass scale is observed. Expected and observed 95% CL upper limits are set on $\sigma \times \mathrm{BR}(H \to ZZ^*)$ for a heavy, narrow-width Higgs for ee, $\mu\mu$ and combined channels in Figure 6.11

The expected and observed cross section upper limits at 95% CL for each considered mass point are also listed in Table 6.19 for ee, $\mu\mu$ and combined channels separately.

In addition to the upper limits on production cross-section of additional heavy Higgs bosons, an interpretation of analysis result in terms of upper limits on production cross-section of Randall-Sundrum Gravitons is also performed. The limit setting procedure is very similar to the above description for heavy Higgs boson search except

	ee	$\mu\mu$
Data	324	357
H($m_H = 300\,\text{GeV}$, MC)	46.6±1.27±2.92	51.9 ±1.4±5.36
H($m_H = 600\,\text{GeV}$, MC)	74.22±0.71±3.74	70.74 ±0.68±4.03
H($m_H = 1\,\text{TeV}$, MC)	6.43±0.06±0.37	5.62 ±0.05±0.32
Graviton($m = 600\,\text{GeV}$, MC)	155.3±2.66±8.11	150.4±2.6±7.32
$qqZZ$ (MC)	161.2 ± 2.6 ± 18.6	163.8 ± 2.5 ± 18.9
$ggZZ$ (MC)	16.0 ± 0.4 ± 9.4	15.9 ± 0.4 ± 9.4
WZ (Data-Driven)	92.8 ± 2.2 ± 4.3	99.5 ± 2.3 ± 3.2
Z+jets (Data-Driven)	16.6 ± 0.6 ± 11.4	19.3 ± 0.6 ± 17.2
$Z\tau\tau$/top/WW/Wt (Data-Driven)	9.2 ± 2.2 ± 1.4	10.7 ± 2.5 ± 0.9
W+jets (Data-Driven)	0.4 ± 0.1 ± 0.04	1.3 ± 1.5 ± 0.8
Others (MC)	1.12 ± 0.04 ± 0.09	1.03 ± 0.04 ± 0.08
Total Bkg.	297.2 ± 4.1 ± 24.2	311.5 ± 4.6 ± 27.4

Table 6.18: The observed data and expected yields (scaled to 36.1 fb^{-1}) in ee and $\mu\mu$ signal regions after full event selections. Estimates include statistical and systematic errors given where available in both MC and data-driven estimations. The total background prediction is given in the last row. The statistical and systematic errors on the total background prediction are summed quadratically from each individual process. The "Others" category is composed of ttV and VVV backgrounds.

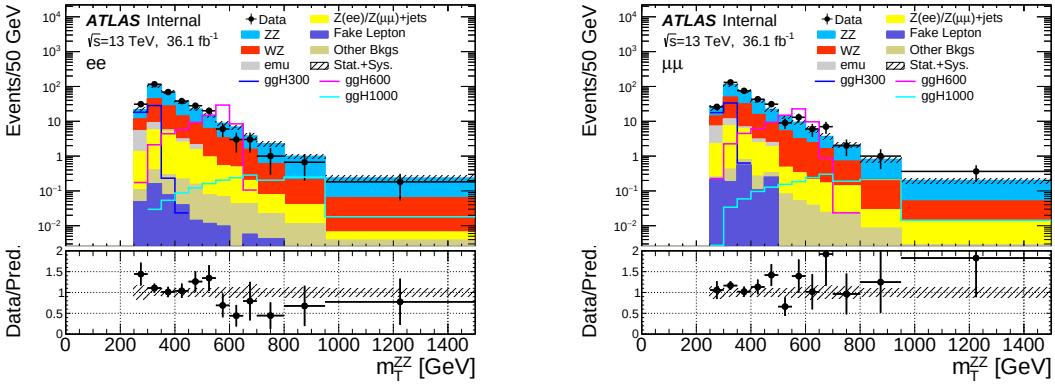

(a) (b)

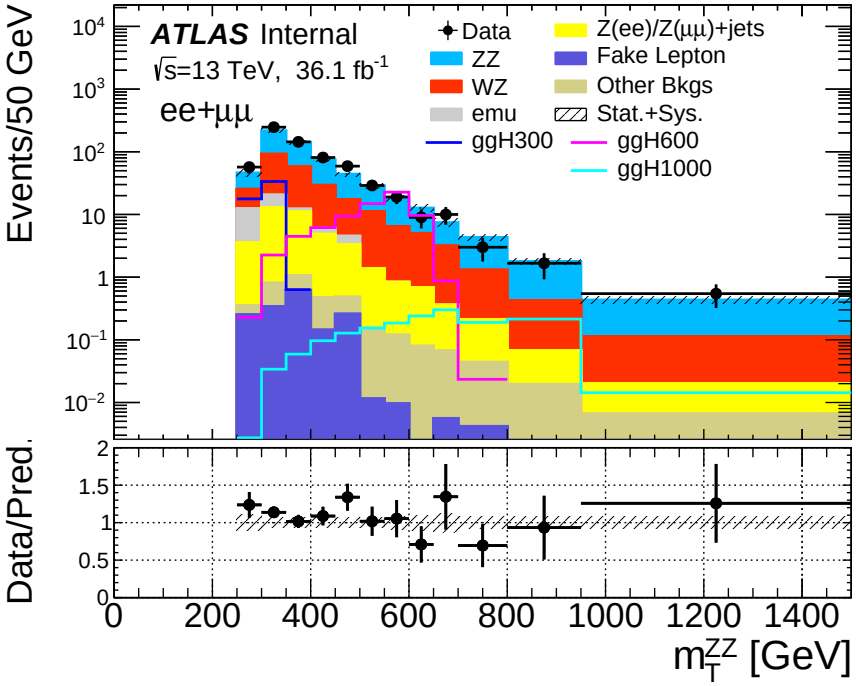

(c)

Figure 6.10: The m_T^{ZZ} distribution after final selections in the (a) ee channel, (b) $\mu\mu$ channel, and (c) $ee+\mu\mu$ combined channel. The yield of WZ, $Top/WW/Z \to \tau\tau$ and $Z \to ee/Z \to \mu\mu$ backgrounds are estimated using data-driven method and the m_T^{ZZ} shapes for these backgrounds are derived from MC samples. Signals are scaled to the SM cross section values time branching fraction of $H \to ZZ^*$ and $ZZ \to \ell\ell\nu\nu$. The ZZ backgrounds are fully estimated from theoretical predictions and higher order corrections are applied. Both statistical and systematic uncertainties are included in the uncertainties bands, and they are summed quadratically.

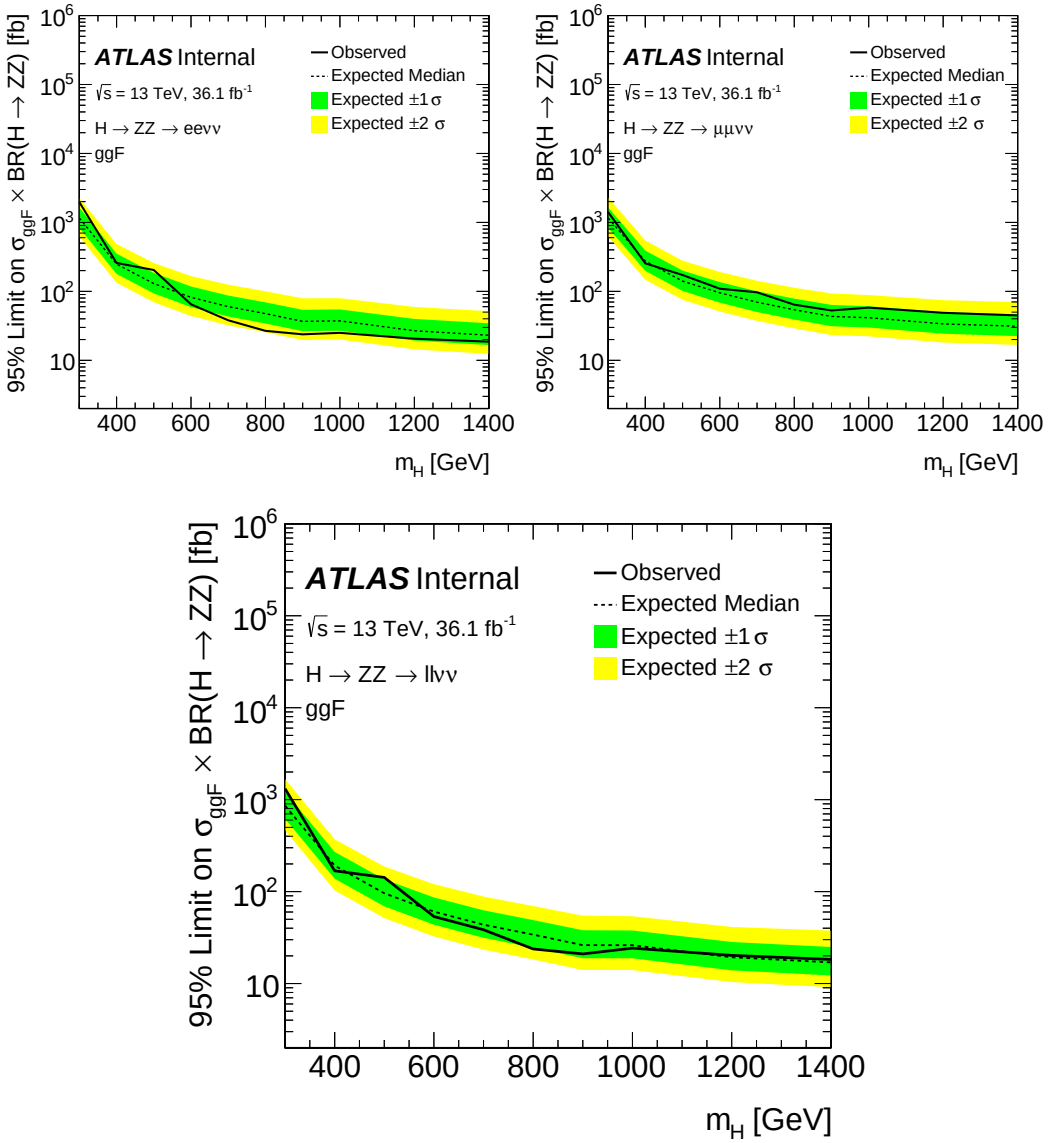

Figure 6.11: 95% C.L. limits on $\sigma \times \mathrm{BR}(H \to ZZ^*)$ for a narrow width heavy Higgs boson produced a function of its pole mass. The limits are derived using events in ee (top left), $\mu\mu$ (top right) and combined channels (bottom). The observed and expected limits are derived with considering the full uncertainties discussed in previous sections. The limits are derived for mass points between 300 GeV and 1 TeV with a 100 GeV interval. Two additional mass points are added, 1.2 TeV and 1.4 TeV. And limit lines between each mass points are interpolated using an exponential function. Both the statistical and systematic uncertainties are considered in the limit setting.

Limits on production cross section of heavy Higgs signals				
Mass Point [GeV]	Expected Limits [fb]	Exp+2σ, Exp+1σ	Exp-1σ, Exp-2σ	Observed Limits
ee channel				
300.0 GeV	1159.26	2259.26 , 1637.31	835.31 , 622.20	1968.06
400.0 GeV	248.45	486.63 , 352.86	179.02 , 133.35	258.23
500.0 GeV	129.72	257.88 , 184.90	93.47 , 69.62	204.01
600.0 GeV	81.90	166.66 , 117.68	59.01 , 43.96	64.96
700.0 GeV	59.99	125.00 , 86.96	43.23 , 32.20	38.06
800.0 GeV	47.50	100.23 , 69.25	34.23 , 25.50	26.77
900.0 GeV	36.73	79.29 , 54.00	26.46 , 19.71	23.82
1000.0 GeV	37.34	79.57 , 54.69	26.90 , 20.04	25.04
1200.0 GeV	26.84	59.41 , 39.87	19.34 , 14.41	20.59
1400.0 GeV	23.09	51.64 , 34.42	16.64 , 12.39	18.66
Mass Point [GeV]	Expected Limits [fb]	Exp+2σ, Exp+1σ	Exp-1σ, Exp-2σ	Observed Limits
$\mu\mu$ channel				
300.0 GeV	1160.43	2298.49 , 1644.86	836.15 , 622.83	1411.22
400.0 GeV	274.35	547.03 , 389.23	197.69 , 147.25	254.58
500.0 GeV	140.74	278.04 , 200.01	101.41 , 75.54	172.62
600.0 GeV	95.17	191.19 , 136.08	68.57 , 51.08	109.28
700.0 GeV	69.63	142.29 , 100.20	50.17 , 37.37	96.85
800.0 GeV	54.10	112.89 , 78.47	38.98 , 29.04	64.14
900.0 GeV	43.32	93.09 , 63.56	31.22 , 23.25	52.80
1000.0 GeV	41.49	88.53 , 60.80	29.90 , 22.27	58.10
1200.0 GeV	33.74	74.62 , 50.03	24.31 , 18.11	48.86
1400.0 GeV	31.15	69.82 , 46.46	22.44 , 16.72	44.79
Mass Point [GeV]	Expected Limits [fb]	Exp+2σ, Exp+1σ	Exp-1σ, Exp-2σ	Observed Limits
combined channel				
300.0 GeV	863.56	1679.65 , 1218.76	622.25 , 463.50	1320.04
400.0 GeV	191.93	371.53 , 270.52	138.29 , 103.01	168.34
500.0 GeV	96.01	187.45 , 135.89	69.18 , 51.53	142.67
600.0 GeV	60.62	120.53 , 86.39	43.68 , 32.54	53.60
700.0 GeV	43.65	88.28 , 62.60	31.45 , 23.43	38.49
800.0 GeV	34.04	69.60 , 49.01	24.53 , 18.27	23.79
900.0 GeV	26.17	54.75 , 38.01	18.86 , 14.05	21.01
1000.0 GeV	26.12	53.99 , 37.77	18.82 , 14.02	24.27
1200.0 GeV	19.33	41.24 , 28.32	13.93 , 10.38	20.26
1400.0 GeV	16.99	37.67 , 24.98	12.24 , 9.12	18.28

Table 6.19: The observed and expected 95% CL upper limits on production cross-section of additional narrow-width heavy Higgs bosons times the branching fraction of Higgs to ZZ decay $\sigma\times\mathrm{BR}(H \to ZZ^*)$, Limits are derived using ee, $\mu\mu$ and combined ($ee + \mu\mu$) channels, as indicated in the table. Both the statistical and systematic uncertainties are considered in the limit setting.

that signal samples are Graviton samples with mass points between 600 GeV and 2 TeV.

Figure 6.12 gives the predicted and observed limits of the RS Graviton samples. Currently, it is possible to exclude the graviton mass up to around 1.3TeV. The expected and observed limits are also shown in Table 6.20 (both statistical and systematic uncertainties).

6.5.3 Short Summary

The number of observed events is found to be consistent with the SM prediction and both observed and expected upper limits are set on the production cross section of heavy Higgs boson in the mass range from 300 GeV to 1.4 TeV. The limits are derived at 95% CL using a fit to the transverse mass distribution of the di-lepton and $E_{\mathrm{T}}^{\mathrm{miss}}$ system. Interpretation is also performed in terms of a spin-2 graviton from Randall-Sundrum model in the mass range from 600 GeV to 2 TeV.

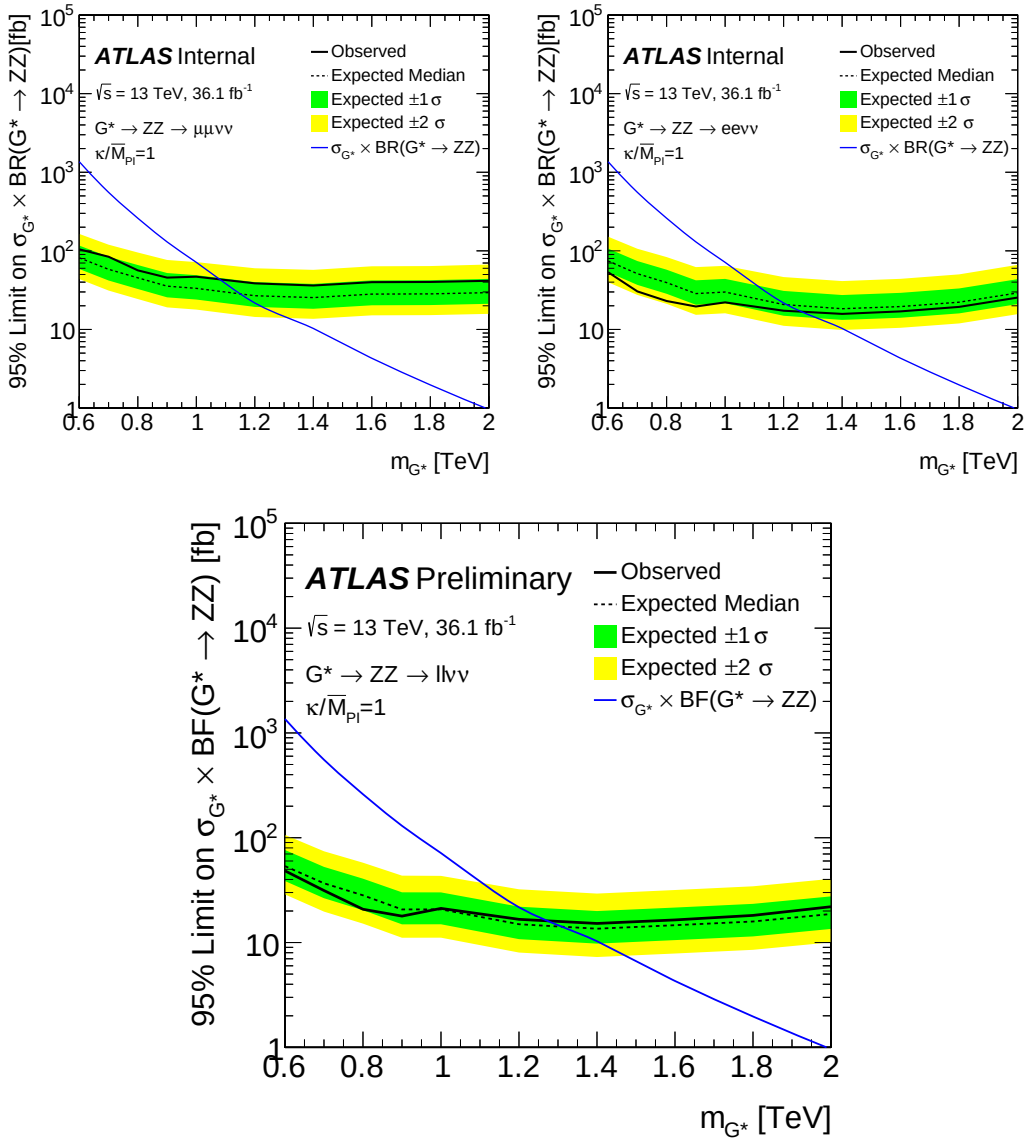

Figure 6.12: 95% C.L. limits on $\sigma \times \mathrm{BR}(G^* \to ZZ)$ for a Randall-Sundrum Graviton as a function of its pole mass. The limits are derived using events in ee (top left), $\mu\mu$ (top right) and combined channels (bottom). The observed and expected limits are derived with considering the full uncertainties discussed in previous sections. The limits are derived for mass points between 600 GeV and 2 TeV. Limit lines between each mass points are interpolated using an exponential function.

Limits on Randall-Sundrum Graviton				
Mass Point [GeV]	Expected Limits [fb]	Exp+2σ, Exp+1σ	Exp-1σ, Exp-2σ	Observed Limits
ee channel				
600.0	76.65	155.70 , 110.11	55.23 , 41.14	52.00
700.0	52.51	108.75 , 75.97	37.84 , 28.18	30.15
800.0	40.40	85.12 , 58.89	29.11 , 21.69	22.89
900.0	29.26	63.42 , 43.09	21.08 , 15.70	19.54
1000.0	30.57	65.72 , 44.90	22.03 , 16.41	22.08
1200.0	21.11	47.18 , 31.46	15.21 , 11.33	17.37
1400.0	18.69	41.94 , 27.89	13.47 , 10.03	15.85
1600.0	19.92	44.83 , 29.75	14.35 , 10.69	17.08
1800.0	22.65	51.09 , 33.86	16.32 , 12.15	19.49
2000.0	29.71	67.64 , 44.45	21.41 , 15.95	25.61
Mass Point [GeV]	Expected Limits [fb]	Exp+2σ, Exp+1σ	Exp-1σ, Exp-2σ	Observed Limits
$\mu\mu$ channel				
600.0	83.30	167.30 , 119.12	60.03 , 44.71	101.07
700.0	58.96	121.22 , 85.04	42.48 , 31.64	82.30
800.0	45.89	96.20 , 66.70	33.07 , 24.63	55.39
900.0	35.94	77.33 , 52.77	25.89 , 19.29	45.02
1000.0	33.63	72.49 , 49.44	24.23 , 18.05	46.56
1200.0	27.03	60.39 , 40.25	19.47 , 14.51	38.46
1400.0	25.59	57.65 , 38.22	18.44 , 13.73	36.19
1600.0	28.35	64.00 , 42.39	20.43 , 15.21	39.96
1800.0	28.53	64.45 , 42.68	20.56 , 15.31	40.21
2000.0	29.60	67.43 , 44.30	21.33 , 15.89	41.63
Mass Point [GeV]	Expected Limits [fb]	Exp+2σ, Exp+1σ	Exp-1σ, Exp-2σ	Observed Limits
combined channel				
600.0	55.18	109.31 , 78.52	39.76 , 29.62	46.46
700.0	37.55	75.77 , 53.82	27.06 , 20.16	30.56
800.0	28.84	58.92 , 41.52	20.78 , 15.48	20.49
900.0	21.15	44.33 , 30.76	15.24 , 11.35	17.67
1000.0	21.14	44.04 , 30.64	15.23 , 11.35	20.97
1200.0	15.21	32.72 , 22.36	10.96 , 8.16	16.64
1400.0	13.79	29.79 , 20.31	9.94 , 7.40	15.26
1600.0	14.91	32.24 , 21.95	10.74 , 8.00	16.51
1800.0	16.16	34.97 , 23.80	11.65 , 8.67	18.20
2000.0	19.03	41.17 , 28.02	13.71 , 10.21	22.02

Table 6.20: The observed and expected 95% CL upper limits on the production cross-section of a Randall-Sundrum Graviton times the branching fraction of Graviton to ZZ decay $\sigma\times\mathrm{BR}(G^* \rightarrow ZZ)$, shown for mass points between 600GeV and 2TeV. Limits are derived using ee, $\mu\mu$ and combined ($ee + \mu\mu$) channels, as indicated in the table. Both the statistical and systematic uncertainties are considered in the limit setting.

CHAPTER VII

Summary

This thesis presents the searches for dark matter particles from the associated production of Zh, $Z \to ll$, $h \to$ invisible with $m_h = 125$ GeV and new resonances with beyond the SM Higgs boson productions in $H \to ZZ^* \to \ell^+\ell^-\nu\bar{\nu}$ channel at high mass scale. Both analyses have the same experimental final state: di-lepton plus large $E_{\mathrm{T}}^{\mathrm{miss}}$. The data used in these analyses are created in proton-proton collisions at the center-of-mass energy of 13 TeV and are collected by the ATLAS experiment, with a total integrated luminosity of 36.1 fb^{-1} during 2015 and 2016. Results of these searches are summarized below:

1) Search for dark matter particles

For the dark matter search, $E_{\mathrm{T}}^{\mathrm{miss}}$ is used as the discriminant to observe signature of the dark matter. Data is observed to be consistent with the SM predictions. An observed (expected) upper limit of 67% (39%) is set on BR($h \to$ inv.) at the 95% CL for $m_h = 125$ GeV. The observed limit is higher than the expected one due to some accesses of current observed data in $\mu\mu$ channel, correpsonding to a significance of 1.9σ. Upper limits at 95% CL are also set on production cross sections of invisible Higgs decay with m_h between 110 GeV and 400 GeV.

2) Search for new resonances

For new heavy resonance searches, transverse mass of the di-lepton and $E_{\mathrm{T}}^{\mathrm{miss}}$ system is used as the discriminant to separate signals and backgrounds. Data is found to be consistent with the SM predicted backgrounds, no new physics is observed. Both observed and expected upper limits at 95% CL for production cross-sections of an additional heavy Higgs boson with a narrow width are derived within the mass range from 300 GeV to 1.4 TeV. In addition, cross-section limits are set on the production of graviton candidates predicted by the Randall-Sundrum model within the mass range from 600 GeV to 2 TeV.

By the end of LHC Run II, at the end of 2018, approximately 140 fb^{-1} data from proton-proton collisions will be collected by the ATLAS detector. Comparing to the data used in these analyses (36.1 fb^{-1}), a factor of 3.9 increase in data sample will improve the sensitivity of dark matter search by about a factor of 2, which will improve the expected limit from 39% (current result) to 20% (at the end of Run II). The sensitivity of search for the new heavy resonances will be significantly improved. For example, the limit of graviton mass will be extended from 1.3 TeV to 1.6 TeV. Ultimately, the LHC will deliver 3000 fb^{-1} data, which will provide great potential to discover new physics.

BIBLIOGRAPHY

BIBLIOGRAPHY

[1] Lyndon Evans and Philip Bryant., LHC Machine, JINST, 3(08):S08001, 2008.

[2] The ATLAS Collaboration et al, The ATLAS Experiment at the CERN Large Hadron Collider, JINST, 3:S08003, 2008.

[3] CMS Collaboration, The CMS Experiment at the CERN LHC, JINST, 3:S08004, 2008.

[4] S. L. Glashow, Partial-symmetries of weak interactions, Nuclear Physics 22 no. 4, (1961) 579-588.

[5] S. Weinberg, A Model of Leptons, Phys. Rev. Lett. 19 (1967) 1264-1266.

[6] A. Salam, Elementary Particle Physics: Relativistic Groups and Analyticity, Almqvist and Wiksell, Stockholm, 1968.

[7] F. Englert and R. Brout, Broken symmetry and the mass of gauge vector mesons, Phys. Rev. Lett., 13:321, 1964.

[8] P.W.Higgs, Broken Symmetries and the Masses of Gauge Bosons, Phys. Rev. Lett. 13 (1964) 508.

[9] The ATLAS Collaboration, Observation of a new particle in the search for the Standard Model Higgs boson with the ATLAS detector at the LHC, Phys. Lett., B716:1, 2012.

[10] The CMS Collaboration, Observation of a new boson at a mass of 125 GeV with the CMS experiment at the LHC, Phys. Lett., B716:30, 2012.

[11] U.S. Department of Energy, Building for Discovery-Strategic Plan for U.S. Particle Physics in the Global Context, Phys. Lett., B716:30, 2012.

[12] The ATLAS Collaboration, Search for Invisible Decays of a Higgs Boson Produced in Association with a Z Boson in ATLAS Phys. Rev. Lett. 112, 201802

[13] The ATLAS Collaboration, Search for an invisibly decaying Higgs boson or dark matter candidates produced in association with a Z boson in pp collisions at $\sqrt{s} = 13$ TeV with the ATLAS detector Physics Letters B 776 (2018) 318-337.

[14] G.C. Branco, P.M. Ferreira, L. Lavoura, M.N. Rebelo, Marc Sher, et al., Theory and phenomenology of two-Higgs-doublet models, Phys. Rept., 516:1-102, 2012.

[15] A. Hill and J.J. van der Bij., Strongly interacting singlet-doublet Higgs model, Phys. Rev., D 36:3463-3473, 1987.

[16] S. Profumo, M. J. Ramsey-Musolf, and G. Shaughnessy, Singlet Higgs phenomenology and the electroweak phase transition, JHEP 0708 (2007) 010.

[17] Tania Robens, Tim Stefaniak, Status of the Higgs Singlet Extension of the Standard Model after LHC Run 1, Eur. Phys. J. C (2015) 75:104.

[18] The ATLAS Collaboration, Search for an additional, heavy Higgs boson in the $H \to$ ZZ decay channel at $\sqrt{s} = 8$ TeV in pp collision data with the ATLAS detector, Eur. Phys. J. C (2016) 76:45

[19] The ATLAS Collaboration, Search for heavy ZZ resonances in the $\ell^+\ell^-\ell^+\ell^-$ and $\ell^+\ell^-\nu\bar{\nu}$ final states using proton proton collisions at $\sqrt{s} = 13$ TeV with the ATLAS detector, arXiv:1712.06386 [hep-ex]

[20] https://wikipedia.org/wiki/Standard Model.

[21] P. Langacker, Introduction to the Standard Model and Electroweak Physics, arXiv:0901.0241 [hep-ph].

[22] Nicola Cabibbo, Unitary Symmetry and Leptonic Decays, Phys.Rev.Lett. 10, 531 (1963).

[23] M. Kobayashi and T. Maskawa, CP Violation in the Renormalizable Theory of Weak Interaction, Prog.Theor.Phys. 49, 652 (1973).

[24] B. W. Lee and S. Weinberg, Cosmological Lower Bound on Heavy Neutrino Masses, Phys. Rev. Lett. 39 (1977) 165.

[25] J. Goodman, M. Ibe, A. Rajaraman, W. Shepherd, T. Tait, H-B. Yu, Constraints on Dark Matter from Colliders, Phys. Rev. D 82 (2010) 116010.

[26] M. C. Bento, O. Bertolami, R. Rosenfeld, and L. Teodoro, Self-interacting dark matter and the Higgs boson, Phys. Rev. D 62 (2000) 041302.

[27] C. Englert, T. Plehn, D. Zerwas and P. M. Zerwas, Exploring the Higgs portal, Phys. Lett. B 703 (2011) 298.

[28] A. Djouadi, O. Lebedev, Y. Mambrini, and J. Quevillon,, Implications of LHC searches for Higgs-portal dark matter, Phys.Lett. B709 (2012) 65-69.

[29] L. Lopez-Honorez, T. Schwetz, and J. Zupan, Higgs portal, fermionic dark matter, and a Standard Model like Higgs at 125 GeV, Phys.Lett. B716 (2012) 179-185.

[30] P. J. Fox, R. Harnik, J. Kopp, and Y. Tsai, Missing Energy Signatures of Dark Matter at the LHC, Phys.Rev. D85 (2012) 056011.

[31] N. Craig, J. A. Evans, R. Gray, C. Kilic, M. Park, et al., Multi-Lepton Signals of Multiple Higgs Bosons, JHEP 1302 (2013) 033

[32] Lisa Randall, Raman Sundrum, A Large Mass Hierarchy from a Small Extra Dimension, Phys. Rev. Lett. 83 (1999) 3370

[33] H. Davoudiasl, J. L. Hewett and T. G. Rizzo, Bulk gauge fields in the Randall-Sundrum model, Phys. Lett. B 473 (2000) 43

[34] Hooman Davoudiasl, Echoes from a Warped Dimension, Nucl.Phys.B, Proc.Suppl.200-202 2010:149-158,2010.

[35] Richard D. Ball et al., Parton distributions for the LHC Run II, JHEP, 04:040, 2015.

[36] J. C. Collins, D. E. Soper, and G. F. Sterman, Factorization of Hard Processes in QCD, Adv.Ser.Direct.High Energy Phys. 5 (1988) 1-91 arXiv:hep-ph/0409313 [hep-ph].

[37] J. Womersley, QCD at the Tevatron: Status and prospects, arXiv:hep-ex/0012061.

[38] The NNPDF collaboration, https://nnpdf.hepforge.org/images/.

[39] M. Dobbs and J. B. Hansen, The HepMC C++ Monte Carlo Event Record for High Energy Physics, Comput.Phys.Commun. 134 (2001) 41-46.

[40] T. Sjostrand, S. Mrenna, and P. Z. Skands, PYTHIA 6.4 Physics and Manual, JHEP 0605 (2006) 026.

[41] T. Sjostrand, S. Mrenna, and P. Z. Skands, A Brief Introduction to PYTHIA 8.1, Comput.Phys.Commun. 178 (2008) 852-867,

[42] J. Alwall, R. Frederix, S. Frixione, V. Hirschi, F. Maltoni, O. Mattelaer, H.-S. Shao, T. Stelzer, P. Torrielli, M. Zaro, The automated computation of tree-level and next-to-leading order differential cross sections, and their matching to parton shower simulations, JHEP 07 (2014) 079.

[43] T. Gleisberg, S. Hoeche, F. Krauss, M. Schonherr, S. Schumann, et al., Event generation with SHERPA 1.1, JHEP 0307 (2003) 001.

[44] P. Nason, A New Method for Combining NLO QCD with Shower Monte Carlo Algorithms, JHEP 0411 (2004) 040, arXiv:hep-ph/0409146 [hep-ph]

[45] N. Kauer and G. Passarino, nadequacy of zero-width approximation for a light Higgs boson signal, JHEP 1208 (2012) 116

[46] N. Kauer, nterference effects for $H \to WW/ZZ \to \ell\bar{\nu}_l\bar{\ell}\nu_l$ at the LHC, JHEP 1312 (2013) 082

[47] CERN, The CERN accelerator complex, http://cds.cern.ch/record/2197559.

[48] The ALICE Collaboration, The ALICE experiment at the CERN LHC, 2008 JINST 3 S08002.

[49] The LHCb Collaboration, The LHCb Detector at the LHC, 2008 JINST 3 S08005.

[50] O. S. Bruning (Ed.) et al., LHC design report. Vol. I: The LHC main ring. http://cds.cern.ch/record/782076.

[51] ATLAS Luminosity Public Results Run2, https://twiki.cern.ch/twiki/bin/view/AtlasPublic/LuminosityPublicResultsRun2.

[52] ATLAS Technical Paper List Of Figures, https://twiki.cern.ch/twiki/bin/view/AtlasPublic/AtlasTechnicalPaperListOfFiguresChapter

[53] C Kourkoumelis and S Vourakis, HYPATIA-an online tool for ATLAS event visualization, http://iopscience.iop.org/article/10.1088/0031-9120/49/1/21.

[54] L. Evans, The Large Hadron Collider (LHC), New J.Phys. 9 (2007) 335.

[55] G. Aad, M. Ackers, F. Alberti, M. Aleppo, G. Alimonti, et al., ATLAS pixel detector electronics and sensors, JINST 3 (2008) P07007.

[56] A. Ahmad, Z. Albrechtskirchinger, P. Allport, J. Alonso, L. Andricek, et al., The Silicon microstrip sensors of the ATLAS semiconductor tracker, Nucl.Instrum.Meth. A578 (2007) 98-118.

[57] ATLAS TRT Collaboration , E. Abat et al., The ATLAS Transition Radiation Tracker (TRT) proportional drift tube: Design and performance, JINST 3 (2008) P02013.

[58] The ATLAS Collaboration, ATLAS liquid-argon calorimeter: Technical Design Report, Technical Design Report ATLAS. CERN, Geneva, 1996.

[59] The ATLAS Collaboration, ATLAS tile calorimeter: Technical Design Report, Technical Design Report ATLAS. CERN, Geneva, 1996.

[60] D. Gingrich, G. Lachat, J. Pinfold, J. Soukoup, D. Axen, et al., Construction, assembly and testing of the ATLAS hadronic end-cap calorimeter, JINST 2 (2007) P05005.

[61] A. Artamonov, D. Bailey, G. Belanger, M. Cadabeschi, T. Chen, et al., The ATLAS forward calorimeters, JINST 3 (2008) P02010.

[62] The ATLAS Collaboration, The Run-2 ATLAS Trigger System, ATL-DAQ-PROC-2016-003

[63] The ATLAS Collaboration, The ATLAS Experiment at the CERN Large Hadron Collider, 2008 JINST 3 S0800

[64] The ATLAS Collaboration, The ATLAS Simulation Infrastructure, Eur. Phys. J. C (2010) 70: 823.

[65] C Kourkoumelis and S Vourakis, HYPATIA-an online tool for ATLAS event visualization, 2014 Phys. Educ.49 21

[66] The ATLAS Collaboration, Electron reconstruction and identification efficiency measurements with the ATLAS detector using the 2011 LHC proton-proton collision data, Eur.Phys.J. C74 no. 7, (2014) 2941,

[67] The ATLAS Collaboration, Photon and electron identification with the ATLAS detector, ATL-PHYS-PROC-2016-230

[68] The ATLAS Collaboration, Muon reconstruction performance of the ATLAS detector in proton-proton collision data at $\sqrt{s} = 13$ TeV, Eur. Phys. J.C (2016) 76:292.

[69] The ATLAS Collaboration, Measurement of the muon reconstruction performance of the ATLAS detector using 2011 and 2012 LHC proton-proton collision data, Eur.Phys.J. C74 (2014) 3130.

[70] The ATLAS Collaboration, Topological cell clustering in the ATLAS calorimeters and its performance in LHC Run 1, Eur. Phys. J. C (2017) 77:490.

[71] The ATLAS Collaboration, Commissioning of the ATLAS b-tagging algorithms using $t\bar{t}$ events in early Run-2 data, ATL-PHYS-PUB-2015-039, 2015, `http://cds.cern.ch/record/2047871.`

[72] The ATLAS Collaboration, Expected performance of the ATLAS b-tagging algorithms in Run-2, ATL-PHYS-PUB-2015-022, `https://cdsweb.cern.ch/record/2037697.`

[73] The ATLAS Collaboration, Determination of the tau energy scale and the associated systematic uncertainty in proton-proton collisions at $\sqrt{s} = 7$ TeV with the ATLAS detector at the LHC in 2011, ATLAS-CONF-2012-054.

[74] Matteo Cacciari et al, The catchment area of jets, JHEP04(2008)005.

[75] The ATLAS Collaboration, Performance of missing transverse momentum reconstruction with the ATLAS detector using proton-proton collisions at $\sqrt{s} =$ 13 TeV, arXiv:1802.08168 [hep-ex].

[76] ATLAS Physics Modeling Group, CentralMC15ProductionList, https://twiki.cern.ch/twiki/bin/viewauth/AtlasProtected/CentralMC15ProductionList.

[77] T. Sjostrand, S. Mrenna, and P. Z. Skands, A Brief Introduction to PYTHIA 8.1, Computer Physics Communications.178 (2008) 852-867, arXiv:0710.3820 [hep-ph]

[78] S. Agostinelli et al., GEANT4: A Simulation toolkit, Nucl.Instrum.Meth. A506 (2003) 250-303

[79] J. Allison, K. Amako, J. Apostolakis, H. Araujo, P. Dubois, et al., Geant4 developments and applications, IEEE Trans.Nucl.Sci. 53 (2006) 270.

[80] S. Agostinelli et al., Geant4-a simulation toolkit, Nucl. Instrum. Meth. A506 (2003) 250-303

[81] J. Allison et al., Geant4 developments and applications, IEEE Trans. Nucl. Sci. 53 (2006) 270.

[82] S. Heinemeyer et al., Handbook of LHC Higgs Cross Sections: 3. Higgs Properties, arXiv:1307.1347 [hep-ph]

[83] J. Alwall, M. Herquet, F. Maltoni, O. Mattelaer, and T. Stelzer, MadGraph 5: going beyond, JHEP 06 (2011) 128, arXiv:1106.0522 [hep-ph].

[84] NNPDF Collaboration, R. D. Ball et al., Parton distributions for the LHC run II, JHEP 04 (2015) 040, arXiv:1410.8849 [hep-ph].

[85] ATLAS Muon Combined Performance Group, MCPAnalysisGuidelinesMC15, https://twiki.cern.ch/twiki/bin/view/AtlasProtected/MCPAnalysisGuidelinesMC15

[86] ATLAS Egamma Combined Performance Group, Electron Identification, https://twiki.cern.ch/twiki/bin/view/AtlasProtected/EGammaIdentificationRun2#Electron_identification

[87] M. Cacciari, G. P. Salam and G. Soyez, The anti-kt jet clustering algorithm, JHEP 0804 (2008) 063, arXiv: 0802.1189 [hep-ph].

[88] The ATLAS Collaboration, Properties of Jets and Inputs to Jet Reconstruction and Calibration with the ATLAS Detector Using Proton-Proton Collisions at $\sqrt{s} = 13TeV$ ATL-PHYS-PUB-2015-036, 2015, http://cds.cern.ch/record/2044564.

[89] The ATLAS Collaboration, Tagging and suppression of pileup jets with the ATLAS detector, ATLAS-CONF-2014-018, 2014, http://cds.cern.ch/record/1700870.

[90] The ATLAS Collaboration, Selection of jets produced in 13 TeV proton-proton collisions with the ATLAS detector, ATLAS-CONF-2015-029, 2015, http://cds.cern.ch/record/2016323.

[91] The ATLAS Collaboration, Commissioning of the ATLAS b-tagging algorithms using $t\bar{t}$ events in early Run-2 data, ATL-PHYS-PUB-2015-039, 2015, http://cds.cern.ch/record/2047871.

[92] The ATLAS Collaboration, Recommendations of the Physics Objects and Analysis Harmonisaton Study Groups 2014, ATL-COM-PHYS-2014-451, 2014, http://cds.cern.ch/record/1700874.

[93] The ATLAS Collaboration, Expected performance of missing transverse momentum reconstruction for the ATLAS detector at $\sqrt{s} = 13TeV$, ATL-PHYS-PUB-2015-023, 2015, http://cds.cern.ch/record/2037700.

[94] ATLAS JetEtMiss Performance Group, Usage of Missing ET in analyses: rebuilding and systematics, https://twiki.cern.ch/twiki/bin/view/AtlasProtected/METUtilities.

[95] The ATLAS Collaboration, Jet energy measurement and its systematic uncertainty in proton-proton collisions at $\sqrt{s}$=7 TeV with the ATLAS detector, Eur. Phys. J. C (2015) 75:17.

[96] The ATLAS Collaboration, Study of $\ell^+\ell^-+E_{\mathrm{T}}^{\mathrm{miss}}$ final state in HZZ group with proton-proton collisions at $\sqrt{s} = 13TeV$: objects definition and background estimation, ATL-COM-PHYS-2015-1275, 2016, http://cds.cern.ch/record/2058246.

[97] The ATLAS Collaboration HZZ Group, Search for an additional heavy Higgs boson in the H $\rightarrow$ ZZ $\rightarrow$ ll$\nu\nu$ final state in pp collisions at $\sqrt{s} = 13$ TeV with the ATLAS detector, http://cds.cern.ch/record/2058243.

[98] The ATLAS Collaboration, Supporting note for the ZH(inv) and the mono-Z search in the $\ell^+\ell^-+E_{\mathrm{T}}^{\mathrm{miss}}$decay channel, ATL-COM-PHYS-2016-423, http://cds.cern.ch/record/2150065.

[99] The ATLAS Collaboration, Supporting note for the search for additional heavy Higgs bosons in the $H \rightarrow ZZ^* \rightarrow \ell^+\ell^-\nu\bar{\nu}$final state, ATL-COM-PHYS-2016-421, 2016, http://cds.cern.ch/record/2150051.

[100] The ATLAS Collaboration HZZ Group, Theoretical Uncertainties Occurring In $H \rightarrow ZZ$analyses, http://cds.cern.ch/record/2232040.

[101] The ATLAS Collaboration, Measurement of the ZZ production cross section in pp collisions at 8 TeV using $ZZ \rightarrow 2l2v$ and $ZZ \rightarrow 4l$ decay channels with the ATLAS detector, ATL-COM-PHYS-2014-1570, http://cds.cern.ch/record/1976407.

[102] M. Grazzini et al., W^+W^- production at the LHC: fiducial cross sections and distributions in NNLO QCD, Journal of High Energy Physics 2016 (2016) 140

[103] M. Grazzini, S. Kallweit and D. Rathlev Status of diboson production in NNLO QCD, arXiv:1601.06036 [hep-ph]

[104] B. Biedermann et al., Electroweak Corrections to $pp \to \mu^+\mu^- e^+ e^- + X$ at the LHC: A Higgs Boson Background Study, Phys. Rev. Lett. 116 (16 2016) 161803.

[105] LHC, Higgs cross section working group, SM Higgs production cross sections at $\sqrt{s} = 13$ TeV, https://twiki.cern.ch/twiki/bin/view/LHCPhysics/CERNYellowReportPageAt13TeV#ZH_Process

[106] LHC, Higgs cross section working group, VH calculations of the LHC HXSWG for the yellow report number 4, https://twiki.cern.ch/twiki/bin/view/LHCPhysics/LHCHXSWGVHYR4#Differential_cross_sections_from

[107] ATLAS AnalysisSoftwareGroup, ExtendedPileupReweighting, https://twiki.cern.ch/twiki/bin/view/AtlasProtected/ExtendedPileupReweighting

[108] The ATLAS Collaboration, Energy calibration prerecommendation for Run 2, https://cds.cern.ch/record/2060328.

[109] The ATLAS Collaboration, Jet Calibration and Systematic Uncertainties for Jets Reconstructed in the ATLAS Detector at $\sqrt{s}$=13 TeV, ATL-PHYS-PUB-2015-015, 2015, https://cds.cern.ch/record/2037613.

[110] G. Watts, F. Filthaut, G, Piacquadio, Extrapolating Errors for b-tagging, ATL-PHYS-PUB-2015-711, 2015, https://cds.cern.ch/record/2034234.

[111] G. Cowan et al., Asymptotic formulae for likelihood-based tests of new physics, Eur. Phys. J. C71 (2011) 1554, [Erratum: Eur. Phys. J.C73,2501(2013)], arXiv:1007.1727 [physics.data-an].

[112] The XENON10 Collaboration, Search for Light Dark Matter in XENON10 Data, Phys.Rev.Lett. 107 (2011) 051301.

[113] The COUPP Collaboration, First dark matter search results from a 4-kg $\mathbf{CF_3I}$ bubble chamber operated in a deep underground site, Phys.Rev. D86 (2012) 052001.

[114] The CDMS Collaboration, Silicon detector results from the first five-tower run of CDMS II, Phys. Rev. D 88, 059901 (2013)

[115] P. Cushman, C. Galbiati, D. McKinsey, H. Robertson, T. Tait, et al., Working Group Report: WIMP Dark Matter Direct Detection, arXiv:1310.8327 [hep-ex]

[116] Djouadi, A., Falkowski, A., Mambrini, Y. et al., Direct detection of Higgs-portal dark matter at the LHC, Eur. Phys. J. C (2013) 73: 2455.